UNIVERSITÀ DEGLI STUDI DI MILANO

Dipartimento di Fisica

Corso di Dottorato in Fisica, Astrofisica e Fisica Applicata

Ciclo XXXII

Strain-mediated magneto electric coupling and beyond: case studies by *in-operando* spectroscopy

Settore Scientifico Disciplinare FIS/03

Supervisore: Professor Giorgio ROSSI

Coordinatore: Professor Matteo PARIS

Tesi di Dottorato di:

Federico Motti

Anno Accademico 2019-2020

Commission of the final examination:

External Referees:
Prof. C. Back & Prof. P. Vavassori

External Members:
Prof. G. Ghiringhelli & Prof. R. Bertacco

Internal Member:
Prof. G. Rossi

Final examination:

19 December 2019

Università degli Studi di Milano, Dipartimento di Fisica, Milano, Italy

to the joy of seeking,
and finding the unexpected.

MIUR subjects:

FIS/03

PACS:

75.50.-y, 75.85+t, 75.70.Cn, 78.20.Ls, 77.84.-s

Contents

Acknowledgements

Talking to my peers, I often find consensus that going through a PhD is a tough and stressful (although formative) experience. Sometimes this unease can even become a real frustration, pushing the student to abandon the option of science as a career. I am happy to state that my PhD was none of that, and instead it was a joyful and rewarding part of my life. Nevertheless I maturated the belief that science itself accounted for only half of the story, the other half have to do with human relationships. Therefore I must sincerely thank all the people belonging to the APE beamline research team for building a collaborative, respectful and friendly atmosphere: I am grateful for having been part of it.

First of all I want to thank my supervisor, Prof. Giorgio Rossi. He always demonstrated a blind faith in me, giving me plenty of freedom to make my own mistakes and widen my experience in the direction I wanted. I think this was useful to develop a sense of responsibility. Despite being constantly trapped in a vortex of meetings and conferences all over the world, he never denied his help when he was asked for. During our rare meetings he always had a wise advice for me, which pushed me to think and view the problems from different perspectives. I am sure that the positive atmosphere pervading the APE group ultimately is a legacy of his kind and fair attitude. I can say the same of Dr. Giancarlo Panaccione, which I must also thank for first initiating me to the fine diplomatic art of writing, submitting and publishing a research article.

I am especially grateful to Dr. Piero Torelli, who *de facto* supervised my work on a daily basis. I found inspiring his way to handle the responsibility of a small research team: always injecting enthusiasm and optimism in the quest, taking charge himself of the most annoying tasks that a leader have to face. He was a strong guide, prompting me to pursue my scientific project with rigor and precision, although I never had the feeling he has given me orders. I was incited to develop my own ideas and to find the inventive to address the challenges I had to face, but I also found a precious source of practical and technical advices whenever I needed any. Finally, I am grateful for the numerous suggestions he gave me about being a scientist in its more general and human aspects.

A special thank should be addressed to Dr. Giovanni Vinai. He followed my first steps in the laboratory and trained me on the functioning of every machine, showing an unlimited patience and dedication. Even when I reached my independence, I could always rely on him for useful discussions and suggestions. He is also the local contact that every synchrotron user would like to have. Beside all of that, he was a friend more than a colleague in these three years I spent in Trieste.

I must acknowledge also Dr. "Sasha" Petrov, who grew the LSMO samples discussed in this thesis and performed many of the diffraction measurements. He has the habit of testing my understanding of physical phenomena raising very appropriate questions. Finally, he happily accepted to put his long experience as a MBE grower at work to indulge some of my bizarre and unfruitful ideas about oxide heterostructures.

I want to thank all the other scientists at whose side I spend these years in the lab, which resulted in various degrees of collaboration, scientific chatting and friendship. These include especially, for what regards the APE-HE beamline: Luca Braglia, Valentina Bonanni, Raju Edla, and Vincent Polewczyk. Among the others members of the NFFA-Trieste family I would like to remember Gian Marco Pierantozzi, Riccardo Cucini, Alessandro DeVita (SPRINT lab), Pasquale Orgiani, Sandeep Kumar Chaluvadi (PLD growth), Debashis Mondal, Ivana Vobornik, Jun Fujii (APE-LE), Andrea Fondacaro, Federico Salvador (technical staff). And of course Chiara Bigi, who shared a path parallel to mine at the LE branch of the

APE beamline. Mutual confrontation was extremely useful as we fought our way through the perils of a PhD. I also thank Tommaso Pincelli who, having concluded the same path two years before me, represented a useful reference in this journey.

There are many other people that gave a significant scientific contribution to the results presented in this thesis. They are (or soon will be) credited in the publications that involved their work. However I would like to especially mention here: Alessio Filippetti (IOM-CNR, Unit of Cagliari) for the DFT simulations, Christian Rinaldi and Matteo Cantoni (Politecnico di Milano) for setting up the MOKE microscope, Francesco Maccherozzi and Thomas Forrest (Diamond Light Source, I06 beamline) for their assistance during the PEEM measurements.

Finally, beside the scientific merit, I want to thank the UniMi PhD School secretariat Andrea Zanzani and the administrative staff at IOM-CNR for their support during these years.

Regarding founding, this research was widely supported thanks to the project "Progetto Internazionale NFFA" financed by MIUR, the Italian Ministry for University and Research.

1. Background

The work presented in this thesis addressed the *Electrical control of Magnetism*, a field of active research at this time [1]. In this introductory chapter we will see the general motivations connected with the technology of magnetic devices, and their bottlenecks that make the electrical control of magnetism an interesting challenge. The focus will be on *multiferroic heterostructures*, which are systems suitable for electrical control of magnetism: the principal mechanisms governing the magnetoelectric coupling in heterostructures will be addressed. This approach is independent, but complementary to that based on spin current-induced torques on magnetization. The field of electrical control of magnetism and multiferroic heterostructures has been expanding continuously in the recent years, and many recent review articles summarize the state of play. These reviews will be our background, and we avoid systematic citation of *all* the relevant literature published in the field, in already cited therein. We concentrate on the most general concepts. Specific papers, which are directly relevant for our work, will be discussed in the two following chapters, in order to clarify the role of the original results found within the state-of-the-art.

1.1. Spintronics

If the word electronics is used to indicate device functionalities arising from the physics and engineering of transport of electrons, the word spintronics indicates functionalities arising from the effect of the electron spin, along with its charge. Despite the word being still used only by a specific community, the advances in spintronics in the last 20 years have been in the hands of a wide public. In particular, it allowed the dramatic increase of storage density of hard disk drives by more than two orders of magnitude between 1990 and 2000. The birth of spintronics is commonly dated in the late 80s, with the experiments on spin-dependent transport carried on in parallel by Albert Fert and Peter Grünberg, for which they were awarded the Nobel Prize in Physics in 2007 [2]. The important breakthrough was the discovery of the so-called *Giant Magneto Resistance* effect (GMR), which describes the dramatic change of the resistivity in multilayer structured films depending on the relative orientation of the magnetization in the magnetic layers. In the first experiments, ferromagnetic films were separated by non-magnetic metallic layers, and the results were interpreted in terms of spin-dependent scattering of the conduction electrons. Later it was realized that an even bigger effect could be achieved substituting the metallic spacer layer with an insulating barrier, exploiting spin-dependent tunneling in a so-called *Magnetic Tunnel Junction* (MTJ). The potential applications were soon understood and exploited: if a bit of information is encoded in the magnetization of the layers (parallel or antiparallel), GMR gives an efficient tool to read this information electrically. This is nowadays implemented in the read heads of hard disk drives. As the platters rotate under the read head, that contains an MTJ, the stray fields of the bit domains affect the magnetization of the "free" layer on the junction, and the bit status is read from the resistance of the junction. It took less than 10 years from the first experiments of Fert and Grünberg to the appearance on the market of products containing GMR-based sensors, which is an extraordinary short amount of time between a fundamental scientific discovery and its commercial application at consumers level. Also, the impact on the market was striking, and allowed magnetic recording technology to keep the pace of Moore's Law like semiconductor-based memories and processors (known as CMOS technology, based on Metal-Oxide-Semiconductor junctions and field effect transistors realized from them). A summary of the advances in spintronics, both from the scientific and technological point of view, is given in figure 1.1.

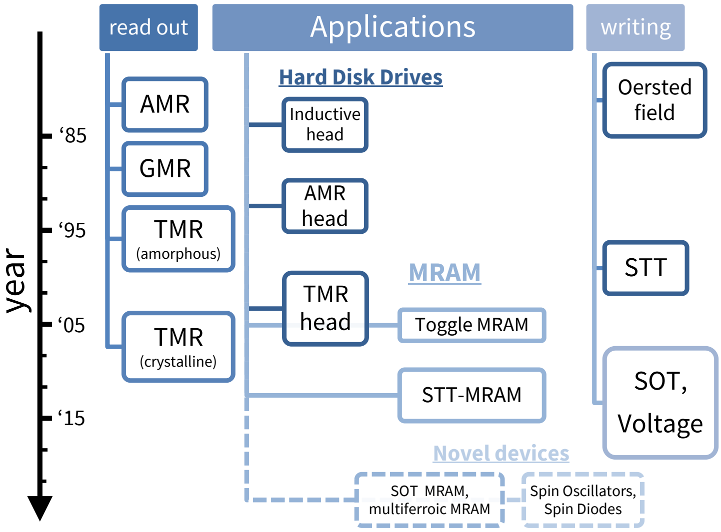

Figure 1.1: Advances in the world of spintronic with time, including both scientific discoveries (magnetoresistance effects for read out on the left, and spin manipulation for the writing process on the right) and technological applications (center). Adapted from [3].

Another device based on MTJ is the *Magnetoresistive Random Access Memory* (MRAM), a potential candidate for becoming a "universal memory" [4]. It is composed of an array of MTJs connected in a grid, and each of them represents a bit of information. They have the advantage over traditional static- and dynamic-RAM of being non-volatile, and hence reducing power consumption. It has a very high endurance, and in principle allows for the same read and write speed of traditional, volatile RAM. At present, our computers and communication devices contain different kinds of memory devices, each of them dedicated and optimized for a specific task. Static RAM is used in the first cache levels, requiring highest speed. Dynamic RAM, slower but denser, is implemented in the primary storage of CPU memory. And finally there are non volatile memories, such as flash or HDD, outside the CPU, dedicated to secondary storage. This requires a complex architecture to connect the different units, and a continuous data transfer between them. The usage of a single "universal" memory device, combining the advantages of many of the technologies used today, would improve system performance and reliability, reduce complexity and cost (probably even if at the expense of reducing density). This is the reason why MRAMs triggered such a wide interest. First commercialized in 2006, MRAM technology is finally on the market in 2016 as a 256 MB product. A schematic of a MRAM memory is illustrated in figure 1.2.

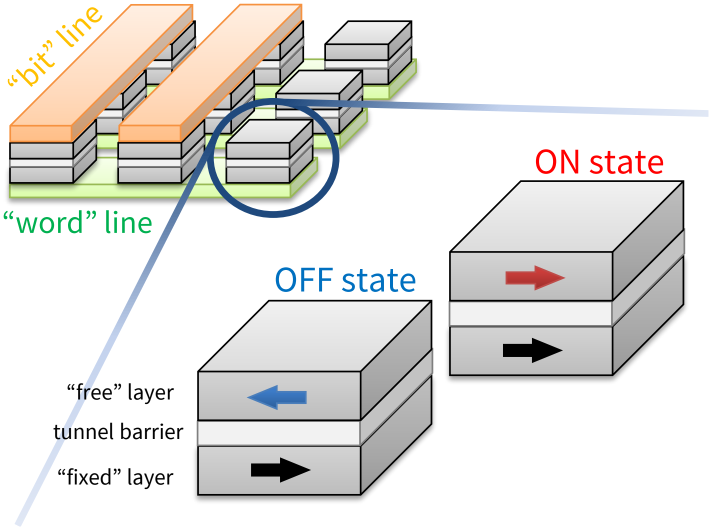

Figure 1.2: Schematic of a MRAM memory, and of a Magnetic Tunnel Junction.

One of the main issues regarding MRAMs (and magnetic memories in general) concerns the writing method: controlling magnetic fields at the micro- and nano-scale is not trivial, especially if we would like to do it in an embedded device. In the first MRAM prototypes, the magnetization in a MTJ could be switched with a magnetic field generated by currents passing simultaneously in the word and bit line, according to Biot-Savart law. Unfortunately this method is not scalable: reducing the size of the MTJ would require higher current, increasing power consumption. The development of the MRAM products currently available is based on a different scheme, named *Spin Transfer Torque* (STT). The flow of electrons through a magnetic material produces, as effect of spin-dependent scattering, a torque on the magnetization of the latter. This phenomenon can be used to switch the state of a MTJ making a current pass through the junction, the direction of the switch being determined by the polarity of the current. Contrary to field-induced switching, STT is scalable: when the dimension of the junction is reduced, the current required diminishes accordingly. Although this was a major breakthrough in MRAM technology, is it clear that using current is still not an ideal solution. Currents dissipate power by Joule heating, setting limits for power consumption and complicating the design of smaller and denser devices. Furthermore the requirements of faster writing operation, lower power consumption, higher thermal stability and reliability, are contradictory: while the first asks for higher current, the others for smaller [3].

An alternative to STT is under investigation: the *Spin-Orbit Torque* mechanism (SOT) [5]. This phenomenon relies on the spin-orbit interaction to transfer angular momentum from the orbital to the spin system, eventually resulting in a torque on the magnetization. The main consequence for MRAM technology is that a magnetization reversal can be obtained making a current pass “below” the junction, instead than “across” it, as for STT. Decoupling the read and write paths in the device ease the severe compromise between fast/efficient writing and reliable reading, and some promising results have been published already [6].

Beside the applications in memory devices that have been discussed here, there are many others in which spintronics may play a role in the future [7]. MTJ-based devices may be used in combination with CMOS for non-volatile logic operations, bridging the gap between data storage and computing. Micro-wave magnetic devices can be used for communication, but call for an efficient tuning of their ferromagnetic resonance. Finally, there are several ideas for bio-inspired computing and spin-caloritronics. All these applications would benefit from an efficient, fast, low-power control of magnetization.

1.2. Electrical control of magnetism

The use of current-induced torques to reverse the magnetization, instead of current-induced magnetic fields, was a giant step forwards for spintronic devices. However, the power consumption of STT-MRAM is still much higher compared to semiconductor technology like flash memories or field effect transistors, whose mechanism relies on charging/discharging a capacitor. Although SOT will help in this direction, still the use of currents is not ideal. Manipulating magnetism using electric fields, without current flow and hence avoiding Joule heating, would be ultimately preferable (to achieve some electrical control of the SOT mechanism is appealing as well [8]). Very recently, researchers from Intel published a study in which they propose a new spintronic logic device based on electrical writing of the magnetic state and its electrical reading through spin-orbit transduction [9]. They claim that such a device has the potential to overpass the performances of the state-of-the-art CMOS transistors. In order to achieve electrical control of magnetism, we can be inspired by the physics of semiconductors. In devices like field-effect transistors, an electric field generated through a metal-oxide-semiconductor junction depletes or accumulates charge carriers in the latter, tuning its conductivity. Is it possible to do the same with ferromagnets, acting on spin-polarized carriers? Unfortunately the charge density in ferromagnetic metals is so high that the electric field is screened within a very short length, and modifications of the bulk magnetic properties are impossible. However, electrical modulation of Curie temperature, magnetic anisotropy and saturation magnetization have been observed in diluted magnetic semiconductors such as Manganese-doped Gallium Arsenide (Ga,Mn)As [10]. The possibilities in this context are nonetheless limited by the lack of semiconductors displaying carrier-mediated ferromagnetism close to room temperature. Other field-effects like phenomena in metals and oxides will be discussed below.

The current-based approach aims at dynamically manipulating the magnetization by setting the system out of equilibrium. We may envision a conceptually different case, in which we could switch between two different magnetic ground states, according to the polarity of an applied electric field. A system of this kind can be realized in a multiferroic compound [11]. A *ferroic* material (ferroelectricity, ferromagnetism, ferroelasticity) exhibits some spontaneous non-zero value of an *order parameter* (electric polarization, magnetization, strain) which can be switched by an external *conjugate field* (electric, magnetic, or stress, respectively) as summarized in figure 1.3. Common features are the partition of the system into *domains* (regions within which the order parameter is uniform), high susceptibilities with respect to the external field, and eventually coupling mechanisms (piezoelectricity, magnetoelasticity, magnetoelectricity). A *multiferroic* is defined as a material exhibiting more than one ferroic order parameter. For the applications that we mentioned earlier, we are interested in multiferroics which are both ferroelectric and ferromagnetic, with a strong magneto-electric coupling.

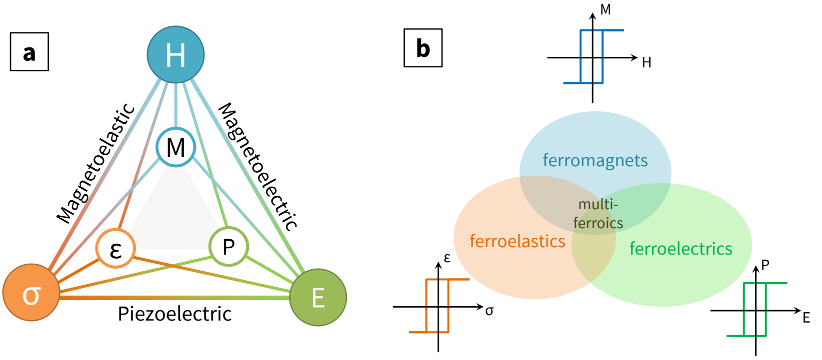

Figure 1.3: **a** - couplings between elastic, magnetic and electric properties in multiferroics. In empty circles are shown the order parameters, in the filled ones the external conjugate fields. **b** - different ferroic compounds and their intersection.

1.2.1. Single-phase multiferroics

Single-phase multiferroic compounds are actually very rare, because the driving mechanisms for ferroelectric distortion and magnetic ordering tend to be conflicting [12]. Ferroelectric materials are characterized by the lack of inversion symmetry: in oxides, the position of a cation is shifted with respect to the center of the oxygen polyhedron that surrounds it. Typically, the cation is formally in a d^0 configuration, and its displacement is favored by hybridization with oxygen $2p$ orbitals. On the contrary, magnetic materials are characterized by partially filled d orbitals, which become spin-polarized due to the exchange interactions. Furthermore, d occupancy often promotes a Jahn-Teller distortion which competes with the ferroelectric one. There are however other mechanisms that can promote ferroelectricity being compatible with magnetic ordering [13]. These include the presence of unbound valence electrons on the A site of the perovskite (*lone-pair* mechanism), geometric distortions due to steric effects, charge ordering, and magnetism itself. Multiferroics are usually classified in two categories. In *type I multiferroics* magnetic and ferroelectric ordering appear "independently", having origin from different mechanism. Famous examples are $BiFeO_3$ and $YMnO_3$. For these compounds both ordering may be robust, but the coupling between them is expected to be weak. In *type II multiferroics* instead, a particular arrangement of spins breaks inversion symmetry and promotes ferroelectricity. The two orderings are hence strongly coupled, but the disadvantage is that usually the induced polarization is rather weak and the magnetic order is antiferromagnetic (eventually canted). A notable example is $TbMnO_3$. These considerations clarify why single-phase multiferroics, beside being rare, are often also unsuitable for applications: robust ordering and strong magnetoelectric coupling are in competition, so that they emerge only in very peculiar conditions (e.g. only at low temperatures). This lack of suitable multiferroic compounds has pushed scientist to realize artificial multiferroic systems, combining different materials heterostructures [14].

It is worth mentioning that in the last few years we observed the rising of the new field of *antiferromagnetic spintronics* [15], for which electrical control of the magnetic order is equally interesting. Up to now the most promising approach exploited SOT and related effects [16]. In this perspective, single-phase and artificial antiferromagnetic/ferroelectric multiferroics deserve a special consideration. However, in the context of this thesis, we decided not to discuss this emerging trend and to focus on the electrical manipulation ferromagnetic systems.

1.2.2. Multiferroic heterostructures

Even if multiferroics are scarce, ferromagnetic or ferroelectric compounds are not. An appealing possibility is then to integrate different ferroic compounds in an artificial composite structure, taking advantage of interface physics leading to coupling between electric polarization and magnetization such to achieve the desired functionality. Material science greatly evolved in the last decades, passing through the challenges posed by the semiconductor physics and the development of spintronics. The more recent advances in the synthesis of thin films (mainly oxides) have also shown that the physical properties of compounds can be engineered by the growth protocol, and even new phases can be found at the interfaces, not expected in any of the single constituents [17]. Given the wide pool of candidates to choose from, the approach based on heterostructures can provide an exceptional flexibility for designing and realizing artificial multiferroics.

Most of the known ferroelectric materials are oxides with the perovskite structures. These materials can be grown in a highly controlled way by mature techniques like Pulsed Laser Deposition (PLD), Molecular Beam Epitaxy (MBE), sputtering, etc. Crystalline substrates are also commercially available. Most of the studies focused on ferroelectric $BaTiO_3$ (BTO), and piezoelectric/ferroelectric ceramics like PZT and PMN-PT. The choice for ferromagnets has been wider: from pure transition metals (Fe, Co, Ni), to alloys already relevant in spintronics (CoFeB), to complex perovskite oxides. In particular this last class of magnetic materials is very interesting: the rich physics of transition metal oxides is governed by electronic correlations, and can be tuned by several external stimuli. The research in this field has flourished in recent years, opening possibilities for discovering and engineering novel magnetic phases in all-oxide multiferroic heterostructures.

1.3. Magnetoelectric coupling in multiferroic heterostructures

Talking about heterostructures, the understanding of the coupling mechanisms between magnetism and ferroelectricity at the interface is crucial. In literature, four different mechanisms were proposed, that are conceptually distinct since they have origin from different interactions [18]. These are charge-mediated (originating from the electrostatic interactions), strain-mediated (involving transmission of stress across the interface), exchange-mediated (involving modifications of the exchange interaction), and chemistry-mediated (involving ion migration across the interface) effects, as summarized in figure 1.4. These phenomena have different characteristic length-scales, but in many cases they may be present simultaneously. Hence, a key challenge is disentangling the different origins of the observed magneto-electric coupling in a system. Only this understanding will enable the design of multiferroic heterostructures with desired characteristics for applications. In general, the magnetoelectric coupling can reveal itself as a change of different magnetic properties, as shown in figure 1.5. Scientists must be careful to fully characterize these effects, to avoid confusion in the interpretation of the results and in the speculations about their origin.

1.3.1. Charge mediated effects

Under the application of an electric field, the electrons in a material will experience a force and their density will be modified in order to screen the external field. Since charge carries are also responsible for the mag-

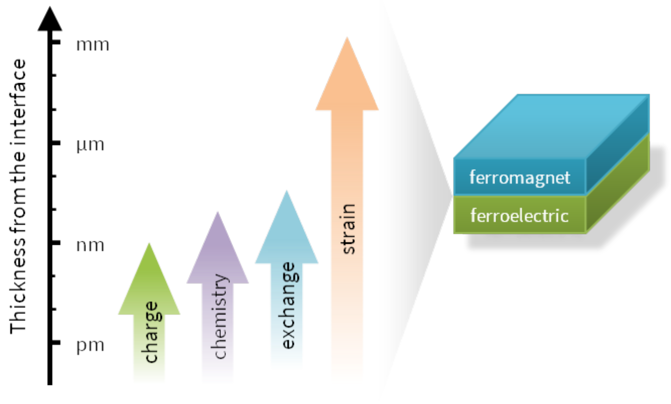

Figure 1.4: Typical length scale for the different coupling mechanism at the interface between multiferroic heterostructures.

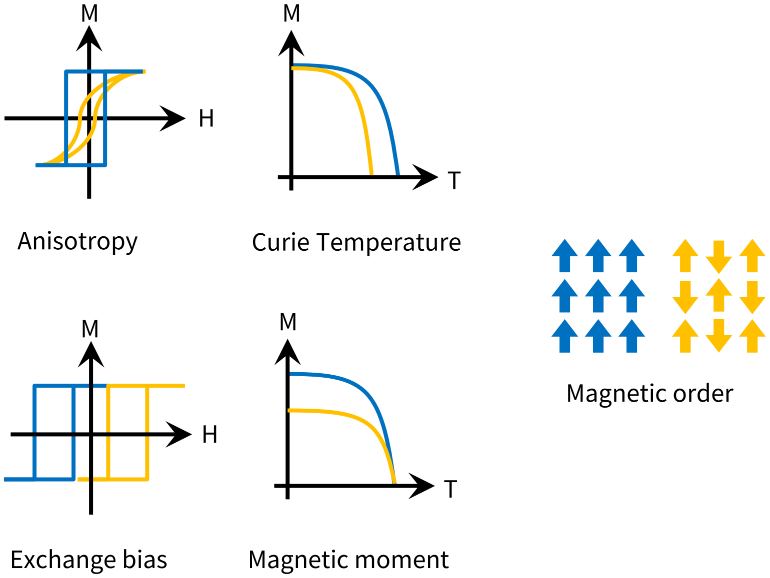

Figure 1.5: effect of a change in different magnetic properties.

netic properties in many materials, the field effect can be used in principle to manipulate magnetism. The magnitude of the electron density perturbation depends ultimately on how many free carriers can participate in the screening. In semiconductors the carrier density is determined by the doping level (between 10^{13} and $10^{20}\,\mathrm{cm}^{-3}$), and the redistribution of charge may extend for tens of nanometers. In metals, however, the density of free carriers is much higher (around $10^{22}\,\mathrm{cm}^{-3}$) and the characteristic screening length is of the order of a single unit cell [10]. Complex oxides are an intermediate case, since their conductive properties are also determined by chemical doping (e.g. in cuprates, manganites…) but with higher densities with respect to standard semiconductors. The typical screening length is of the order of 1 nm [19]. Hence, if we exclude the peculiar case of diluted magnetic semiconductors, electrostatic gating in magnetic materials can induce variation in electron density only in a very thin interfacial region. If we want to induce a sizable change in the magnetic properties, high fields and low thicknesses are required. Experimentally this is hard to achieve and calls for the highest structural quality of the materials to avoid charge leaking through defects. However, compared to the standard approach of gating through a dielectric, ferroelectrics are helpful for the purpose: they have a high dielectric constant, can provide high areal charge density at the interface, and of course can add non-volatility to the induced changes.

Charge accumulation or depletion at the interface can induce a local change in the spin and/or orbital populations at the Fermi level, responsible for a change in the Curie temperature, magnetic moment and/or magnetic anisotropy. These effects can be observed in metals, even if limited to very thin regions. Charge mediated effects are an excellent playground for correlated oxides: the delicate balance governing their electronic properties enables phenomena that have no analogue with metallic systems. For example, a change in charge density can result in electronic reconstructions and magnetic transitions, similar to the effect of chemical doping [20]. Often valence of transition metal ions, orbital polarization and spin populations are entangled, giving rise to interesting new physics. The limited length-scale of charge mediated effects makes them difficult to observe experimentally, but this is not actually a strong limitation for applications. Indeed, in spintronic devices based on tunneling, the interfacial properties have a key impact on the performances, and a change in the magnetic properties within 1 nm or less can generate a sizable on/off ratio. Voltage-induced change in anisotropy may also be combined with current-induced torques to improve the efficiency of the switching mechanism, as demonstrated in MTJs [10].

1.3.2. Strain mediated effects

Magnetostriction indicates the deformation of a material related to a change in its magnetization. The physical origin lies in the spin-orbit coupling: the spin orientation, mainly responsible for the magnetic moment of an atom, is linked to the orbital degree of freedom, responsible for the anisotropy of the electron clouds. Hence stretching the atomic bonds will affect the direction of the magnetic moment and vice versa. On the other hand in a ferroelectric material, the displacement of atoms that generates an electric dipole is also accompanied by a deformation of the unit cell. Ferroelectrics are part of a wider class of materials called piezoelectrics, which distort under an electric field, and vice-versa develop an electric dipole under mechanical stress, but do not possess spontaneous polarization. Since both magnetic and electric polarizations are linked to the lattice, strain can be used as an intermediate to link the two, obtaining a magneto-electric coupling in a heterostructure. An electric field deforms the ferro/piezo-electric material and the strain propagates across the interface into the magnetic material, affecting its magnetic properties. Contrary to the other mechanisms, strain-mediated effects are the only ones that can propagate on the macroscopic scale.

It is easy to understand that magneto-crystalline anisotropy and magnetostriction are linked, since they both originate from spin-orbit coupling: indeed a typical effect of an induced strain in a ferromagnet is a change in the anisotropy. As magneto-crystalline anisotropy is determined by different constants relative to different orientations, also magnetostrictive effects can have different magnitude (and even sign) according to the crystallographic direction along which the stress is applied. These considerations suggest that a precise control of the epitaxy relation in the heterostructure may be required to optimize the strain-mediated magnetoelectric coupling. The ferroelectric domain structure also plays an important role in strain-mediated effects [21]. It was shown that the shape of ferroelectric domains can be imprinted onto the ferromagnetic ones, and that the behavior under applied electric field (e.g. remanent vs. volatile effects) can be strongly dependent on the ferroelectric domain switching process. This fact complicates the interpretation of experimental results on the macroscopic scale, and calls for a careful study of the ferroelectric domains on the microscopic scale.

Electrical adjustment of magnetic anisotropy can be exploited to assist other switching mechanisms, reducing the required power. Moreover, the change in anisotropy can induce a huge shift in the ferromagnetic resonance of a device, which is highly desirable for radio frequency/microwave applications [22]. However, symmetry reasons prohibit strain-mediated effects to be the cause of a deterministic reversal of the magnetization direction: since the anisotropy energy is even under inversion symmetry, two states with opposite magnetization will always be degenerate. Hence, it is possible to achieve full-electrical 90° rotation of magnetization through strain-mediated coupling, but not a 180° rotation [14]. This is somehow a limitation for memory applications, in which the "ON/OFF" switch is achieved by a full reversal. Also in this case complex oxides deserve a special attention. Their magnetic ground state is often the result of a delicate balance of interactions (*direct exchange*, *super-exchange*, *double-exchange*), and the parameters governing them always involve the overlap between orbitals in some manner. Hence any modification in the crystal structure affecting it may trigger a magnetic phase transition. These include tensile/compressive strain but also the rotational pattern of the oxygen octahedral. The special case of manganites will be discussed extensively in the next chapter.

1.3.3. Exchange mediated effects

As mentioned before, the vast majority of the single phase multiferroics display an antiferromagnetic ordering, while a net magnetization is generally required for applications (both ferromagnets and antiferromagnets display an Anisotropic Magneto Resistance, according to the direction of the current respect to the magnetic moments, but this effect is quite small [3]). Nevertheless, antiferromagnets also play a role in the MRAM technology: one of the two ferromagnetic layers is usually "pinned" by the exchange bias generated at the interface with an antiferromagnetic layer, permitting a selective switch of the "free" layer during the write operation. We can thus imagine manipulating electrically the antiferromagnetic order in a single-phase multiferroic, modifying the exchange bias applied to the ferromagnetic layer [23]. The exchange coupling has a typical length-scale of few nm [24], which is about an order of magnitude bigger than for charge-mediated effects, so it can cause sizable changes also in thin metallic films. Since the exchange bias induces a preferential direction in the magnetization, changing its sign can even produce a full reversal of the magnetization, as demonstrated for example in CoFe/$BiFeO_3$ heterostructures [25]. Up to now most of the studies were focused on $BiFeO_3$ (BFO), since it is one of the few multiferroics with a Neel temperature above 300 K [11]. Even in this case the structure of the multiferroic domains is crucial in determining the magnitude of the effect, and the study of the interplay between ferroelectric and magnetic order in BFO is in itself a challenging and exciting research topic. It is worth remembering that BFO and other multiferroics are strongly correlated materials, in which the rotation of the electric polarization affect all the others degrees of freedom. The multiferroic/ferromagnet interface can therefore host a plethora of phenomena, not only mediated by exchange interactions, but also by strain and charge.

1.3.4. Electrochemical effects

A final mechanism for the voltage control of magnetism regards electrochemical effects, i.e. an applied electric field triggers a reversible modification of the chemical composition of a ferromagnetic material. Strictly speaking, these effects do not involve multiferroic heterostructures, since up to now ferroelectrics where not employed for these kinds of experiments, but it is worth mentioning few examples for completeness. At oxide/ferromagnetic metal interfaces, in which the former is used as a gating dielectric, we can expect to observe charge-mediated effects described previously. However, some experiments also found non-volatile effects when the voltage is removed, which calls for a different explanation. It has been shown that, in systems such as Co/Gd_2O_3 and NiCo/HfO_2, the electric field can induce a reversible oxygen ion migration across the interface, also changing the magnetic properties like saturation magnetization and magnetic anisotropy. The migration of ions can propagate far beyond the interface, affecting the magnetic layer on a scale of about ten nanometers [18]. Thus this is not a simple interfacial re-hybridization of the bonding between metal and oxygen, but can be considered properly a chemical reaction driven by voltage. Something similar can also happen in ferromagnetic oxides, whose properties can be largely affected by the presence of oxygen vacancies. These defects can be created and annihilated by large electric fields following an electrochemical mechanism similar to the one discussed for metals. Again manganites attracted most of the efforts in this context, besides ruthenates and other non-magnetic oxides like vanadates. To generate large electric fields, often ionic liquid gating was employed, and in such experiments charge mediated and electrochemical effects can coexist. The relative importance of the two depends on oxygen diffusivity, and to monitor the chemical state of the materials under study, spectroscopic techniques are invaluable.

2. Experimental techniques

Most of the original results discussed in this thesis have been obtained by the experimental techniques described in this chapter. As these are mature methodologies we make reference to selected textbooks ad review articles, as representative of a rich literature. In the first section the growth of thin film and heterostructures by physical deposition will be introduced. Emphasis will be given to Molecular Beam Epitaxy, which was the chosen synthesis approach for growing the samples that were needed for the scope of this thesis. Next we will introduce the fundamentals of X-ray Absorption Spectroscopy (XAS) and its specialization of polarization dependent X-ray Magnetic Circular Dichorism (XMCD) and of photoelectron energy resolved Photoemission Electron Microscopy (PEEM). These are techniques based on the availability of tuneable synchrotron-light which implies understanding the physics of photon absorption as well as the technical aspects of photoelectron signal retrieval. The interpretation of our experimental results however is quite robust and does not depend on models, so the theoretical background is kept as concise as possible. The Magneto Optical Kerr Effect (MOKE) is described in a dedicated chapter as magneto-optical measurements were extensively used during the PhD project for preliminary magnetic characterization of samples. Finally we describe the apparatuses used to carry out the experiments discussed in the following chapters.

2.1. Layer controlled growth of thin films and heterostructures

A very active field in solid state physics is that of surface, interface and generally matter of low dimensionality. The synthesis of high quality material samples with a high-degree of control of stoichiometry, crystallinity and morphology is a prerequisite for advanced experiments. These requirements have pushed the development of the modern techniques for physical deposition of thin films and heterostructures, among which we concentrate on *in-situ* techniques: Pulsed Laser Deposition (PLD) and Molecular Beam Epitaxy (MBE). These techniques can produce samples with an extremely high crystal quality, in many cases comparable (if not superior) to what can be obtained with the synthesis of bulk crystals [26]. The unique advantage of deposition of thin films is the possibility to engineer some physical properties and grow artificial materials that have no bulk counterpart. Indeed the control of many growth parameters are driving the research in condensed matter towards discovery of new phenomena and engineering of new functionalities. The principle of physical vapour deposition techniques is simply to direct an atomically pure beam towards a suitable, atomically clean, single crystal substrate. Thermodynamic conditions can be set close to equilibrium between adsorption and desorption, allowing for an energetically controlled growth process, or far from equilibrium as in the case of highly energetic ablated atomic clouds whose fine kinetic energy distribution determine the growth mode. The target sample temperature control is one of the parameters that determine the mobility of the adsorbed atoms in the growth process. In the case of MBE the molecular beam comes from thermal evaporation of element-pure nuggets placed in a dedicated crucible. Atoms from the crucible sublimate and the wanted vapour pressure is reached at a certain temperature. The sample substrate is exposed to a quasi-ballistic molecular beam with low kinetic energy coming from the crucible. The rate of evaporation, and hence of deposition, is typically of the order of few Å min^{-1}. Complex materials are obtained by alternate or simultaneous exposure of the substrate to more elemental sources, in a controlled partial pressure (e.g oxygen or ozone for growing metal oxides). In PLD instead, a powerful laser pulse is shot against a target of the desired material (usually in form of a stoichiometric powder). Atoms from the target are ablated by the IR laser pulse, form a plasma plume which ultimately reaches the surface of the substrate. In all cases, the molecules must have an adequate mean-free-path to reach the substrate, so that the background pressure during deposition must be low, from UHV ($10 \cdot 10^{-12}$ mbar for MBE of ultra-pure GaAs, to partial pressures of pure oxygen in the mbar range for oxide-PLD). The growth of oxide thin films requires an oxidizing atmosphere (it may be molecular oxygen, atomic oxygen or ozone) with partial pressure spanning over decades. For example, in PLD the atomic species coming from the plasma plume have quite a high kinetic energy, while in MBE the molecular beam is thermal and has low energy. This allows PLD to be carried out at higher background pressure (up to 1 mbar) compared to MBE (3-4 orders of magnitude lower), which may be useful in case of species reactive to oxidation. The absence of highly energetic atomic species is nonetheless considered the cause of the superior crystal quality achievable by MBE [27]. Another difference is that PLD can achieve a relatively high deposition rate compared to MBE. This is an advantage for growing thick films or superlattices, but MBE allows for a better control over thickness. A common tool for real-time (*in-operando*) characterization is Reflection High Energy Electron Diffraction (RHEED) [28]. High energy electrons coming from a gun impinge on the sample at grazing incidence and are scattered. An atomically clean surface will produce an electron diffraction pattern, which can be used to infer the symmetry and the structure of the sample, or eventually a surface reconstruction. The high kinetic energy and the scattering geometry allow RHEED to be used during a deposition process, and hence to monitor the growth as it is happening. When a new atomic layer is growing, it usually forms 2D islands on the surface. Hence new atomic steps are appearing, which ruin the perfect periodicity. The intensity of the RHEED spots is reduced, because of the destructive interference between electrons scattered by the two atomic planes. When the 2D islands grow and merge, the number of atomic steps is reduced, with consequent increase of the RHEED spots intensity. During the deposition one can observe oscillations in intensity with a period that corresponds to the formation of one atomic plane. This allows monitoring the layer-by-layer growth of the film, with in principle a control over thickness of a single unit cell, and it is a powerful tool for achieving the desired stoichiometry in complex compounds [29].

Regarding the strategies for material engineering, one important tool is the choice of the substrate [26]. The clean and ordered surface of a crystal can act as a template for the growth of a thin film of a material with the same, or similar, crystal structure (what is called *epitaxy*). This is true, within certain limits, also in presence of a mismatch between the lattice parameters of the film and the substrate. As a consequence, a certain amount of strain can be induced and tuned in the crystal structure of the film just by choosing the proper substrate. In some cases this strain can be much larger than what is achievable in bulk crystals, profoundly affecting the properties of the film. Another important aspect is that if the growth proceeds layer-by-layer, a fine control of the thickness can be achieved. This can be exploited to grow ultra-thin films with a high surface/volume ratio i.e. materials that often display exotic electronic and magnetic effects reflecting the two-dimensional nature of the system [30]. Artificial materials can also be synthesized in the form of thin films with no stable bulk counterpart [31]. Finally, the control on thickness and stoichiometry can be exploited to grow heterostructures and superlattices [32], in which the composition of the material changes on the nanometer scale: again something that cannot be achieved in bulk systems [17]. In the field of electrical control of magnetism, one exciting possibility is the design of entirely new single-phase multiferroic compounds with high ordering temperature [33].

2.2. X-ray absorption spectroscopy with synchrotron radiation

Low energy excitations of weakly bound electron states in solids are the most effective messenger of the collective properties of condensed matter. Extended “valence electron” states describe the chemical bonds and macroscopic properties as thermal and electrical conductivity, magnetism, optical response, and all exotic order parameters. Probing low energy electron states in solids is hence a key experimental task of spectroscopy. Relevant binding energies, as referred to the Fermi energy, range from few eVs to sub-eV, corresponding roughly to visible light in the electromagnetic spectrum. On the other hand core electrons are strongly bound to the ionic core, with energies corresponding to UV or X-ray radiation. Since core levels are basically non dispersive, their energy is characteristic of the atomic specie, and their measure can be used for chemical analysis via atomic photoionization cross sections and understanding of photoelectron scattering in matter. In *X-ray Absorption Spectroscopy* (XAS) a core level is photoionized and an electron is promoted to an available empty state. This is done by absorbing a photon in the X-ray range, whose energy is matching the energy difference between the two states involved. The results can be interpreted adopting different models, as will be later discussed in detail. It is important however to keep in mind that the core hole generated in the absorption process strongly perturbs the valence electrons, which in most of the cases will rearrange to screen the charge of the hole. This implies that the XAS spectra cannot be simply understood in an independent-particle picture, but carry information on the electronic correlations, which is actually the most interesting aspect. Finally, different effects observed as a function of the polarization of the incoming radiation (i.e. dichroic effects) allow us to probe magnetic properties or the anisotropy of the electron density. The basic underlying principle of dichoric effects is that absorption of polarized light probes empty states with a definite symmetry. From the practical point of view XAS measurements imply shining monochromatic X-ray radiation on the sample, which will be absorbed in correspondence of a resonance, i.e. a particular electronic transition. What it is needed is then a tuneable monochromatic X-ray source and a detection method for measuring absorption. Synchrotron radiation (SR) from 2-6 GeV electron energy storage rings and insertion-type radiators is the premium source of X-rays for spectroscopy. In third-generation machines insertion devices (*wigglers* and *undulators*) are placed along the ring, which produce a magnetic field that makes the electrons oscillate around their average trajectory. The generated radiation has high intensity, low divergence and a well defined fixed, or tuneable polarization. Its energy spectrum is composed of several broad harmonics, whose peak energy is determined by the magnetic field strength, periodicity and phase of the undulator (see figure 2.1). A monochromator is employed to select the desired wavelength that is finally delivered to the sample. Laboratory X-ray tubes deliver characteristic radiation lines overlapping a continuum *Bremsstrahlung* background, whose intensity is dramatically (more than a million times) lower that of SR and there is no control over polarization. This is the reason why SR is mandatory for XAS experiments and related techniques.

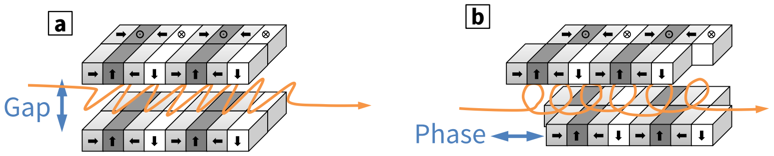

Figure 2.1: Schematic of an APPLE-II undulator. Adjusting its parameters (gap and phase) it is possible to tune the energy and the polarization of the photons. Small black arrows indicate the direction of the magnetic dipoles. Orange lines indicates the trajectory of the electrons. **a** - case of horizontal polarization **b** - case of circular polarization.

But how is an absorption spectrum measured? [34] The simplest solution conceptually consists in measuring the X-ray intensity before and after the sample. Practically, however, this method requires some special sample preparation. Especially in the soft X-ray range, the sample must be very thin (below 1 µm) to let any radiation pass through. The absorption of X-rays sets the electrons of the sample in an excited state which quickly decays through different channels, each of which can be used for detection. One mechanism is the decay through Auger processes, resulting in an avalanche of secondary electrons that are emitted into vacuum only when they are generated near the surface. Measuring the emission of these electrons, i.e. with a channeltron electron multiplier, is the basis of the so-called *total electron yield* (TEY). Measuring a drain current that compensates this flow of charge gives a very practical method for TEY detection, requiring only a picoammeter between the sample surface and ground. It is important to stress that only electrons very close to the surface can escape and contribute to the measured signal. This makes TEY detection surface sensitive, with a probing depth between 5 and 15 nm, depending on materials. Another channel for the core-hole decay is the re-emission of photons, which can be detected by a photodiode in the *fluorescence yield* mode (FY). Since photons are hardly scattered by the atoms in the sample compared to electrons (the absorption length can be several hundreds of nm), FY has a much bigger probing depth than TEY, and can be considered "bulk sensitive" for most applications in surface science. Despite that, fluorescence photons can be reabsorbed, refracted and reflected at interfaces and surfaces, which can result in the occurrence of saturation effects when the absorption length is indeed comparable to the escape depth. This can greatly distort the measured spectra compared to the true absorption cross section, a problem that is substantially reduced when detecting the TEY. A final remark is that the cross-sections for Auger and fluorescence decay may be very different according to the absorption edges. For K edges in the hard X-ray range usually they are comparable, but for L edges in the soft X-ray range (those interesting for magnetism in transition metals) Auger is the dominant process. The ratio of fluorescence decay also increases for heavier elements.

2.2.1. Theoretical description of XAS spectra

In quantum mechanics, the probability of transition $W_{i\to f}$ between an initial state $|i\rangle$ and a final one $|f\rangle$ by means of a perturbation is given by the well-known Fermi Golden Rule.

$$W_{i\to f} \propto \sum_q |\langle i|\vec{e}_q \cdot \vec{r}|f\rangle|^2 \delta(h\nu - E_f + E_i)$$

Here, the perturbation Hamiltonian, which describes the electromagnetic radiation, is described within the dipole approximation, with q a quantum number describing the polarization [35]. The initial state is the ground state of the electronic system and the final one contains the core-hole. A Dirac delta-function ensures the conservation of energy: the energy of the absorbed photon matches the difference between final and initial states. The interesting information about the absorption process, i.e. the line-shape of the spectrum, is contained in the matrix element. The Wigner-Eckart theorem, a powerful result of group theory, states that matrix elements like this can be calculated as a product of two components: one “radial” part, which determines the line strength, and an “angular” one, involving the symmetry of the two states and responsible for selection rules. Once we have chosen to use the dipole approximation, the main issue is how we want to describe the initial and final state wavefunctions. A first intuitive interpretation can be given with the independent particle picture, schematized in figure 2.2. The absorption process brings an electron from a core level (usually split in two lines by the spin-orbit interaction) to an empty state. Since we consider the particles independently, we suppose that the presence of a core-hole does not modify the empty energy levels, so does not the extra electron in the valence band. The absorption spectrum is then simply given by the (mathematical) convolution of the core level lines (in principle infinitely narrow) and the empty *density of states* (DOS), broadened by the instrumental resolution and the core-hole lifetime. To be more precise, we actually probe only the empty states which have a symmetry allowed by the selection rules, which may be different for the two components of the doublet.

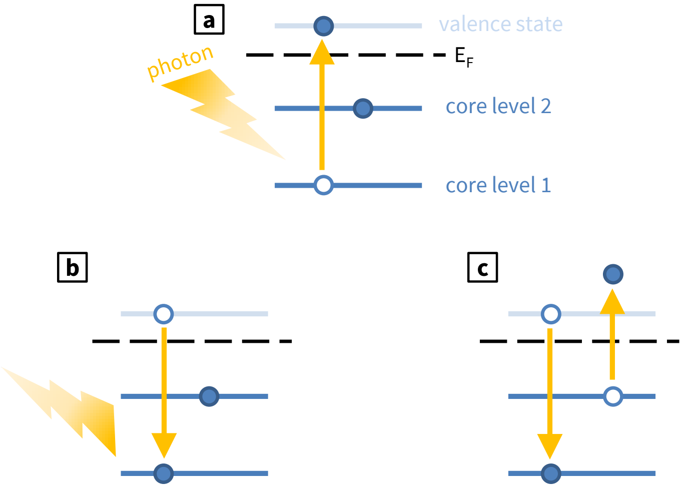

Figure 2.2: Independent-particle picture schematization of: **a** - the absorption process, **b** - the fluorescence decay, **c** - the Auger decay of the core hole.

The independent particle picture gives an insight of the physical meaning of the XAS spectrum, but not much more: indeed the core-hole wavefunction strongly overlaps with the valence states. This not only perturbs them (i.e. the DOS should be calculated with the extra potential generated by the hole), also the actual final state is given by a combination of the core-hole and valence state wavefunctions, a typical effect of electronic correlations. This is particularly true for the L edges of transition metals, like those presented in this thesis. Let's start with an atomistic picture. In the independent particle picture, the atomic orbitals are found solving the Schrödinger equation including the spherically-averaged part of the electronic repulsion. Adding the non-spherical part mixes the electronic wavefunctions, coupling the angular momenta of the different particles. The electronic states are then grouped in different terms $^{2S+1}L_J$, characterized by their values of the resulting spin (S), orbital (L) and total (J) angular momenta. The electronic interactions are described by the Slater-Condon parameters, which are basically direct and exchange integrals between single-particle atomic orbitals, and the energy levels of the system are given by combinations of these parameters. The idea for understanding an absorption spectrum is that we should calculate the energies of the possible terms for the initial and final configuration, and then the allowed transitions between the initial ground state and the final states. For what regards the final state, it is important to notice that the electrostatic interaction between the core hole and the valence electrons has to be taken into account, and so does the core hole spin-orbit coupling. In general the latter is not just a small perturbation and has to be treated on the same footing of the others (in a so-called intermediate coupling scheme), so that the eigenstates in the final state are not simply the terms $^{2S+1}L_J$.

Up to now we described an atomistic picture, but when dealing with atoms in a crystal or molecule, also its neighbor ions have to be taken into account. The main consequence is that the symmetry of the problem is lowered so that the energy levels cannot be labeled anymore by the same quantum numbers. The strength of the interaction between the neighbours is described by the crystal field parameters, the number of which increases for lower symmetry. In determining the electronic structure, their relative strength compared to the Slater-Condon parameters is crucial. In the atomistic limit, the effect of the crystal is just a small split of the atomic levels, while in the opposite case of a strong crystal field the eigenstates are labeled by the irreducible representations of the symmetry group and result from mixing of the different atomic terms. This behavior is summarized in the well-known Tanabe-Sugano diagrams. The presence of ligands around the absorbing atom has another consequence: *charge-transfer* effects. The hybridization between orbitals of the ligands and of the metal ion can induce a partial charge transfer between the two atoms, so that the ground state of the system should be described e.g. as a superposition of d^n and $d^{n+1}\bar{L}$ states, where $\bar{L}$ indicates a hole in the ligand. The same is also true for the final state, where the presence of a core hole can induce a rearrangement of the charge between the metal ion and the ligands. To describe these phenomena few other parameters need to be introduced: the hybridization strength V and charge-transfer energy Δ. Charge-transfer effects are important to reproduce the correct lineshape, especially the broadening of the peaks, and may induce the presence of weak satellites.

2.2.2. X-ray magnetic circular dichroism

The power of synchrotron-based spectroscopy in the study of magnetic materials lies in the possibility to probe the magnetic moment of atoms exploiting dichroic effects, i.e. changes in the absorption according to the polarization of the X-rays. Recalling the Fermi Golden rule, we see that the dipole operator also contains the polarization of the light. Averaging over the quantum number q will give the isotropic XAS spectrum, but other information can be obtained from the difference of two spectra for definite q. *X-ray Magnetic Circular Dichroism* (XMCD) is the difference observed reversing the helicity of the photon, from left- and right-circular polarization. Why this is related to magnetism can be simply understood in the independent-particle picture. Let's consider for example the case of the $2p-3d$ transition ($L_{2,3}$ edges of the transition metals). The $2p$ levels are split in two by the spin-orbit interaction ($2p_{3/2}$ and $2p_{1/2}$). X-rays with $q=\pm1$ will promote transitions in which $\Delta m_l=\pm1$. On the other hand, the spin moment will be preserved, $\Delta m_s=0$. The dichroic effect comes from the fact that the $3d$ electrons in magnetic materials have a well defined value of m_s (the valence band is spin-polarized), while the $2p$ electrons do not (they have a defined value of m_j instead). Let's consider the extreme case in which only spin-up d electrons are taken into account (100% spin polarization). Then if we calculate

$$W^{q}_{2p,j\rightarrow 3d,\uparrow} \propto \sum_{m_j,m_l} |\langle 2p,j,m_j|\vec{e}_q\cdot\vec{r}|3d,m_l,\uparrow\rangle|^2$$

We will see that, fixed q and the spin $\uparrow$ of the $3d$ states, the transition probability for the two different j values (corresponding to L_2 and L_3 edges) is different. Switching q will increase the intensity of one edge and decrease the intensity of the other, so that the difference would produce the typical XMCD spectral shape, with a positive and a negative peak [36]. This concept is schematized in figure 2.3. Of course this is a very simplified model, and a more accurate one should consider all the effects described for XAS [35].

A consideration about the geometry of the experiment must be added. The quantization axis is determined by the helicity of the photon, which is parallel or anti-parallel to the propagation direction for circularly polarized light. This means that with XMCD we actually probe the component of the magnetization parallel to it. If the magnetization direction is aligned

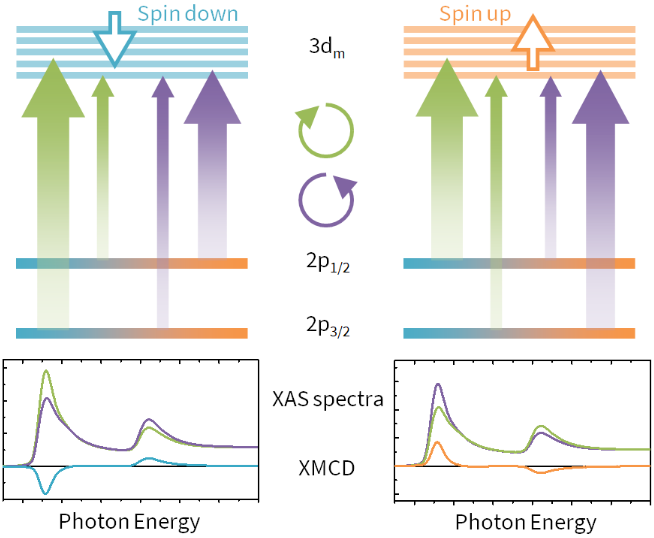

Figure 2.3: Schematic of the XMCD phenomenon in the independent-particle picture (above) and corresponding examples of XMCD spectra (below). The width of the arrows corresponds to the intensity of the transitions.Green and purple colours correspond to opposite helicity of the photon, blue and orange to opposite orientation of the spin.

parallel to the propagation of the X-rays, reversing the helicity produce identical spectra as inverting the sample magnetization direction. Some flexibility in the geometry of the experiment (direction of the applied field, orientation of the sample) can be exploited to get a deep insight into the magnetic anisotropy. Another important advantage of XMCD is that it is quantitative. Some specific *sum rules* were derived in quite general conditions for the $L_{2,3}$ edges of transition metals [37]:

1. The integral of the isotropic XAS spectrum is proportional to the number of holes in the valence states n_h. Note however that for obtaining the quantitative results the absolute absorption has to be measured.

2. The integral of the XMCD spectrum is related to the average of the orbital angular momentum L^z. To obtain a number in physical units, n_h has to be known.

3. If it is possible to clearly subdivide the XMCD spectrum in a L_2 and a L_3 parts, their integrals can be combined to obtain the average of the effective spin angular momentum S^z_eff. It is "effective" since it contains also a "magnetic dipole term", which is usually small but cannot be always neglected [38].

These rules are what make XMCD such a powerful tool to study magnetism in transition metals. Another unique feature of this technique is that it is element sensitive. In alloys it can be used to disentangle the magnetic behaviours of different atomic species [39], or selectively probe induced magnetism in non-magnetic materials at interfaces [40]. Changing the applied magnetic field, it is possible to measure element sensitive hysteresis loops, again to distinguish different anisotropies or coercivities in heterostructures. One final remark is that XMCD is usually unaffected by artefacts more commonly encountered with bulk-sensitive magnetometry techniques such as VSM or SQUID. Being element sensitive, one can be sure that the signal measured is coming from the sample. The shape of the XMCD spectrum for several compounds is well known and has a characteristic shape, clearly recognizable. The ability to reverse both the magnetic field and the polarization can finally be exploited to distinguish a "true" magnetic signal from an artefact affecting the shape of the spectrum.

2.2.3. Photoemission electron microscopy

As already mentioned, one consequence of X-ray absorption are avalanche decay processes, that result in the emission of secondary electrons from the surface. The quantification of these electrons is at the basis of the TEY detection. However, detecting the emission of these electrons with spatial resolution can be used as an imaging technique. This is at the basis of *Photoemission Electron Microscopy* (PEEM). The sample surface is illuminated with a photon beam, and electrons are emitted with a wide distribution of kinetic energies. Similarly to optical microscopy, the highest resolution can be obtained when the particles are emitted normal to the surface. For this reasons they are accelerated by a strong electric field (about 10 kV) towards an electron optic system which forms a two-dimensional image on a suitable detector. The lateral resolution is ultimately determined by the chromatic aberration, i.e. the fact that electrons with different kinetic energies will follow different paths in the optics system. For this reason a contrast aperture is employed, which cuts the high energy distribution of the electron spectrum. Some other specific elements may be used to correct these aberrations, or to narrow the kinetic energy distribution. Ultimately, the lateral resolution is also determined by imperfections on the sample surface, which inevitably produce some aberrations. With soft X-rays in a synchrotron beamline, typically a resolution of some tens of nm can be achieved. PEEM can be used to image nanostructures through several contrast mechanisms. One is the difference in work function between different materials, that is reflected in the yield, or different grains and crystallographic orientations, which is dominant for low excitation energies. A chemical contrast can of course be exploited by tuning the photon energy at (and far from) a characteristic absorption peak. But one of the invaluable advantages of PEEM is that it can be used to image magnetic domains exploiting XMCD. At an energy fixed on the absorption edge, two images obtained with reversed photon helicity will show an opposite contrast for the magnetic domains. The vectorial nature of the XMCD can be exploited to obtain a proper 2D vector map of the magnetization if the same region is imaged two times, rotating the sample by 90°.

2.3. Magneto optical Kerr effect

The *Magneto Optical Kerr Effect* (MOKE) indicates a change in the polarization of the light reflected by a magnetic material. If the incident light is linearly polarized, the reflected one will be elliptically polarized with its main axis rotated with respect to the incident polarization. The Kerr effect can be quantified by two parameters: ellipticity and Kerr rotation angle, which are in general small (below 1°). The measurement of these effects is performed by employing a polarizer in the reflected branch and a detector, in order to translate a change in polarization in a change in detected intensity. By means of a photoelastic modulator, the signal coming from rotation and ellipticity can also be separated [41]. In general it is not easy to recover the real rotation and ellipticity from the measured signal, because of the several experimental parameters involved, and even more difficult is to relate the measured rotation to the magnetization of the material. For these reasons it is hard to obtain really quantitative measurements with MOKE. However, tracking the measured intensity as a function of the applied field a hysteresis loop can be recorded: MOKE measurements are then perfectly suitable for measuring coercivity, remanence, Curie temperature, and anisotropy. With some analysis, fine details about the dynamics of magnetization rotation can be obtained [42], and even reconstruct a complete vectorial picture [43]. Several geometric configurations can be exploited in MOKE measurements. In a given scattering plane, the polarization can be either parallel or perpendicular to it (called p and s polarization). Then, three variations are obtained according to the direction of the magnetic field relative to the scattering plane and the surface of the sample. These are called polar (field perpendicular to the surface of the sample), longitudinal (field parallel to the surface and the incidence plane) and transverse (field parallel to the surface but perpendicular to the incidence plane) MOKE, and are illustrated in figure 2.4. Each configuration is predominantly sensitive to different components of the magnetization vector [44].

But what is the physical origin of the Kerr effect? A very simple argument is based on a fully classical picture. The light in the visible range excites the conduction electrons (for metals, valence electrons for insulators), and their response to this stimulus produces the reflected light. Normally, the electric field along one direction (linear polarization) will "shake" the electrons along that direction and the reflected light will still have the same polarization. In presence of a magnetic field instead the electron

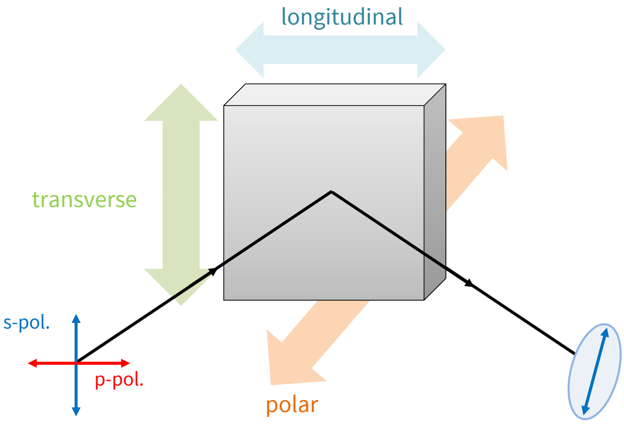

Figure 2.4: Various geometrical configurations for MOKE measurements. Light wide arrows indicate the direction of magnetic field, the red and blue small arrows the direction of polarization.

would follow curved orbits due to the Lorentz force, and the polarization of the reflected light will be rotated, and not fully linear. Mathematically this behavior is described by non-diagonal terms in the dielectric tensor ϵ. Symmetry considerations can be used to determine the form of ϵ for the various geometrical configurations, and it can be shown that the non-diagonal elements should be proportional to the magnetization (since the effect is small, we can always describe it as linear). Given the form of ϵ, the eigenmodes for light propagation inside the medium can be calculated, which for longitudinal and polar MOKE are left- and right-circular polarizations [45]. Starting from a linear polarization described as a sum of the eigenmodes, rotation originates from a de-phasing between them, while ellipticity comes from a difference in attenuation. The reflection is described imposing the continuity relation for the electromagnetic field at the surface. For a rigorous first-principle description of the phenomenon, the response function of the valence electrons to the external applied field must be computed. This is typically a computationally challenging many-body problem [46]: not only the ground state, but also the excited states need to be calculated, and the interaction between valence electrons cannot be ignored. For this reason the standard Density Functional Theory (DFT), which is reliable only for ground state properties, cannot describe magneto-optical effects satisfactorily.

MOKE measurements can be done with a simple visible laser in a table-top setup, which makes it a technique much more accessible than XMCD. MOKE is a very valuable technique for time-resolved studies because of the availability of laser sources with ultrashort pulses (below 1 ps [47, 48]). It can be also used to study nanostructures, either focalizing the light on a single microscopic objects [49], or exploiting diffraction from an ordered array of them [50]. The Kerr effect can be even exploited to image magnetic domains with an optical microscope [51]. Similar experiments with X-ray technique can be done only in large scale facilities. As a counterpart MOKE lacks the main advantages of XMCD: chemical selectivity (although there are some remarkable exception, see e.g. [52]).

2.4. Experimental setups

2.4.1. The NFFA-Trieste facility

NFFA-Trieste [53] is an open access facility to perform experiments involving growth, characterization and spectroscopy with synchrotron radiation. It is part of the Istituto Officina dei Materiali (IOM-CNR), located within the Elettra Synchrotron site. NFFA-Trieste is part of the wider consortium NFFA-Europe [54], whose aim is to provide access to infrastructures located at several different sites in Europe for users willing to carry out a multidisciplinary research project. Most of the experiments discussed in this thesis where performed within the NFFA-Trieste facility, exploiting the time dedicated to in-house research. The experimental set-ups described in the following are represented in figure 2.5.

APE-HE beamline

The *Advanced Photoelectric Effect* (APE) beamline at the Elettra Synchrotron uses photons emitted simultaneously by two insertion devices placed in the section number 9 of the storage ring, arranged in a zig-zag configuration, which produce two slightly divergent beams finally delivered in two distinct branches, able to work independently [55]. One branch is

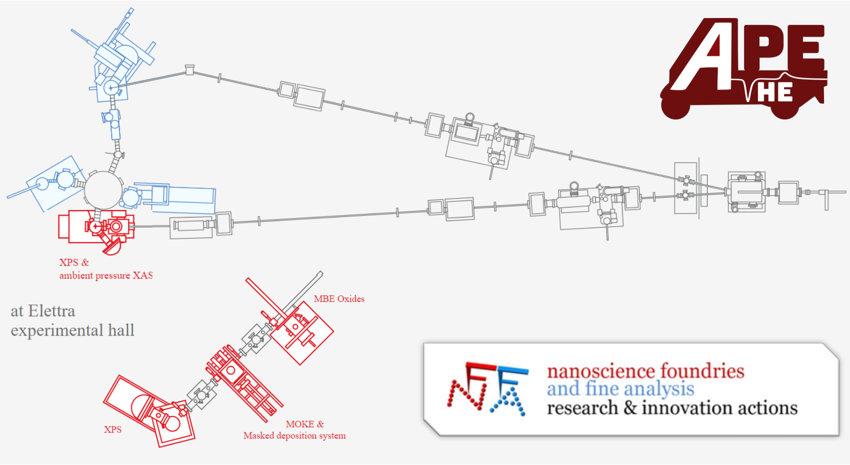

Figure 2.5: Diagram of the facilities at the Elettra experimental hall available within NFFA-Trieste. The set-ups described in the text are highlighted in red color.

labeled “Low Energy” (LE, photon energy between 10 and 100 eV) and is dedicated to Angular Resolved Photoemission Spectroscopy (ARPES) with spin-resolution. The second one is called “High Energy” (HE, photon energy between 150 and 1200 eV) and is dedicated to core-level spectroscopies: XPS, XAS and XMCD. The APE-HE branch will be described, were the measurements presented in this thesis were acquired. The undulator serving the APE-HE endstation is an APPLE-II type, composed by 36 periods of 2.16 cm each. It’s able to produce horizontal, vertical or circular polarization changing the vertical gap and the longitudinal phase. The light from the undulator is horizontally deflected by a spherical mirror onto the plane grating monochromator, which covers the 140 - 1500 eV energy range (900, 1800 lines/mm, double track with variable groove density). The spherical mirror of the monochromator focuses the light on the exit slit in the vertical plane. The horizontal size of the beam on the sample can be adjusted down to 100 µm by means of two sets of independently movable slits. The resolving power is $E/\Delta E > 8000$ at 400 eV and $E/\Delta E = 3000$ above 900 eV with a photon flux greater than $5 \cdot 10^{10}$ photons/s at best resolution in the range of 200-450 eV, decreasing down to 10^{10} photons/s at 1200 eV. In the endstation, the sample is placed in a manipulator with four degrees of freedom (three perpendicular translations and rotation around a vertical axis). The manipulator is equipped with three stages: a Low-Temperature one (LT), which allows cooling down to 60 K during measurements, a Rotatable one (RT), which allows rotating the surface of the sample around an axis parallel to the photon beam, and a High-Temperature one (HT), which allows heating up to 700 K during measurements. XAS measurements here presented were all collected in TEY mode, measuring the drain current from the sample to ground with a Keithley 6514 picoammeter, although measurements in TFY are also possible with a photon detector. An identical instrument measures the drain current from a fine grid (*mesh*) placed upstream the photon beam, which is used to normalize the photon flux for varying incident energy. A magnetic field can be applied in the LT and RT stages parallel to the sample surface with a small electromagnet placed on the manipulator, able to provide a field of 20 mT in continuous mode, or up to 100 mT in pulsed mode. XMCD spectra were recorded at remanence, measuring the TEY after alternating magnetic field pulses at each energy point of the spectra. XPS measurements can be done in all the stages with an Omicron EA 125 hemispherical analyzer, equipped with 7 channeltrons. The angle between the incident photon beam and the analyzer is fixed and equal to 45°, which means that for 45° of photon incidence the electron emission is normal to the surface. The sample holders are hooked to the stages of the APE-HE manipulator by means of two pins. Using specific sample holders (see figure 2.6) these pins provide two separate electrical contacts to the sample, which can be used for applying a voltage or a current. The endstation is hence fully equipped for *in-operando* characterizations, in which spectroscopic measurements are performed in combination of applied electric and magnetic fields. Typically, voltage-current sweeps are measured using a Keithley 6487 picoammeter/voltage source. For the experiments described in the following chapters, the bottom of the ferroelectric substrate was glued with silver paint to the sample holder, also providing electrical connection with the first lead of the sample holder. The surface of the sample (the magnetic film) was connected to the second lead with a gold wire, also glued with a drop of silver paint. Since the magnetic film is much more conductive than the ferroelectric crystal, the two contacts can be used to apply a voltage across the thickness of the ferroelectric. Current-Voltage characteristic curves can be measured *in-situ* with the sample in the measurement position, right before or after the spectroscopic measurements. For TEY detection, the voltage source was disconnected and the drain current was measured from the pin connected to the surface of the sample.

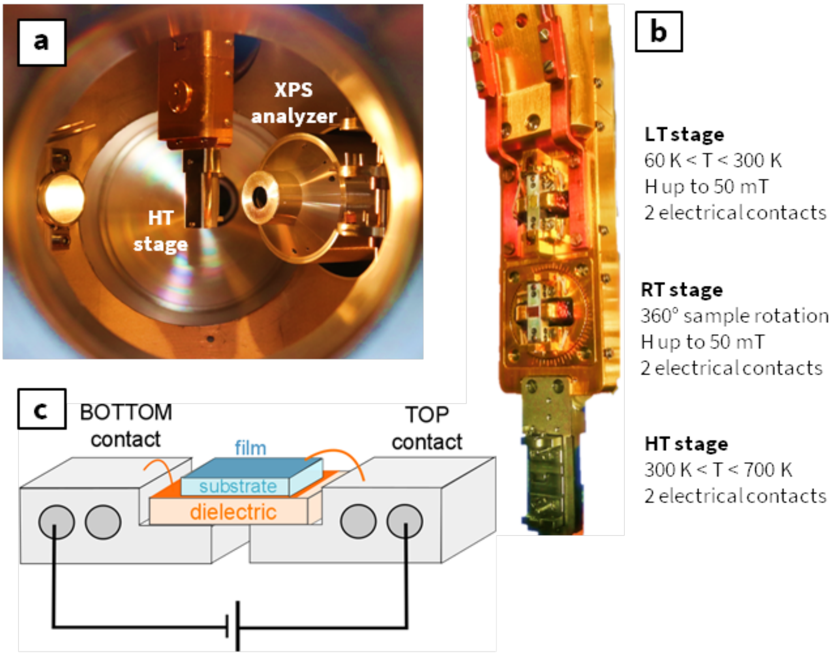

Figure 2.6: **a** - picture of the the APE-HE endstation. The X-ray beam enters in he chamber from a flange opposite to the viewport from which the photo was shot. **b** - close view of the manipulator. **c** - schematic of the sample holder for *in-situ* electrical poling, as used for out-of-plane polarization of ferroelectric substrates. Electrical contacts, usually made with silver paint and gold wires, are shown in orange.

MBE Cluster

A cluster of UHV chambers that can exchange samples for growth and analysis is also located inside the experimental hall of Elettra, in proximity but not connected to the APE beamline [56]. The cluster is composed of three different chambers: one MBE chamber dedicated to the growth of oxides (OxMBE), one multi-purpose chamber equipped with the standard tool for sample preparation in UHV condition, masked MBE deposition of metals and MOKE characterization (MASK), and a final one devoted to XPS analysis (VolPE). Samples can be moved between the three chambers in UHV conditions, allowing for a multi-technique step-by-step characterization of heterostructures. A schematic of the apparatus is shown in figure 2.7

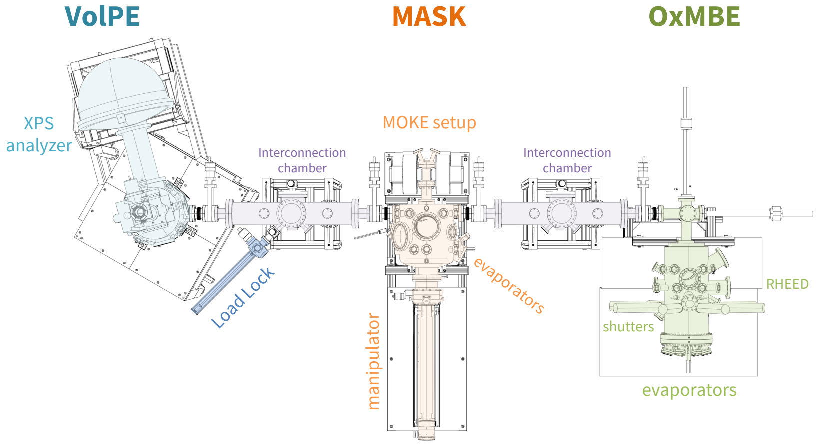

Figure 2.7: Technical design of the MBE Cluster, as seen from above.

The XPS chamber is a standard UHV chamber equipped with one close cycle cryostat that allows the control of the sample temperature in a range between 25 and 300 K. X-rays are generated by an non-monochromatized double anode (Mg,Al) source. Electrons are collected by a hemispherical analyzer (mean radius 200 mm) equipped with a 2D-delay line detector (300 × 300 channels). The angle between the X-ray beam and the analyzer is 90°. The manipulator permit the rotation of the polar angle permitting the change from the (almost) normal emission condition to the grazing emission (and therefore from the grazing incidence of x-rays to normal incidence). In the OxMBE chamber single elements are evaporated from Knudsen cells. The atomic fluxes can be roughly calibrated with a quartz microbalance. For the growth of pervoskite oxides (formula ABO_3), the temperature of the cells is kept fixed, and the molecular beams are shuttered sequentially to grow the alternating stack of AO and BO_2 atomic planes along the (001) direction. The time during which each shutter remains open is adjusted according to the deposition rate. The background oxygen pressure is provided through a nozzle placed few centimetres from the sample surface. The deposition of individual monolayers is monitored *in-situ* by RHEED, which also allows a calibration of stoichiometry within 1% following the method developed by Schlom and co-workers [57]. The shape of the RHEED oscillations is indicative of the ratio between A and B atoms deposited: the flux of the elements can be adjusted in order to have a stable and reproducible pattern. Also the deposition of fractional unit cell for each shutter cycle will manifest as a beat frequency in the RHEED fluctuations. After deposition of a calibration sample, whose thickness is measured *ex-situ* by e.g. X-Ray Reflectivity (XRR), the shutter times can be adjusted in order to have the desired correspondence 1 unit cell/1 RHEED oscillation, with the correct stoichiometry. LSMO thin films discussed in the next chapter were deposited following this procedure. During deposition the substrate was heated to 1000 K in a background ozone pressure of 10^{-7} mbar. The manipulator of the MASK chamber hosts three stages for the sample holders. In the first one (HT-stage) the sample can be heated up to 900 K by electron bombardment, and can be used for annealing and MBE deposition at high temperatures. Similar to APE-HE, there are two separate contacts for *in-situ* electrical characterization or bias. A second stage is equipped with a shadow mask system that allows the direct evaporation of patterned film of micrometric size. This may be used to deposit *in-situ* electrodes or markers on the surface of as grown samples. Masks are fixed to standard sample holders, and can hence be changed with ease without breaking the vacuum. The chamber is also equipped with a sputtering system for surface cleaning and a standard LEED/Auger apparatus. Finally, a third stage is used for longitudinal MOKE characterization. The sample can be translated in a narrow section of the vacuum chamber, which fits inside the gap of an electromagnet able to provide a field up to 0.8 T parallel to the sample surface. The helium-flow cryostat on the manipulator can cool the sample down to 5 K, and the azimuthal angle can be rotated by 360° for a full characterization of the in-plane anisotropy. The optical components are placed on an optical table just outside the chamber. The incoming and reflected laser beams enter and exit the vacuum chamber through specific windows. The light from the laser can be modulated either in intensity, by a mechanical chopper, or in polarization, by a photo-elastic modulator. The modulation frequency serves as a reference for a lock-in amplifier, which filters out the signal of the detector from the spurious noise coming from the environmental light. Two different wavelengths are available: 632 nm (red) and 405 nm (blue). The same set-up can be used for *ex-situ* MOKE characterization at room temperature. Fe_xMn_{1-x} thin films discussed in chapter 4 were deposited in the MASK chamber by MBE co-deposition from Fe and Mn crucibles on [001]-oriented pristine PMN-PT single crystal substrates ($5\times5\times0.5$ mm^3) at room temperature, with a base pressure of $2\cdot10^{-10}$ mbar. The x ratio was modulated by varying the deposition rates of the Mn evaporator, which were previously calibrated by quartz microbalance. The deposition rate was fixed at $1.9\,\text{Å}\,\text{min}^{-1}$ for the Fe evaporator and ranged from 0.19 to $1.9\ \text{Å}\,\text{min}^{-1}$ for the Mn evaporator. Samples were then capped by a 3 nm thick MgO layer with $0.57\,\text{Å}\,\text{min}^{-1}$ deposition rate.

2.4.2. Others

MOKE microscopy

Imaging-magnetometry measurements by micro-MOKE were performed in the Nanomagnetism Laboratory of the Politecnico di Milano. The microscope is an optical wide-field polarization microscope (Zeiss Axiotron II) customized in-house for Kerr microscopy. The magnetic field was applied in the sample plane by means of a calibrated electromagnet (up to 70 mT). Images are acquired by a high-resolution, high-sensitivity, and low noise digital CMOS camera by Hamamatsu (ORCA-spark C11440-36U). The magnetic hysteresis loops are obtained by selecting an arbitrary region of interest and thus integrating the intensity collected by the corresponding pixels using the camera as a conventional photodetector. The signal for each pixel is proportional to the magnetization along the sensitivity direction, which is parallel to the externally applied magnetic field in these measurements. Several magnifications are available using different objectives: 20×, 50×, 100×. With the 100× objective, each pixel corresponds to an area of 85×85nm^2 of the sample surface.

PEEM at I06 beamline

PEEM measurements on Fe$_x$Mn$_{1-x}$ samples were performed on the Nanoscience Beamline I06, located at the Diamond Light Source [58]. Exploiting the brightest region in Diamond's spectrum, its two APPLE II undulators can provide circularly polarized X-rays in the range 100 - 1300 eV with a photon flux around 10^{12} photons/s, resolving power $E/\Delta E = 10000$ at 400 eV and a micrometer spot size on the sample. The typically achievable lateral resolution is 50 - 100 nm. Images were acquired both in 10 µm and 50 µm field-of view, with an X-ray beam footprint of a similar size. The samples are mounted on customized cartridges and are kept in position by molybdenum caps with a hole in the center, through which X-rays and electrons can pass. Since the cap and the bottom of the cartridges are electrically insulated, an electric field can be applied *in-situ* between the surface and the back of the sample. In this way the ferroelectric polarization was switched using a high-voltage power supply, before the acquisition of a new set of images.

3. Strain-induced magnetization control in LSMO/BTO heterostructures

This chapter resumes the first of the two main original studies which are the core of the thesis: the one concerning the perovskite LSMO/BTO heterostructure [59]. Some general remarks on the interest in this class of systems were anticipated in the first chapter. The first section will introduce the two materials that were studied. At first an introduction to the complex physics of manganites and LSMO in particular will be presented, followed by a summary of the crystallographic phases of BTO. Since several reports on this system are present in the literature, section 3.2 summarizes the known results. The scope is also to highlight the element of novelty of the present work, which consists of the following finding: the tuning of applied strain perturbs the magnetic properties of manganites, and it can even be used to induce a magnetic phase transition. An active control of the applied strain for this purpose is here demonstrated. The experimental data are presented in section 3.3 followed by supporting ab-initio calculations. Finally, the results are discussed and interpreted in section 3.4.

3.1. Materials

Manganese oxides with perovskite structure show rich and interesting physics, and have been widely investigated [60]. They can be considered by now an emblematic example of a “strongly correlated magnetic oxide”. Despite the rich literature on this topic some aspects of manganites are still not completely understood, as will be discussed below, and interfacing manganites with other materials provides continuously new interesting observations.

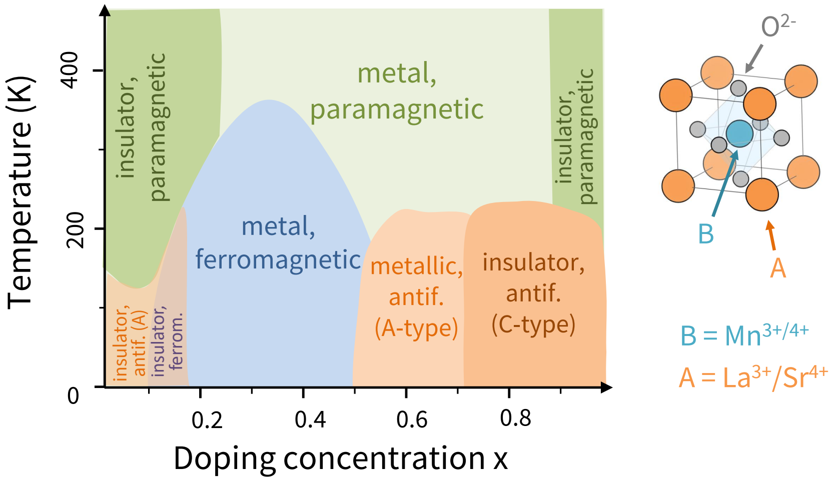

Figure 3.1: Schematic of the bulk LSMO phase diagram as a function of doping concentration x and temperature. A sketch of the cubic perovskite structure is represented on the right.

In the perovskite structure ABO_3 (represented in figure 3.1) Mn ions occupy the B site at the center of the oxygen octahedron. Since manganese ions can have different valence states (Mn^{3+}, Mn^{4+}), the A site can be occupied both by trivalent (La, Pr, Y...) or divalent cations (Ca, Sr, Ba...). Compounds like $\mathrm{LaMnO_3}$ (LMO) and $\mathrm{SrMnO_3}$ (SMO) are charge-transfer insulators, and the *super-exchange* interaction determines the antiferromagnetic ordering (of different kind for LMO and SMO) of the spins. In mixed-valence manganites, such as $\mathrm{La_{1-x}Sr_xMnO_3}$ (LSMO) or $\mathrm{La_{1-x}Ca_xMnO_3}$ (LCMO), a variety of behaviors are encountered as a function of temperature and doping level x, as summarized in the phase diagram in figure 3.1. The main feature is the appearance of a ferromagnetic and metallic state in the doping region $0.2 < x < 0.5$, and in LSMO the maximum T_C, obtained for $x = 0.35$, exceeds room temperature. The interplay between antiferromagnetic-insulator and ferromagnetic-metal states has been described with the *double-exchange* mechanism. This is illustrated in figure 3.2. If the valence of adjacent Mn cations is different, electrons may hop between the two, reducing the kinetic energy contribution. However this would be favorable only if the ordering is ferromagnetic, because spin is preserved in the hopping process and in case of antiferromagnetic ordering an energy cost due to the Hund coupling should be paid. In a nutshell: in the case of mixed-valence, the ferromagnetic ordering may enable the minimization of kinetic energy. Mean-field models correctly predict the highest T_C for $x = 1/3$. On the other hand if all Mn ions have the same valence, hopping is excluded due to the Coulomb repulsion, and the ground state is antiferromagnetic. At intermediate doping levels, electrons may localize with a long range correlation (charge−ordering). The presence of different d orbitals (degenerate or not, according to the structure) characterized by different hopping amplitudes or hybridization leads to *orbital-ordering*. Orbital and charge ordering can, of course, be related to particular arrangements of the spins. Even if a simple model describes correctly some features of the phase diagram, many other experimentally observed phases escape such simple analysis. This is not surprising, since the chemical doping not only introduces extra charges, but also disorder and structural deformations, which ultimately affect many coupling parameters of the interactions.

Manganites attracted much interest because they display the Colossal Magneto-Resistance effect (CMR): application of an external field may induce dramatic changes in the conductive properties. A first naïve interpretation is based on the aforementioned picture: if an external field can induce a ferromagnetic alignment, metallic conductivity will follow through. Indeed the CMR is stronger in regions of the phase diagram

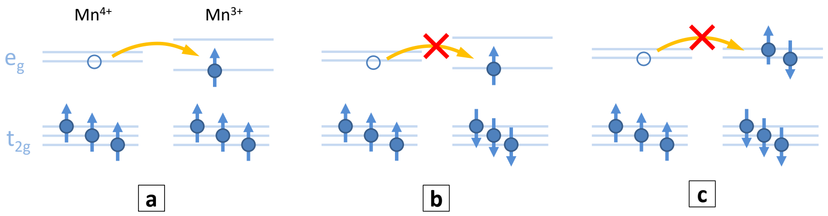

Figure 3.2: Visual representation of the double-exchange mechanism. **a** - hopping between two sites is possible if they have a different valence and the atoms are coupled ferromagnetically. **b** - hopping is not favored if the coupling is antiferromagnetic, because of the energy associated to the on-site Hund coupling. **c** - hopping between two sites with the same valence state is hindered by the strong intra-atomic Coulomb repulsion.

close to a phase transition (e.g. in LCMO for $x = 0.2$ at low temperatures), where the competition between the phases is tight, and a relatively weak perturbation (a field of 1 T correspond to only 50 µeV in terms of Zeeman splitting) can have strong effects. Nowadays it is understood that in the CMR regime manganites display phase-separation [61], i.e. the different competing ground states form separated “clusters” that coexist on a microscopic scale. The external field produces an imbalance between the phases, and the change in conductivity originates from percolation within conductive clusters. A detailed description of these phenomena requires the understanding of the several different phases and their competition, which is a challenging theoretical task. This brief discussion of the CMR effect should ultimately emphasize the following concept: the physics of manganites is determined by several competing interactions, which include the electrons, their spin, orbitals and the lattice. This fact makes them interesting building blocks for multiferroic heterostructures, because we can act on their magnetic ordering through different channels. LSMO is among the manganites the one with a wider bandwidth, and as a consequence its metallic/ferromagnetic phase is quite robust. Compared to other materials like the parent LCMO the competition of phases is apparently less intricate, and CMR effects are weaker. However, LSMO is probably the most studied member of the manganite family. This is because for the “optimal” doping $x = 0.35$ the T_C is above room temperature, and at lower temperatures it is predicted to be a half-metal (i.e. the mobile electrons are 100% spin polarized). These properties make LSMO appealing as a candidate for spintronic applications. Although ferromagnetism is intrinsically robust in this compound, it is still possible to perturb its state in several ways (e.g. through strain) to achieve an electrical control of its magnetic properties close to room temperature.

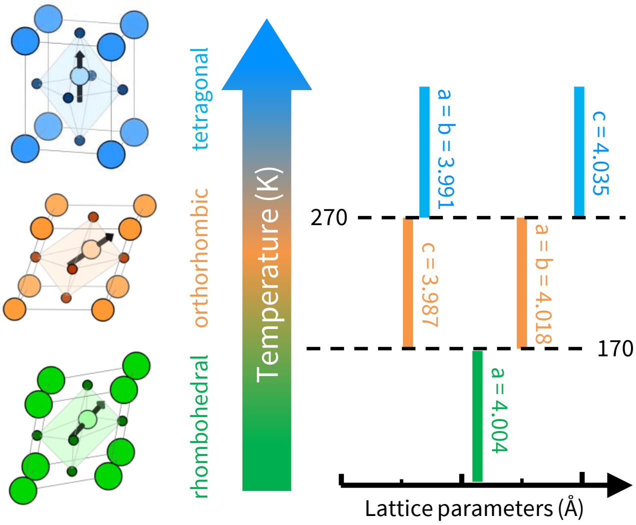

Figure 3.3: Sketch of the different ferroelectric crystallographic phases of BTO as a function of temperature. Corresponding bulk lattice parameters, referred to a pseudo-cubic perovskite unit cell, are reported on the right panel.

$BaTiO_3$ (BTO) is one of the first ferroelectric ceramics ever discovered, and hence one of the most studied. Like other ferroelectrics with a similar structure, the position of the transition metal cation (in this case, Ti^{4+}) is shifted from the center of the surrounding oxygen octahedral cage. As a consequence, the centres of mass of the positive and negative charge distributions are no more coincident. Correspondingly the inversion symmetry is broken inducing a deformation of the (otherwise cubic) unit cell along the direction of the electric dipole. For different temperatures, BTO presents four different crystallographic phases, as summarized in figure 3.3. Above 400 K the structure is cubic and the compound is not ferroelectric. Between 400 and 270 K the structure is tetragonal, which means that the unit cell is elongated along one of the $\langle 100 \rangle$ directions (the edges of the cube). Between 270 and 170 K the structure is orthorhombic, so the deformation is along the $\langle 110 \rangle$ directions (face diagonals). Finally below 170 K BTO is rhombohedral, and the deformation is along ⟨111⟩ (main diagonal of the cube). Microscopy studies have imaged the ferroelectric domain structures of BTO single crystals. Commonly, a striped pattern of alternating in-plane and out-of-plane domains is observed at room temperature [62].

3.2. State of the art

The fact that strain can affect the magnetic and electronic properties of manganites is understood. A first evidence comes from the fact that thin films grown on different substrates shows changes in magnetic moments and Curie temperature as a function of the effective epitaxial strain [63]. The interesting question becomes the following: it is possible to actively tune the strain to (reversibly) change the properties of a sample?

To our knowledge, the first experiment of this kind is the one of Lee et al., published in 2000 [64]. They grow a 50 nm thick LSMO film (optimally doped, $x = 0.33$) on a BTO (001) substrate. Due to the lattice mismatch between bulk LSMO and BTO (nominally around +3%) the resulting films are partially relaxed. However, from diffraction measurements the authors still observe an in-plane +1.5% expansion and an out-of-plane -1% contraction of the LSMO lattice parameters. The interesting results are that in correspondence of the BTO structural transitions, both the resistivity and the magnetic moment of the film (as measured by SQUID magnetometry) show abrupt discontinuities. This was a first demonstration of how the magnetic properties of the LSMO film can be modified acting on the structure of the substrate. However, the trend of both resistivity and magnetization are very similar to what would be expected for bulk LSMO (i.e. metallic and ferromagnetic), except for the aforementioned anomalies at some specific temperatures. This means that structural changes of BTO for sure perturb the magnetic film, but do not induce any phase transition. It should also be mentioned that the authors recognize the need of two different parameters to describe the strain applied to LSMO when BTO is in the tetragonal and orthorhombic phase.

Another important work is the one of Thiele et al. in 2007 [65]. In this case, the authors grow manganites thin films (both LSMO and LCMO) in the thickness range 20-50 nm on rhombohedral PMN-PT (001) substrates.

Even in this case the films are partially relaxed, and the thinner film is the one with higher resulting strain. The authors measure the change in magnetization as a function of an electric field applied across the PMN-PT substrate, which induces a change in the lattice parameter because of the piezoelectric effect. The relation between applied strain and magnetization is shown to be linear. Contextually, a change in T_C with the applied field is observed. This work is relevant because it is the first demonstration of an electrical control of magnetism in manganites, mediated by strain. However, since the experiment relies on the piezoelectric effect of PMN-PT, the induced changes disappear when the electric field is removed.

In the same year, another reference work is the one of Eerenstein et al. [66] The sample under investigation is a 40 nm thick LSMO film deposited onto a BTO (001) substrate. At fixed temperature, they measure the magnetization during the application of an electric field across the thickness of BTO. After a certain threshold voltage, an abrupt change in magnetization is measured. Since no changes are observed for further increase or reversal of the electric field, this effect is ascribed to the change in strain induced by rotation of BTO ferroelectric domains from in-plane to out-of-plane. Since the field is only applied out-of-plane, after one switch the sample has to be “reset” by heating BTO until it transforms to cubic. Importantly, the authors demonstrate with diffraction data that the applied electric field results in a change in the ferroelectric domain distribution of BTO when it is in the tetragonal phase. A very similar experiment was reported by Alberca et al. in 2016 [67] but with a 10 nm thick LCMO film, with comparable results. In addition, by means of polarized neutron reflectometry, the authors observe inhomogeneities in the magnetic properties of the film across its thickness.

In 2014, Chopdekar et al. [68] use PEEM to image the magnetic domains of a 30 nm thick LSMO film deposited on BTO (001). What is found is that the striped ferroelectric domain pattern typical of BTO is imprinted onto the magnetic domain structure of LSMO. Both the strain imposed by the substrate and the direction of the magnetization contribute to an X-ray Linear Dichroism effect (XLD), whose contrast is strongly correlated with the one originating from XMCD. Finally, they show that poling the BTO out-of-plane modifies the striped pattern observed, as a consequence of ferroelectric (and correspondingly ferromagnetic) domain rotation.

In the following year, another article was published by the same group [69] regarding a LSMO thin film (8 nm) grown on PMN-PT(110). With this crystal cut of the substrate, the application of an out-of-plane electric field allows toggling the ferroelectric polarization between in-plane and out-of-plane, and the induced change in strain is non-volatile. The authors show a decrease in the XMCD signal for the in-plane polarized substrate. Measurements performed in several geometries show that this effect is not only due to a rotation of magnetic anisotropy, and indeed it is also accompanied by a decrease of T_C by $10\,\mathrm{K}$. This represents an important demonstration of non-volatile electrical control of magnetism mediated by strain in manganites.

One last work which deserve mentioning is the one of Guo et al. (2017) [70] that focuses on LSMO/BTO superlattices. In particular they use high-resolution transmission electron microscopy (HR-TEM) to study the atomic structure of these samples. Strain appears to be independent from the thickness of the LSMO layers, while significative changes are seen in the oxygen octahedrons rotation pattern. As the thickness is decreased, the tilt of the octahedra is reduced, accompanied by a deterioration of the magnetic properties. Surprisingly, at very low thickness (4 unit cells) the magnetic moment is partially restored, and a polar distortion is observed in the LSMO layer. However, to our knowledge, no further experimental evidence of ferroelectricity in LSMO was published since then. This work shows how the magnetic properties of manganites can be influenced by structural parameters other than the simple epitaxial strain.

3.3. Results

The experiment described here concerns 30 unit cells (u.c.) thick LSMO thin films (optimally doped, $x = 0.35$) deposited on an unpoled commercial BTO (001) substrate. These films were grown by Molecular Beam Epitaxy, according to the method described in chapter 2. The substrate temperature was kept at $1000\,\mathrm{K}$, and the growth was carried on in an ozone atmosphere with pressure $10^{7}\,\mathrm{mbar}$. The base pressure of the deposition chamber was about $10^{-10}\,\mathrm{mbar}$. RHEED was used to monitor the layer-by-layer growth of the film, confirming that LSMO grows epitaxially cube-on-cube on the BTO substrate along the [001] direction. One sample was characterized by XAS and XMCD, and it was capped by a thin gold layer ($2\,\mathrm{nm}$) for the *in-operando* measurements. A second sample, nominally identical but without the gold layer, was characterized by X-ray Diffraction (XRD) and its resistance vs. temperature was measured in a four-probe configuration.

3.3.1. Properties as a function of temperature

XAS and XMCD measurements at Mn $L_{2,3}$ edges were performed at Advanced Photoelectric Effect beamline high energy branch (APE-HE). Total electron yield (TEY) detection system was used, which determines a probing depth of about 8 nm through the LSMO layer. Since the film is 12 nm thick, our XMCD measurements probe most of the volume of the film. Absorption measurements have been taken with circularly polarized radiation, with the sample normal at 45° with respect to the incident beam. At each energy point of the absorption spectra, TEY was measured at remanence, after alternating magnetic field pulses of ±20 mT applied in the plane of the sample surface; the difference between the two spectra gives the dichroic signal of the LSMO layer. The data are presented by normalizing to 1 the sum of the intensity of the L_3 lines of the polarization-averaged spectrum. The XMCD signal expressed in percentage takes into account the angle of 45° between the photon angular momentum and the sample magnetization, as well as the 75% circular polarization degree of light.

XAS and XMCD spectra were collected as a function of temperature. First the sample was characterized at room temperature, and then cooled to 90 K with a liquid nitrogen cooling system. The temperature was slowly raised up to room temperature again, and spectroscopic measurements were performed throughout this process. The results are summarized in figure 3.4. The XAS spectrum presents two broad multiplets, due to the large Mn $3d$ bandwidth, as expected and previously reported for optimally doped LSMO [71]. When passing across the BTO structural transitions, no changes were observed in the Mn $L_{2,3}$ lineshape, as shown in figure 3.4-**a**. Hence, the chemical environment and the valence state of manganese are preserved for all the temperatures. However, some important changes are observed in the intensity of the XMCD spectrum. No dichroism is detected when BTO is in the tetragonal phase (blue color in the graphs, $T > 280\,\mathrm{K}$) or in the rhombohedral one (green color, $T < 180\,\mathrm{K}$), but a clear dichroism signal (3%) is measured in the intermediate orthorhombic phase of BTO (orange color, $180\,\mathrm{K} < T < 280\,\mathrm{K}$). Our detection limit is 0.5-0.3%. These measurements testify that the structural phase

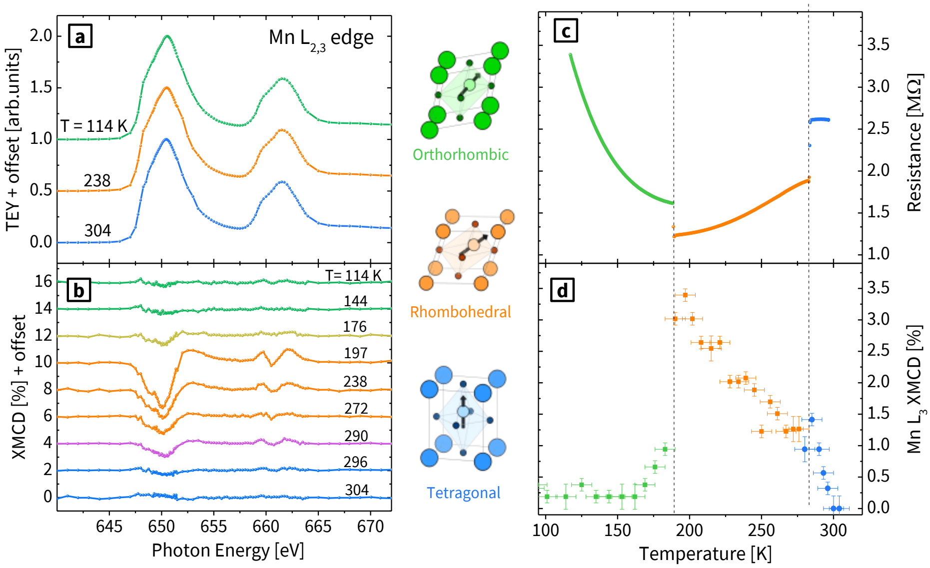

Figure 3.4: **a** - Mn $L_{2,3}$ XAS spectra acquired for various temperatures corresponding to different BTO structural phases, for the pristine case. **b** - corresponding XMCD spectra. **c** - Temperature dependence of the LSMO/BTO resistance with BTO in the pristine phase. **d** - XMCD signal on the Mn L_3 edge. Dashed lines correspond to BTO structural transitions.

of BTO affects the magnetic ordering of the LSMO overlayer. Particularly remarkable is the sharp transition to a ferromagnetic phase that is observed when the temperature is increased above 180 K, corresponding to the BTO rhombohedral to orthorhombic structural transition. Resistivity measurements as a function of temperature also show changes for the different crystallographic phases of BTO (see figure 3.4 - **c**). The resistance presents some discontinuities in correspondence to the transition temperatures, as reported by Lee et al. [64] However, the general trend is also different in the three phases. When BTO is rhombohedral, resistance decreases for increasing temperature, which is a typical insulating behavior. The opposite is found in the orthorhombic phase, as expected for a metallic behavior. These results are well consistent with the XMCD data, as expected for LSMO: ferromagnetism is usually related to metallicity in its phase diagram, while the antiferromagnetic state is insulating.

3.3.2. *In-operando* measurements

In a new experimental set-up the sample was mounted on a specifically designed sample holder that allows *in-situ* application of an electric bias through two separate contacts. The back of the sample was glued to the sample holder with silver paint, which was used as a bottom contact. The LSMO film, covered by a ultra-thin gold layer, was used as a top contact. Two-point current vs. voltage characteristics are measured with a Keithley 6485 picoammeter/voltage source, sweeping the voltage from 0 to a maximum value of ±200 V, and then back to 0. A current peak is measured in correspondence of the switching of the ferroelectric polarization of BTO. This peak is not measured anymore in subsequent sweeps with the same polarity, testifying the non-volatility of the effect. However, the application of an inverse voltage determines the reversible switching of the ferroelectric polarization. This electric behavior is summarized in figure 3.5.

The ferroelectric polarization of BTO was switched *in-situ*, when the sample was in the endstation of the APE-HE beamline. XMCD spectra were collected at zero bias applied, in the same experimental conditions as described above. For each temperature, spectra for “up” and “down” polarization were collected, one immediately after the other. The results are summarized in figure 3.6. Out-of-plane polarization of BTO does not affect the magnetic properties for the rhombohedral and orthorhombic phases: in the former, still no XMCD signal is detected, in the latter, a

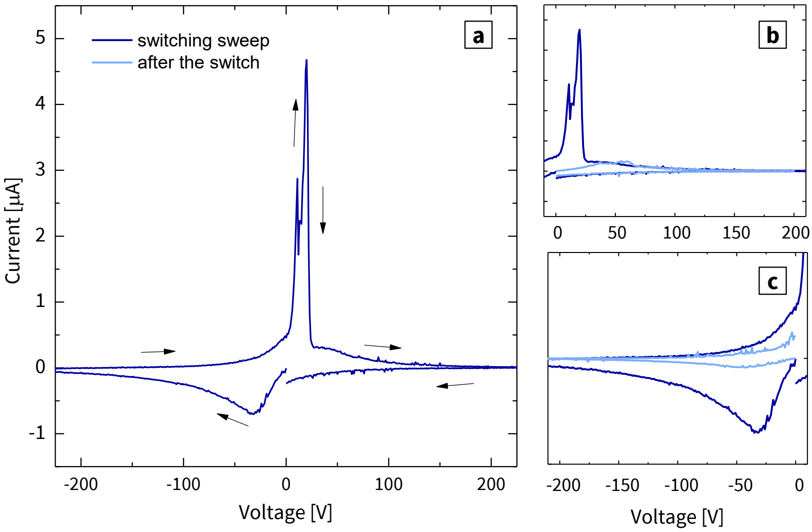

Figure 3.5: **a** - Current vs voltage characteristics of the BTO substrate during *in-situ* out-of-plane polarization. Arrows show the direction of the sweep for the black curve. **b** - comparison between a switching event setting the polarization "up" and a positive-only electric field sweep after the switch. **c** - same as before, for polarization "down" and a negative-only sweep.

signal is still visible, with comparable intensity to the unpoled case. On the other hand, a dichroic signal (0.7%) is clearly detected at room temperature for the tetragonal phase, which was absent in the unpoled state. For all the temperatures, no differences are observed by reversing the out-of-plane polarization, which is compatible with a completely strain-driven effect, as will be further discussed in the next sections.

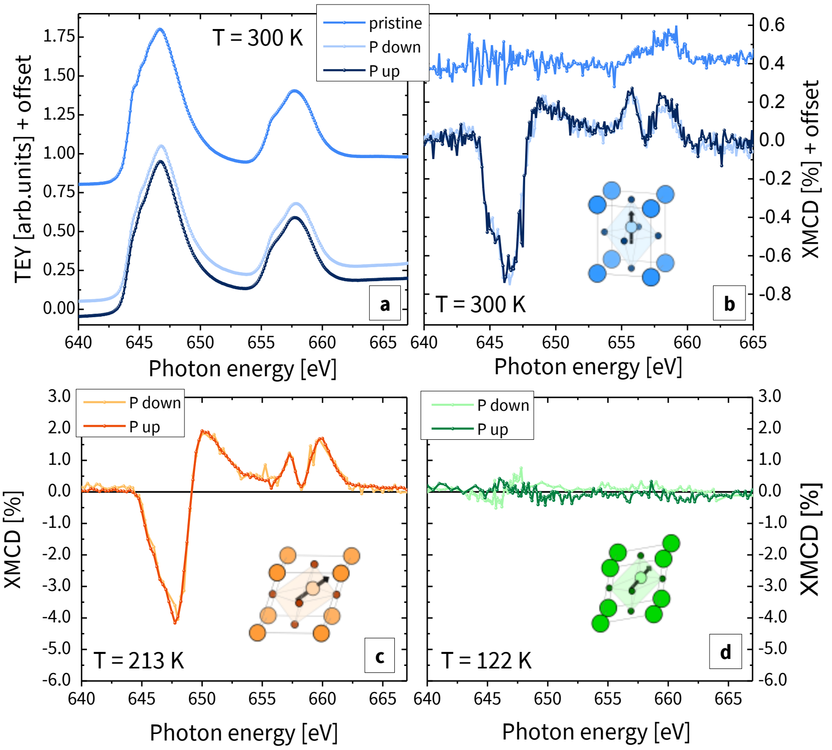

Figure 3.6: **a** - Comparison of the Mn $L_{2,3}$ XAS spectra for BTO in the pristine state and polarized with positive or negative bias in tetragonal phase. **b** - Corresponding XMCD spectra. **c** - Comparison of the XMCD spectra for BTO polarized with positive/negative bias, in the orthorhombic phase. **d** Same for the rhombohedral phase.

3.3.3. Structural characterizations

The full-width-half-maximum (FWHM) of the RHEED (01) diffraction spot, shown in figure 3.7, was recorded to monitor the dynamics of the crystalline structure of the film during deposition. A broadening of the diffraction spots is observed after 10 u.c., symptom of the increasing disorder originating from the formation of defects and/or surface roughening. The formation of defects for increasing thickness can be expected given the large mismatch (2.6% - 3.3%, depending on the structural phase) between BTO and LSMO, and may accompany the tendency to change the lattice parameters towards bulk values (relaxation).

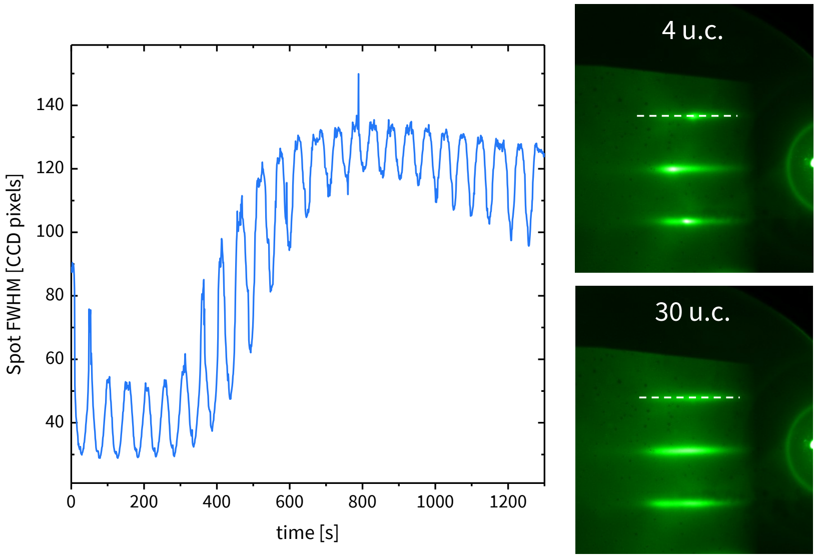

Figure 3.7: Evolution of the full width half maximum of RHEED (01) diffraction spot during the growth of LSMO, starting from the 5th unit cell. The graph was obtained from the intensity profile along the white dashed line shown in the corresponding images.

A more detailed structural characterization was obtained by XRD. Measurements in Bragg-Brentano geometry were performed with a PANalytical's EMPYREAN instrument with Cu-K_α radiation at room temperature, i.e. with BTO in tetragonal phase. In the High-Intensity mode the incident radiation is not monochromatic. High-Resolution XRD measurements were obtained in a double-axis configuration, using a 4-bounce Ge(220) monochromator to select only the Cu-$K_{\alpha 1}$ line. Figure 3.8 - **a** shows the XRD $\theta - 2\theta$ diffraction scan in high intensity mode at room temperature for as-deposited LSMO/BTO. Non-polarized BTO shows the expected presence of domains elongated both in-plane, i.e. (100) and/or (010), and out-of-plane, (001), in tetragonal phase. The corresponding calculated lattice parameters of BTO are 3.991 Å and 4.035 Å respectively, in perfect agreement with the data reported in literature [62, 72]. By comparing the relative intensities of the in-plane and out-of-plane peaks, we infer that the majority of domains are oriented in-plane. Regarding the LSMO thin layer, its (002) peak indicates a pseudo-cubic out-of-plane lattice parameter of 3.78 Å, much smaller compared to the bulk value of 3.87 Å [73]. This is due to the substrate-induced in-plane tensile strain, which causes a decrease of the out-of-plane lattice parameter. The out-of-plane lattice parameter here reported is the lowest among those reported in literature (see the works cited in section 3.2) for thin films deposited on BTO or PMN-PT. This is consistent with the fact that the thickness of the film in this case (30 u.c.) is among the lowest reported on similar substrates, and hence the film is expected to be closer to the fully-strained state, and further from the completely relaxed state. Using the Poisson ratio $\nu = 0.36$ reported in literature [63], an expanded in-plane lattice parameter of 3.90 Å is calculated. Hence, despite the increased FWHM of the RHEED oscillations, the film appears to be far from the fully-relaxed bulk structure, and still clamped to the substrate. Finally, a reciprocal space map in high intensity mode around the (103) reflection is presented in figure 3.8 - **c**. These data confirm the partial relaxation of the film. Unfortunately the intensity of the reflection is very low, possibly because of the poor quality of the BTO substrate, and it's not possible to reliably estimate the in-plane lattice parameter.

$\theta - 2\theta$ scans of BTO (002) were acquired in high-resolution mode to testify the effect of the out-of-plane polarization. Firstly, the sample was set in the high temperature cubic phase, then cooled down to room temperature (tetragonal phase), both without applied bias voltage (light curve in figure 3.8 - **b**) or with an out-of-plane applied electric field of 400 V (dark curve). The two peaks reflects the presence of ferroelectric domains (and hence the long side of the tetragonal unit cell) oriented both in-plane and out-of-plane. What is observed is that although for the unpolarized state the majority of the domains are set in-plane, the application of a voltage changes the ratio of the two peaks. This is interpreted as rotation of domains towards the out-of-plane direction.

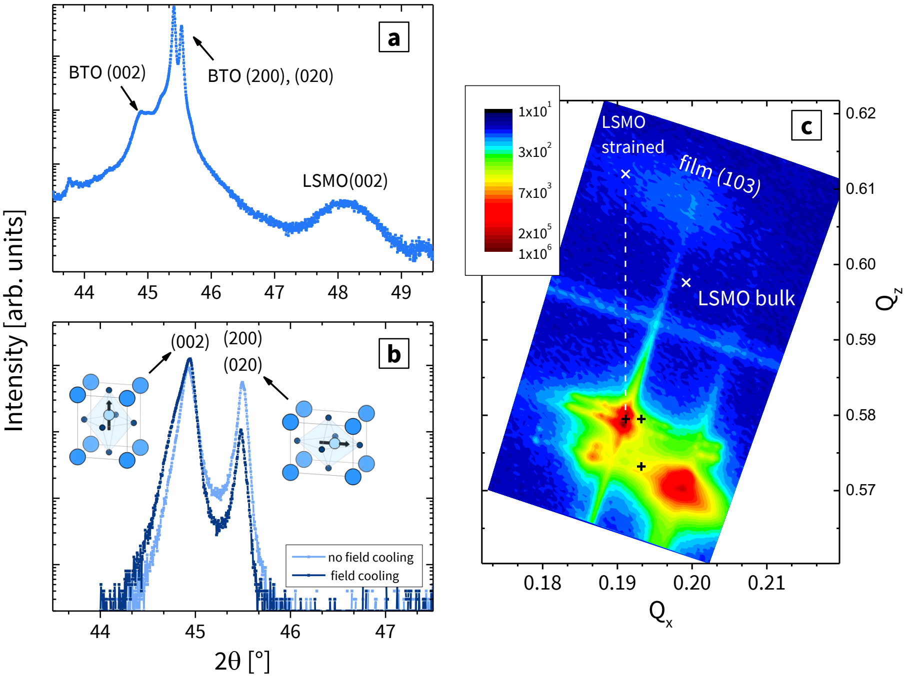

Figure 3.8: **a**- $\theta - 2\theta$ scan of LSMO/BTO sample, acquired at room temperature in a high-intensity configuration. It is possible to distinguish the different domains of the BTO crystal in the tetragonal phase, both out-of-plane and in-plane. Note that the BTO peaks are split into two components because of the presence of both $K_{\alpha 1}$ and $K_{\alpha 2}$ lines in the Cu X-ray source. **b** - $\theta - 2\theta$ scans in high-resolution configuration of LSMO/BTO sample without field cooling from the cubic phase (light blue) and after field cooling under applied 400 V (dark blue). On the side, schematics of BTO unit cells for (001) and (010). **c** - reciprocal space map around the (103) peak of the LSMO(30 u.c.)/BTO sample, obtained in the "high intensity" configuration. Twin peaks corresponding to $K_{\alpha 1,2}$ lines are visible for the substrate. The expected positions of the LSMOs peak for the bulk pseudo-cubic structure (a=3.88 Å) and the fully-strained film are marked with with white crosses. Black crosses mark the expected positions of the BTO substrate peaks.

3.3.4. *Ab-initio* simulations

First-Principles calculations of strained LSMO were performed in order to gain a better understanding of the complex observed phenomenology. The approach was the following: some constraints were imposed on the crystallographic structure of LSMO, which are supposed to mimic the effect of epitaxial strain, and the fully relaxed structures were calculated for different kinds of magnetic ordering. The total energy of the system in the various cases was then compared to understand the most preferable magnetic state as a function of the applied strain. Simulations were realized using Density Functional Theory (DFT) within generalized-gradient spin-density approximation, as implemented in the QUANTUM ESPRESSO code [74]. For our calculations we employed a basis set of plane waves and ultrasoft pseudopotentials with cut-off energies of 40 Ryd, $4 \times 4 \times 4$ k-point grid (corresponding to 32 ab-initio k points in the Irreducible Brillouin Zone) and Gaussian smearing of 0.005 Ryd. A $\sqrt{2} \times \sqrt{2} \times 2$ cell with tetragonal/orthorhombic $Pnma$ symmetry was assumed, with generic $a^- b^- c^+$ octahedral tilting pattern (this symmetry also characterizes the antiferromagnetic $LaMnO_3$ endpoint structure). The Sr doping level is 25% in all the calculations, which was treated by actual atomic substitutions. In the simulations, the interface plane lattice parameters a and b (either square or rectangular) were fixed, while the system was fully relaxed along the interface-perpendicular direction (c axis). A tight convergence threshold of 0.1 mRy/Bohr was imposed to the forces. Fully relaxed 20-atom supercells were used for all the examined magnetic orderings, which are: ferromagnetic (FM), A-type, C-type, and G-type antiferromagnetic (AFM); in this way the nearest-neighbor interactions along all the three directions was taken into account.

Two sets of simulations were performed: in the first set a squared substrate, i.e. with $a = b$, was imposed; this mimics LSMO grown on BTO at room-temperature when polarized out-of-plane, or even for the rhombohedral case if we ignore the small distortion angle involved. In the second set we allowed $a \neq b$ to explore a possible tetragonal-to-orthorhombic symmetry lowering for LSMO. This could mimic the strain imposed by the BTO substrate at room temperature when polarized in-plane, or when it is in the orthorhombic phase. The results are summarized in figure 3.9. Panel **a** shows the energy per formula unit as a function of the a parameter in the case $a = b$ for the various magnetic ordering. We see that ferromagnetic (FM) and A-type antiferromagnetic (A-AFM) orderings tightly compete

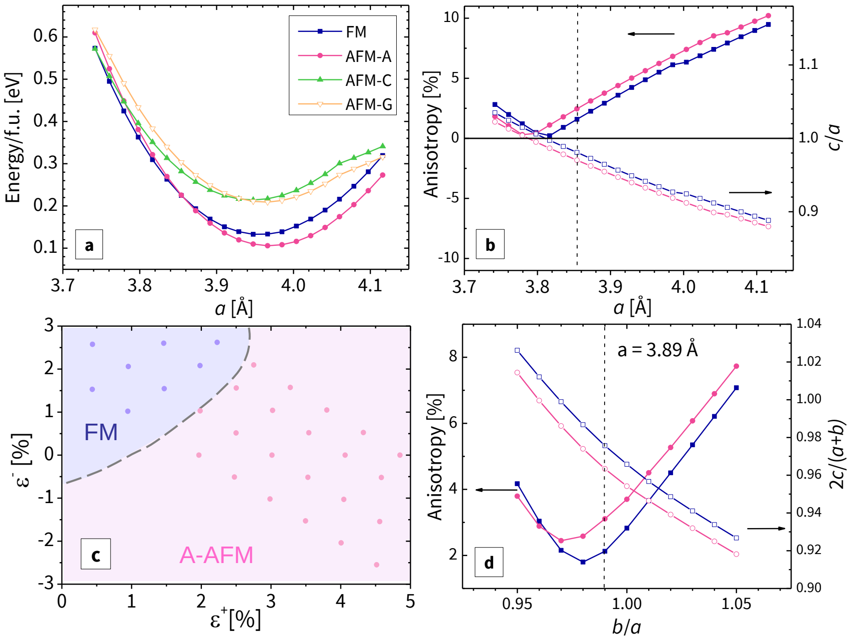

Figure 3.9: Calculations of a tetragonal LSMO film under planar strain. **a** - Energy per formula unit; **b** - Anisotropy factor (left axis) and c/a ratio (right axis). Calculations of orthorhombic $Pnma$ LSMO. **c** - Inferred phase diagram as a function of symmetric and asymmetric strain applied for bulk. Points represent values actually simulated. **d** - Example of anisotropy factor (left axis) and c/a ratio (right axis) for fixed a=3.89 Å. In **b** and **d** the dashed lines correspond to the a and b/a values in which the FM and AFM phases have the same energy.

in this range of parameters. The others are much higher in energy and can be ignored. A-AFM ordering is stabilized with increasing tensile biaxial strain (i.e. increasing a) while FM is strengthened by compressive strain (i.e. decreasing a). The tradeoff between the two occurs for $a = 3.87\,\text{Å}$. In their respective equilibrium structures, FM and A-AFM orders differ by an energy of 25 meV/f.u. Panel **b** shows that increasing a decrease the c/a ratio and as a consequence the anisotropy factor of the unit cell. For any given value of a, c/a is smaller for the A-AFM ordering, which hence is associated with a larger anisotropy. The results for orthorhombic LSMO (i.e. with rectangular substrate) are shown in panels **c** and **d**. The general trend observed in the calculations is that for $b/a < 1$ the FM phase gains stability over the A-AFM. The turn-around occurs at $b/a = 0.95$ for $a = 4\,\text{Å}$, and the b/a value approaches 1 as a is decreased. For $b/a > 1$, on the other hand, the A-AFM phase is further strengthened with respect to the FM phase.

3.4. Discussion

Magnetoelectric coupling mechanisms (see chapter 1): BTO is not magnetic, so one can exclude any exchange-mediated mechanism. The fact that no changes are observed in the lineshape of the Mn $L_{2,3}$ XAS spectra signifies that the chemistry of the compound is unaltered, and hence ion migration is absent. If charge-mediated effects would be responsible for the observed magnetoelectric coupling, significant differences for the two opposite electric polarities would be expected, but these are not observed. This is not surprising, since the thickness of the film is about 12 nm and the probing depth of the TEY detection is about 8 nm. Electrostatic effects previously studied in ferroelectric/manganites heterostructures lead to a general consensus on charge effects being screened within few unit cells in the LSMO layer [75–78]. The ensemble of the present results can be consistently explained by strain-mediated effects. This interpretation will be further discussed also in view of the DFT calculation results presented in the previous section. As already mentioned, the magnetic ground state in LSMO is determined by a competition between super-exchange, mediated by occupied t_{2g} orbitals, and double-exchange interactions, mediated by e_g orbitals, whose occupation is determined by doping. In bulk for $0.2 < x < 0.35$ double-exchange couples the spins in all the three directions, and the compound is ferromagnetic. This is associated with an almost isotropic rhombohedral structure. The effect of *in-plane* epitaxial strain is to break the degeneracy of the e_g states. Specifically, a tensile biaxial strain would lower the energy of the $x^2 - y^2$ orbital respect to the z^2, so that the electron density becomes anisotropic: it is mainly distributed in-plane. As a consequence, ferromagnetic interaction is strengthened within the plane, while super-exchange couples different planes antiferromagnetically. This results in A-type antiferromagnetic order, as predicted by simulations. What happens if then the strain is not biaxial? The magnetic ground state is actually determined by the anisotropy of the unit cell: ferromagnetism is favored by a more cubic-like structure. Then, starting from a high biaxial strain and a A-AFM ground state, decreasing one of the two lattice parameters (i.e. $b/a < 1$) would increase the c parameter, decrease anisotropy, and favour the FM ordering. Increasing b/a will instead increase the anisotropy (c decreases further) and strengthen the A-AFM state. This is indeed what emerges from the DFT simulations. It is evident how in this case it is necessary to describe the system with two parameters, which may be the in plane lattice constants a and b or, equivalently, two components of the strain tensor with different symmetry [64]. Figure 3.9 - **c** summarizes the results of the simulations in a phase diagram as a function of these strain parameters.

In light of the previous discussion, the experimental results can be interpreted. When BTO is in the rhombohedral phase, LSMO is subject to a high biaxial strain that drives it to a (presumably) antiferromagnetic state. At the transition to orthorhombic, one of the two lattice parameters decreases, favoring ferromagnetism, as detected by XMCD. And in the tetragonal phase? Actually it depends on the domain orientation. If the polarization is out-of-plane, the strain is biaxial but lower than in the rhombohedral case, so that the system is ferromagnetic. If instead the polarization is in-plane, one of the two parameters is increased, which hinders ferromagnetism. It is important to mention also that T_C for this thin, highly strained film is very close to room temperature, so we may equivalently describe the observed phenomenon for the tetragonal phase as a strain-driven shift of T_C. Out-of-plane polarization of BTO was shown to change the orientation of the ferroelectric domains, partially relieving the strain applied to the film. Coherently with this view, no changes are observed in the other two phases of BTO, where the electric dipole is not along one side of the unit cell but along a (face or body) diagonal. Hence domains cannot be categorized as “in-plane" or "out-of-plane”, and an electric field across the thickness of the substrate would not change the global strain applied to the overlayer. Another final aspect to be discussed is the smallness of the XMCD signal observed compared to the value around 20% in the case of unstrained LSMO (corresponding to a magnetization of 3.5 μ_B/Mn) [71]. As mentioned above, tensile stress in LSMO epitaxial films is known to decrease T_C, which implies that magnetization is severely reduced. Furthermore, our simulations show that AFM and FM orderings are in tight energetic competition for a wide range of lattice parameters. Several experimental and theoretical works (summarized in the review of Dagotto, Hotta, and Moreo [61]) have demonstrated the tendency of manganites to form an inhomogeneous state in which AFM and FM phases coexist, especially at the boundary of the phase diagram. Hence the changes of the Mn XMCD signal could be attributed to a disproportion of the FM fraction in the LSMO film, which is modulated by the substrate-induced strain. The smallness of this signal indicates that, in agreement with the simulations, the system would preferentially be AFM, but for some distortions of the substrate lattice it is pushed to the FM transition. In summary the observations here reported show that strain is a suitable tool for electric control of the magnetic state in manganites. Compared to previous works, our experiment proves that by a fine tuning of the applied strain it is possible to set the LSMO film very close to a magnetic phase transition. This evidence was achieved by reducing the thickness of the film as compared to previous reports, thus inhibiting the relaxation of the structure and obtaining higher values of strain by epitaxy. The active control of strain (by electric fields or by temperature) allows not only to modulate the magnetic properties, but also to “switch” between two competing ground states. This result is highly suggestive for designing memory applications.

4. Electrical modification of morphology and its effects on ferromagnetism

This chapter presents the second case study on which this thesis is built upon, that is the Fe_xMn_{1-x}/PMN-PT heterostructure. The focus of the discussion will be on the newly-observed (and reversible) electrical control of morphology in PMN-PT crystals, and its effects on the magnetic properties of the metallic overlayer [79]. Following the structure adopted in the previous chapter, the properties of the materials studied are presented in section 4.1. Particular emphasis is given to PMN-PT and its ferroelectric domains, which have been thoroughly studied and are believed to be crucial for the description of magneto-electric coupling across the interface with the overlayer. In section 4.2 the literature on this and similar systems is summarized, which focuses on modelling strain-mediated coupling. Section 4.3 contains our novel experimental results that shine a light on the so far overlooked role of interface morphology. The results are discussed in section 4.4 and compared with the current interpretations.

4.1. Materials

Among the ferromagnetic materials, the simplest examples are some of the $3d$ transition metals: Fe, Co, Ni. It is no surprise that many studies in multiferroic heterostructures involved these elements or their alloys, since their magnetic properties are well understood and hence represent an important conceptual starting point. Moreover, they have high Curie temperatures and can already be deposited by techniques which are industry-friendly, such as sputtering. Hence, any functionality obtained in multiferroic heterostructures involving these metals is closer to real applications than other systems involving complex magnetic oxides. The drawback of course is that their ferromagnetic state is robust and difficult to perturb. Given the short charge screening length (few unit cells) there is very small chance to observe charge-mediated effects in films of a reasonable thickness (few nanometers). Exchange-mediated effects have been studied, but often imply the presence of a multiferroic material such as $BiFeO_3$ [25], so that this cases still fall under the framework of "complex oxides physics". Most of the work has focused on strain-mediated coupling. The magnitude of the effect depends on the magnetostriction constants of the materials λ (which depends on the crystallographic direction, λ_{100} and λ_{111}) [80]. In Ni for example, they are both negative and of similar magnitude, so that the behavior in single crystals and polycrystalline specimens is similar. In iron, they have opposite sign instead. For a polycrystalline film, the result is a small negative coefficient, but the presence of a texture can drastically change the behavior. In a hexagonal crystal such as Co, the effect is very strong in particular directions, but negligible along the c axis. The polycrystalline case falls between Fe and Ni. Finally, alloys such as CoFeB have been synthesized and studied because they are amorphous and magnetically soft, e.g. show a very narrow hysteresis loop and small coercive field, so that any electrically induced change in anisotropy could be easily detectable.

Regarding ferroelectric materials, and having in mind strain-mediated applications, the choice naturally falls on compounds that show the highest piezoelectric effect. These are perovskite ceramics like $PbZr_{1-x}Ti_xO_3$

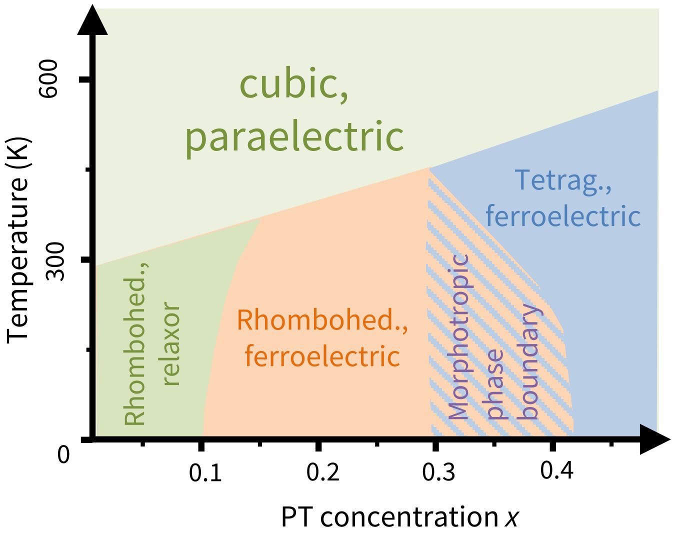

Figure 4.1: Schematic representation of the PMN-PT phase diagram.

(PZT) or $Pb(Mg_{0.35}Nb_{0.65})_{1-x}O_3-PbTi_xO_3$ (PMN-PT), also already in use at the industrial level. $PbMg_{0.35}Nb_{0.65}O_3$ (PMN) falls within the category of relaxor ferroelectrics [81]. It never presents a spontaneous polarization, but at a certain temperature it develops polar regions at the nanoscale that can be influenced by applied electric fields. These are at the origin of giant electrostriction and a high dielectric constant, which present a broad, frequency dependent maximum as a function of temperature. This maximum corresponds to the freezing of the polar nano-regions in a sort of glassy state. On the other hand, $PbTiO_3$ (PT) is a standard ferroelectric with tetragonal structure. The solid solution PMN-PT shows spontaneous ferroelectricity below a critical temperature, but shares many properties of the typical relaxor ferroelectrics, like intrinsic inhomogeneity, polar nano-regions above T_C, and anomalies in the temperature dependency of structural, thermal and dielectric properties. For low x, the structure is rhombohedral, while for $x \geq 0.4$ it is tetragonal [82] (see figure 4.1). These two regions of the phase diagram are separated by the so-called morphotropic phase boundary: a range of compositions and temperatures within which the best dielectric and piezoelectric properties are obtained. These effects are believed to originate from the coexistence of both the rhombohedral and tetragonal phase at the microscopic scale [83]. This may result, on the macroscopic scale, in a lower-symmetry monoclinic structure [84]. The details of the physics of relaxor ferroelectric, and in particular at the morphotropic phase boundary, are still object of study. The origin of the relaxor behavior is not well understood, and so is its relationship with structural and chemical disorder, and the dynamics of the polar nano-regions [81].

The main concern in the use of piezoelectricity to manipulate magnetism is that it is a volatile effect: when the electric field is removed, the resulting strain also vanishes. However, non-volatile effects have been observed in PMN-PT based heterostructures and have been understood in terms of non-reversible ferroelectric domain rotation. In the rhombohedral phase of PMN-PT, the polarization vector can be aligned along any of the $\langle 111 \rangle$ pseudo-cubic directions. Inverting the polarization between "up" and "down" (i.e. reversing the out-of-plane component) can produce 71° or 109° or 180° domain rotation, as shown in figure 4.2. In the 71° case the in-plane component is unchanged, and so is the strain transferred to an overlayer that could be grown on it. In the 180° case, all the components are reversed, so that the initial and final states are strain-symmetric. In the 109° case instead the in-plane component of polarization is rotated by 90°, causing a change in the applied strain accordingly. In this way out-of-plane poling a PMN-PT(001) crystal can induce a rotation of the magnetic easy axis through magnetostriction. Interesting effects can also be obtained for the PMN-PT(011) cut. In this case applying an out-of-plane electric field of the right magnitude can set a stable in-plane polarization [85]. As a consequence the in-plane strain can be reversibly controlled by out-of-plane poling, which is remarkable for strain-mediated magnetoelectric coupling. Also in this case, however, the desired functionality is contingent to specific domain rotation, which has to be 71° or 109°.

4.2. State of the art

The early trials of electrical control of magnetization through strain wanted to exploit piezoelectricity and magnetostriction. PMN-PT is an interesting candidate for its electro-mechanical properties, while highly

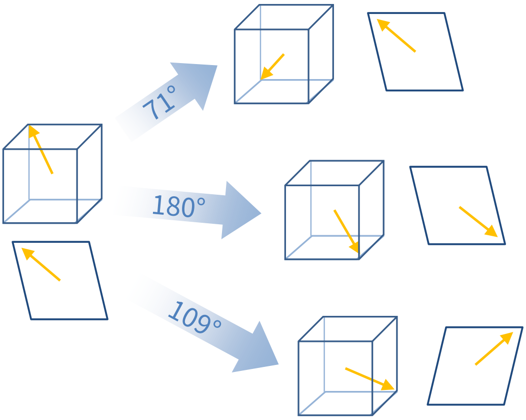

Figure 4.2: Rotation of the ferroelectric polarization in rhombohedric PMN-PT. Starting from an initial state, the out-of-plane component of polarization can be reversed in three different ways. The in-plane component can be invariant, be fully reversed or rotate by 90°, accordingly. 2D sketches represent the in-plane component of polarization in the various configurations.

magnetostrictive materials such as $CoFe_2O_4$ appeared to be promising [86]. However, as expected from symmetry considerations, when the electric field is removed the magnetization goes back in its initial state. The first report of non-volatile control of magnetization with electric field in this kind of heterostructure is the one of S. Zhang et al. in 2012 [87]. In their experiment, a 20 nm $Co_{40}Fe_{40}B_{20}$ thin film was deposited on PMN-PT(001). They observe a loop-like change in magnetization as a function of the out-of-plane electric field. While as-grown films are isotropic, after out-of-plane polarization a uniaxial magnetic anisotropy is induced by a preferential orientation of domains along a particular pseudo-cubic body diagonal. The hard/easy axes are indeed perpendicular, along $\langle 110 \rangle$ directions. Both Piezo Force Microscopy (PFM) and diffraction analysis show that “up” and “down” polarization states correspond to domain configurations which are non symmetric. A fraction of domains indeed rotate by 109°, resulting in a change in the applied strain and consequently a change in the magnetic anisotropy. Hence, these results can be successfully explained by strain-mediated magnetoelectric coupling, and the authors point at the absence of magnetocrystalline anisotropy in CoFeB as a key factor for observing this effect. A different approach is followed by Buzzi et al. (2013) [88], who deposited Ni nano-islands with an ellipse shape on PMN-PT(011). The magnetization of the islands is monitored by XMCD-PEEM as a function of the applied electric field. A variety of behaviors is observed: some dots exhibit a remanent 90° rotation of magnetization in correspondence of the coercive field of PMN-PT, some others rotate back to the original direction at high fields, and some of them are not affected at all. These observations have been explained again in terms of strain-induced effects. Different islands sit on different ferroelectric domains, which follow different switching paths and are hence subject to a different strain. Another Chinese group in 2015 report similar results for 30 nm Fe deposited on PMN-PT(011) [89]. Originally the authors interpreted the results in terms of charge-mediated or chemistry-mediated effects, although this hypothesis is not supported by any experimental evidence. What is undoubtedly observed is a change in the magnetic anisotropy vs. out-of-plane polarization. Similar to the work of 2012, the anisotropy is more or less pronounced, and the main change happens for two axis 90° apart. We can interpret this still as an effect of asymmetric strain state for up/down polarization. The angular dependence of magnetization is however more complicated with respect to the CoFeB case, because of the presence of magneto-crystalline anisotropy. Heidler et al. in 2016 studied Co/PMN-PT(011) heterostructures by XMCD [90]. Non-volatile changes in the remanent magnetization are observed. This is seen comparing in-plane and out-of-plane polarization, as expected from the strain-mediated picture, but also for opposite out-of-plane poling. Since this last effect is evident only in thinner samples (3.5 nm), it was attributed to a purely interfacial phenomenon. The author describe it as a charge-mediated magneto-electric coupling: charge accumulated at the interface can apparently change the magneto-elastic constant and hence the magnetic anisotropy. This is however quite surprising if we compare the thickness of the film with the typical screening length in metals, one order of magnitude smaller. In the same year, Li et al. present another experiment on CoFeB/PMN-PT(001) [91]. The novelty here is that they employ microscopy techniques such as scanning MOKE microscopy and SEM with polarization analysis (SEMPA) to locally observe the response of magnetization to electric field. In accordance with previous studies, there are regions showing a loop-like or butterfly-like behavior. The preferential orientation of magnetization again rotates by about 90° switching the polarization. In 2017, some of the authors of the first study here cited [87] propose again a similar experiment but with Fe instead of CoFeB

[92]. Qualitatively, the results are very similar. The main extension is the effort to separate volatile and non-volatile effects and the different contribution to anisotropy. Interestingly, the angular dependence of non-volatile changes closely resembles the observation of Zhang et al. (2015) [89]. In 2018, two interesting papers appeared addressing magneto-electric coupling using microscopy techniques. Lo Conte et al. [93] observed the domain configuration of micrometer-sized Ni squares deposited on PMN-PT(011) as a function of the applied field by XMCD-PEEM. The initial state of the Ni dots, a typical Landau flux-closure vortex, transforms in a two-domain configuration after application of an electric field. The switching field however varies from dot to dot. These results are complemented by Laue microdiffraction data, from which the authors quantify the local strain applied. This strain happens to be inhomogeneous on a micrometer scale, which matches with the dot spacing. Ba et al. [94] use MOKE and SEMPA to study 10 µm wide CoFeB discs deposited on PMN-PT(001). Three distinct behaviors are observed: 90° rotation of the easy axis, no rotation at all or 30-40° rotation. These where attributed to discs subject to 109° ferroelectric domain rotation, 71/180° rotation, or a multi-domain state respectively. Still in 2018, Liu et al. published for the first time the observation of electrically reversible cracks in PMN-PT(001) crystals [95]. They do not focus on magneto-electric coupling, but instead on the dramatic change in resistance observed in a MnPt metallic overlayer. Finally in 2019, Ghidini et al. [96] quantified more precisely the magnetization rotation in Ni/PMN-PT(011) heterostructures using XMCD-PEEM, noticing that it is actually smaller than 90°, contrary to the previous belief. This was discussed in terms of the shear strain which accompanies the ferroelectric domain switching process.

4.3. Results

The samples of our study are 4 nm thick Fe and $\mathrm{Fe}_x\mathrm{Mn}_{1-x}$ thin films deposited on $\mathrm{PMN}_{0.6}$-$\mathrm{PT}_{0.4}$(001) by Molecular Beam Epitaxy. Our choice of the FeMn alloy is based on the fact that the magnetic state can be tuned from ferromagnetic to antiferromagnetic by changing the Mn concentration. The idea was that magneto-electric coupling might produce stronger effects in materials that are set close to a magnetic transition. A noteworthy case is the one of FeRh, which displays an antiferro-/ferromagnetic transition when the temperature exceeds 473 K [97]. FeMn could in principle display a similar functionality at room temperature, provided that the right composition is selected. As we shall see however, pure Fe and FeMn samples show similar behavior, suggesting that the observed magnetoelectric coupling originates from a very general phenomenon. The deposition of the films was carried out at room temperature, without any surface preparation of the substrate. The composition of the FeMn alloys was tuned by adjusting the deposition rate from the two evaporator sources of elemental Fe and Mn, calibrated with a quartz microbalance. The results here presented are relative to samples with Fe concentration $x \geq 0.85$, which are ferromagnetic, as well as pure Fe films with the thickness of 4 nm. The samples were capped by a 3 nm thick MgO film, evaporated from a single crystal by electron bombardment, after MBE growth, in the same UHV system. Given the deposition conditions, no epitaxial relation between the substrate and the overgrown film is expected. Indeed no LEED pattern was observed from the surface of the samples after FeMn deposition. No diffraction peaks were observed in $\theta - 2\theta$ scans either, as measured *ex-situ* in a X-ray diffractometer. Hence the films should be polycrystalline with small grains. In the sample for micro-MOKE characterization, an interlayer of SiO_2 (10 nm) was deposited between the substrate and the Fe film to remove any substrate-induced texture in the ferromagnetic layer. The deposition was carried out by magnetron sputtering at room temperature, from an RF source with a mounted SiO_2 target, at $5 \cdot 10^{-3}$ mbar Ar atmosphere and 10^{-6} mbar base pressure. A rotating sample holder has been used to obtain a uniform deposition. A constant deposition rate of 0.3 Å s^{-1} was reached at an RF power of 90 W. The film thickness was calibrated on a test sample by means of an *ex-situ* profilometer. In this case the sample was finally capped by a 3 nm Au film, also deposited by MBE right after Fe deposition.

4.3.1. *In-operando* XMCD

XAS and XMCD measurements were performed at the APE-HE beamline in TEY detection mode, as described in section 3.3. Samples were attached to a specific sample holder with two separate electrical contacts in order to apply the switching electric field to obtain the out-of-plane polarization of PMN-PT in situ (see figure in chapter 2). The back of the sample, glued to the holder by silver paint, serves as bottom electrode. The

FeMn film act as top electrode, and was connected to the other electrical contact with a thin gold wire. As for BTO, current-voltage characteristics show well pronounced peaks in correspondence of polarization switching of about ±100 V (corresponding to a field of $0.50\,\mathrm{kV\,cm^{-1}}$). After setting the polarization up (down), no peak in the current is observed for a positive (negative) voltage sweep, testifying the ferroelectric behavior of PMN-PT. This behavior is shown in figure 4.3.

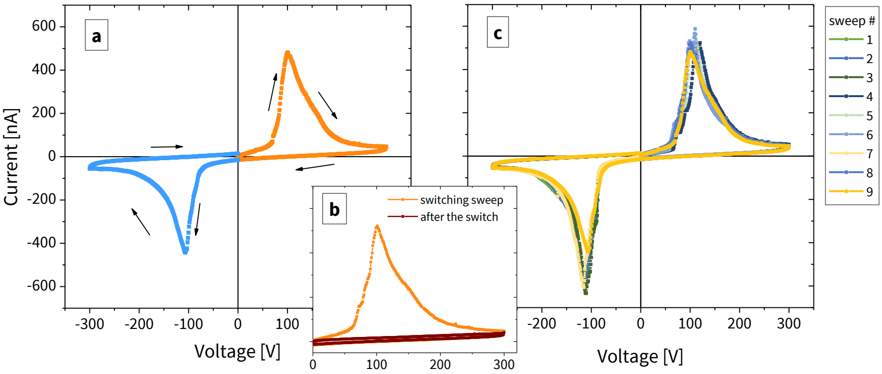

Figure 4.3: **a** - two terminal current vs. voltage curves measured across the thickness of PMN-PT. Peaks in the current testify the switching of out-of-plane polarization. **b** - repeating the same half cycle twice no peak is observed, proving that the electric polarization is remanent. **c** - the switching field is highly reproducible

XMCD spectra at the Fe X-ray absorption L edge were collected right after setting the out-of-plane polarization, to compare the results for up/down cases. The same measure was repeated at several positions of the sample surface, with variable results. Some noteworthy results are shown in figure 4.4 for FeMn (11% Mn) and pure Fe samples. Reversing the out of plane polarization can induce a drastic change in the intensity of the measured XMCD signal. However, depending on the sample area probed, the signal can be higher or lower for the P_{up} or P_{down} state, i.e. the effect of the magneto-electric coupling may be opposite. In the same figure (panels **c**, **d**, **g**, **h**) are presented element-sensitive hysteresis loop measured by XMCD at the Fe L_3 edge, corresponding to the spectra shown in panels **a**, **b**, **e**, **f**. These show that the change of the XMCD signal, measured at remanence, corresponds to a change in the shape of the whole hysteresis loop. This is compatible with a change in the magnetic anisotropy of the sample. It is important to stress that what shown in figure 4.4 are the most dramatic results: in some of the investigated areas no sizable change between P_{up} and P_{down} was observed. The X-ray beam footprint on the sample is about $150 \times 150\ \mu m^2$, hence local effects are present on a spatial scale of this magnitude.

The reproducibility of the observed effect was tested by collecting XMCD spectra after switching the electric polarization up and down several times. One example is given in figure 4.5 for a given position of the Fe sample. Within the accuracy of the measurements, polarization switching seems to induce two distinct and reproducible magnetic responses. This is in accordance with the reversibility of the electrically-induced morphological change, as will be discussed in the next section.

4.3.2. Topographic characterization

From the results presented in the previous section, it is clear that a probe with spatial resolution is needed. We resorted to Atomic Force Microscopy (AFM) to analyze the effect of electrical polarization on the topography of the samples. AFM measurements were acquired with a A100 microscope of A.P.E. Research. Cantilevers with stiffness of 40 N m and length of 125 µm were used. The sample was measured at ambient pressure at zero voltage, after cycling the electric field to positive or negative saturation using the sample holder connections in the measurement position. The tip was lifted during the application of the bias to avoid tip collisions during the morphological transitions.

Something very interesting can be already be observed with the ancillary optical microscope of the instrument, as shown in figure 4.6, panels **a** and **b**: when the electrical polarization is switched “up”, the morphology becomes more corrugated and several cracks appear on the surface in a disordered pattern. Surprisingly, when the polarization is switched “down”, the surface smooths out and the cracks disappear. Repeating the electrical sweep several times, it is seen that cracks open deterministically always in the same place, and close again without any sign of fatigue. AFM data are reported in figure 4.6, panels **c** and **d**. A rich surface topography is observed, with island-like areas of different lateral size (ranging from tens of µm to fractions of µm) and a root-mean-square roughness of 4.5 ± 0.5 nm. The same features were also measured on pristine PMN-PT substrates, indicating that such morphology is not caused by a inhomogeneous depo-

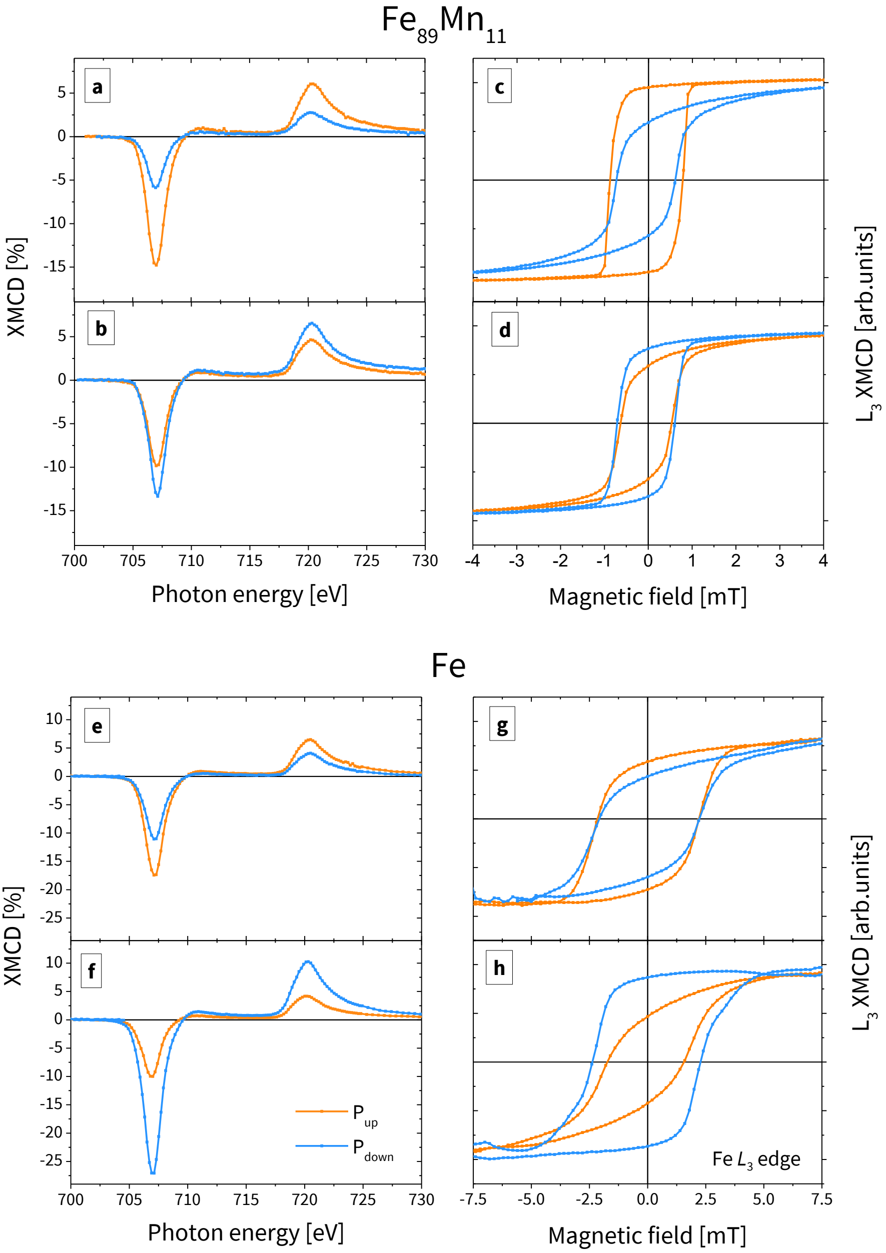

Figure 4.4: **a**, **b** - Fe $L_{2,3}$ XMCD spectra collected in two different points of a FeMn sample, for ferroelectric polarization of the substrate pointing up (orange) or down (light blue). **c**, **d** - corresponding Fe L_3 hysteresis loops. **e** **. . . h** - analogous measurements for a Fe sample.

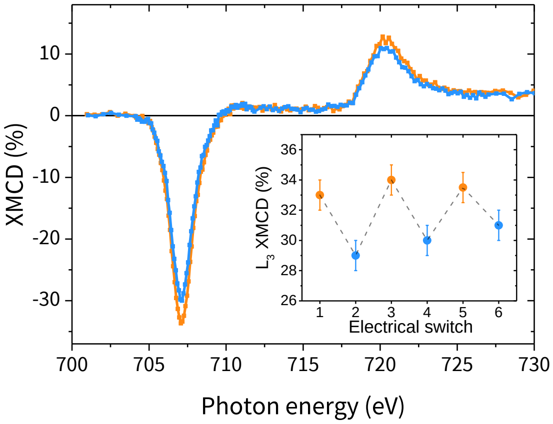

Figure 4.5: Reproducibility of the XMCD measurements. In a selected point of the Fe sample, $\vec{P}$ was reversed up and down three times to observe the evolution of the magnetic signal. As summarized in the inset, the results are perfectly reproducible within the accuracy of the measurement.

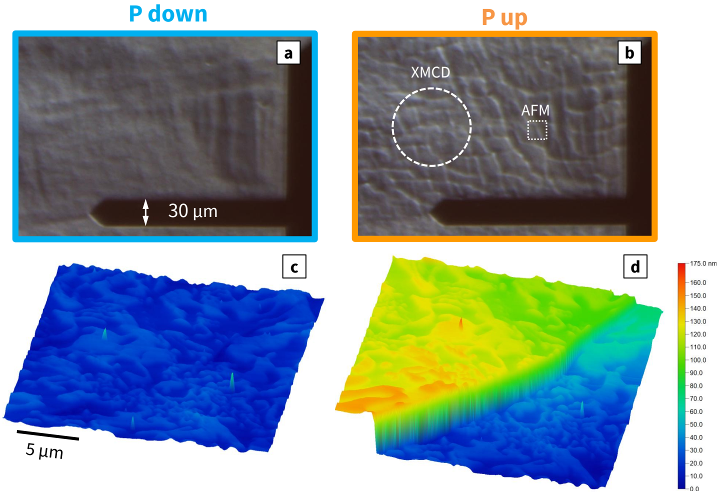

Figure 4.6: **a**, **b** - images acquired by optical microscopy for opposite out-of-plane electrical polarization. The dimension of the AFM images and the X-ray spot used for XMCD are reported for comparison. **c**, **d** - corresponding AFM topography collected on a 20 × 20 µm area.

sition of the FeMn layer, but is instead a characteristic of the substrate which is transferred to the magnetic thin film on top. Besides that, for the P_{up} case surface cracking induce the appearance of a step whose height is about 100 nm, much bigger than the surface roughness and the thickness of the film. Similar steps where observed in other areas of the sample, with variable height of tens of nanometers. Hence in the P_{up} case the FeMn film is mechanically broken in many points. Surprisingly, AFM hardly detects any trace of the cracks in the P_{down} case (notice that the image in figure 4.6 - **a** has been obtained after several cycles of positive and negative sweep). This is very similar to what observed recently by Liu et al. [95], where the reproducibility of this behavior was tested over millions of cycles. Even more surprisingly, they found that the crack opening does not alter irreversibly the conductivity of the metallic thin film (35 nm) on top of PMN-PT, but instead after negative polarization the previous resistance is recovered. One can expect to see similar reversible effects in the magnetic properties, as indeed the XMCD data previously presented show. Effective contact or percolation among the cracked areas, is therefore re-established after a full cycle of external electric polarization.

4.3.3. MOKE microscopy

MOKE microscopy allows combining magnetic characterization at the local scale with the observation of the electrically-induced changes in morphology, and is therefore an excellent tool to study the interplay between these two aspects. Imaging-magnetometry measurements were done at the PoliFab laboratory of Politecnico di Milano using an optical wide-field polarization microscope (Zeiss Axiotron II) customized in-house for Kerr microscopy. All the measurements were performed in air and at room temperature. The magnetic field was applied in the sample plane by means of a calibrated electromagnet. Images are acquired by a high-resolution, high-sensitivity, and low noise digital CMOS camera by Hamamatsu (ORCA-spark C11440-36U). The magnetic hysteresis loops are obtained by selecting an arbitrary region of interest and thus integrating the intensity collected by the corresponding pixels using the camera as a conventional photodetector. The signal for each pixel is proportional to the magnetization along the sensitivity direction, which is parallel to the externally applied magnetic field in these measurements. The electrical polarization of the substrate can be switched without removing the sample from the microscope, thanks to a specific mounting. With the

100× objective, each pixel corresponds to an area of 85×85 nm^2 of the sample surface. The real spatial resolution is however determined by the diffraction limit of visible light, which is estimated to be about 0.5 µm by the Rayleigh criterion. For this experiment, a sample was prepared with 10 nm of amorphous silica between the substrate and the Fe film. Its presence rules out any contribution of ion migration from the substrate or charge-driven phenomena, and furthermore removes any texture in the Fe film that may be induced by the substrate crystal symmetry. Given the magnitude of the electrically induced fractures, however, it should not affect any morphology-driven phenomena.

By optical microscopy, the electrically induced fracturing can be easily observed. In general cracks are denser in certain parts of the sample surface, and form a complex and disordered pattern (see figure 4.7). However, to characterize the relation between magnetic anisotropy and morphology, MOKE measurements were collected in areas in which the cracks form a somewhat ordinate pattern, with the rifts running parallel. The two areas selected differ because of the direction of the rifts, from now on defined "vertical" and "horizontal" for short as referred to the sample image plane. Hysteresis loops where acquired in two cases, rotating the sample by 90° respect to the magnetic field, which happens to be either approximately parallel or perpendicular to the fracture lines. For both orientations, the magnetic field was parallel to one of the $\langle 100 \rangle$ directions of the substrate.

A first analysis was performed by integrating the signal on a big region of interest, containing 3 or 4 cracks. First of all, it must be stated that the sample has a macroscopic magnetic anisotropy. Indeed for both the areas analyzed, and independent of the polarization state, the hysteresis loop is more squared for the applied field H in a particular direction, from here on arbitrary denoted as 0°. This is shown in figure 4.8. Secondly, reversing the electric polarization changes the shape of the hysteresis loop, affecting both remanence and coercive field. For fixed direction of $\vec{H}$ (e.g. 0°) the change is opposite in the two regions, as can be seen in figure 4.9. In one region the $\mathrm{P_{up}}$ case shows a more easy-axis-like hysteresis loop than the $\mathrm{P_{down}}$ case, while in the other region is the opposite. This is very similar to the XMCD measurements of figure 4.4, which were "blind" with respect to morphology. Micro-MOKE data show that the key parameter to understand this phenomenon is the relative orientation of the cracks with respect to $\vec{H}$. As a third point, the observed magneto-electric effect can be described effectively as a change in magnetic anisotropy. Indeed, once fixed a single region, $\mathrm{P_{up}}$ makes the loop more easy-axis-like for

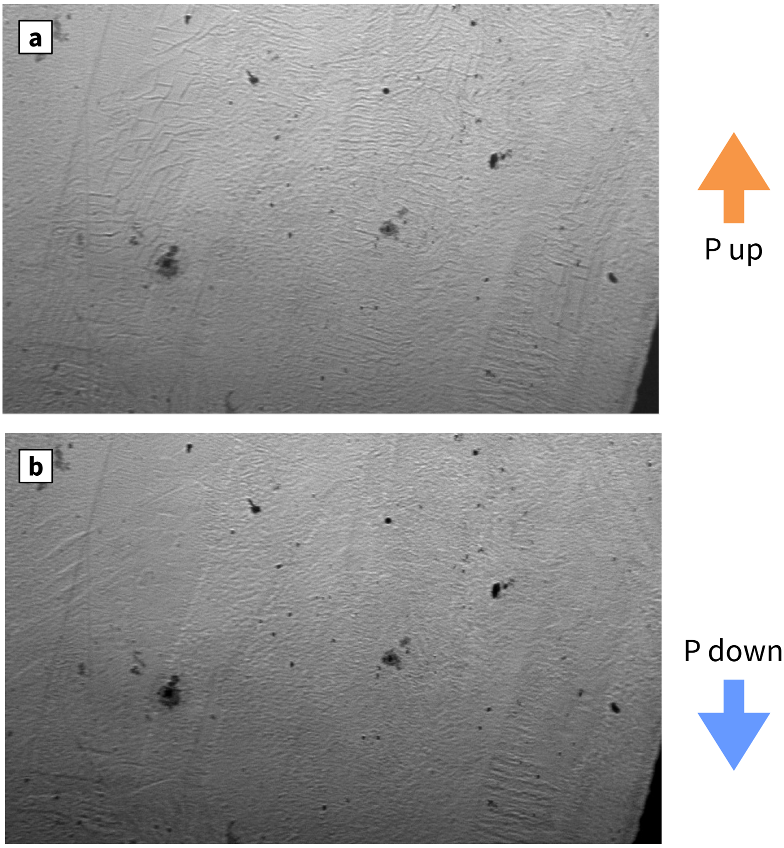

Figure 4.7: **a** - optical microscope image of the surface of a Au/Fe/SiO$_2$/PMN-PT(001) sample in the P_{up} state. Cracking of the surface is visible in different parts of the sample, with various arrangements of the rift pattern. **b** - same region imaged in the P_{down} state.

H in a certain direction, and more hard-axis-like for the perpendicular direction. The overall effect is that in one region the magnetic behavior is more anisotropic in the P_{up} state than in the P_{down}, while the opposite is observed in the other region. This can be seen from figure 4.8.

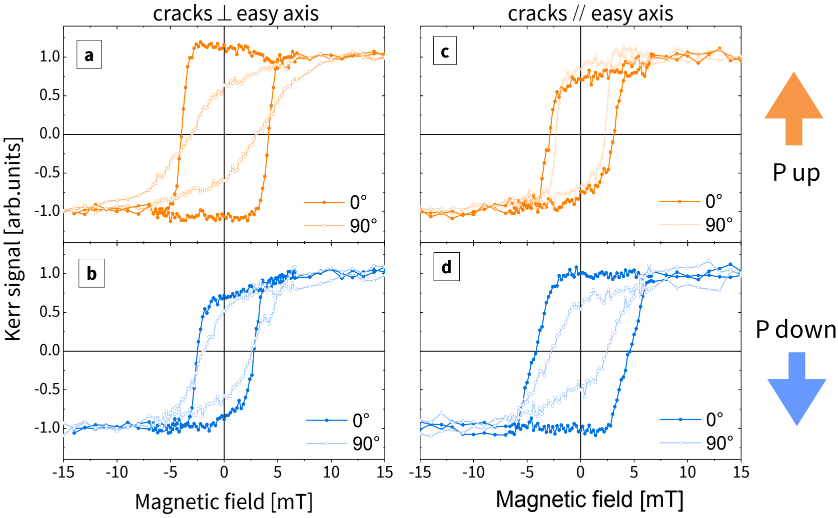

Figure 4.8: **a** - hysteresis loops acquired for polarization up in a region with cracks parallel to the easy axis. **b** - same for polarization down. **c**, **d** - analogous measurements in a region in which the cracks are almost perpendicular to the first one. Different directions of the magnetic field (0° or 90°) correspond to bold or light colors, respectively. On average it is evident that 0° correspond to an easy axis compared to 90°. The regions are the same imaged in figure 4.9.

In a second analysis, we integrated separately the intensity coming from regions of the surface separated by cracks, which have a striped shape in the areas selected. The aim is to understand if the fracturing of the surface induces different magnetic anisotropy between the two sides of the rift. The results are presented in figure 4.10. It can be seen that the different "stripes" present hysteresis loops that are not identical, however the effect of the electric polarization is uniform. Thus the magneto electric coupling acts in the same way in regions separated by a crack, which coherently contribute to the overall behavior described in the previous paragraph.

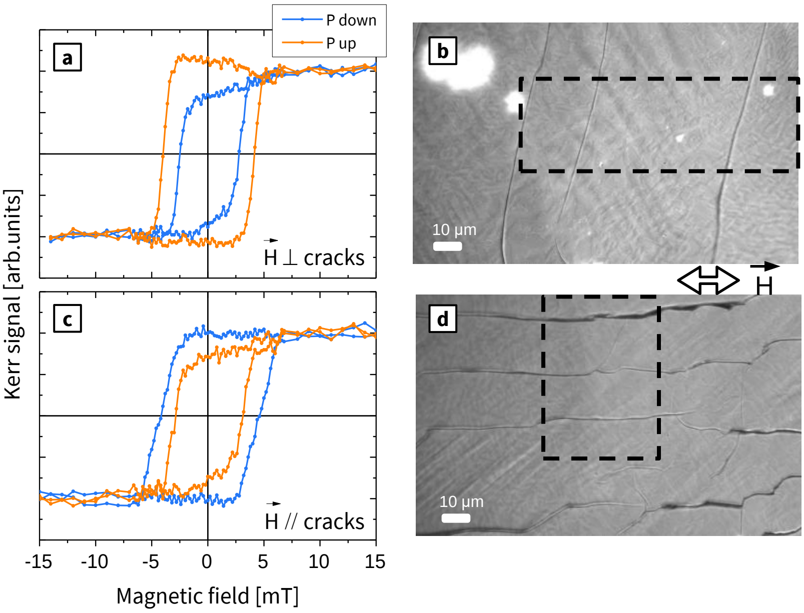

Figure 4.9: **a**, **c** - hysteresis loops acquired for opposite substrate polarization integrating the intensity if the dashed region shown in **b** and **d**, respectively. Comparing panels **a** and **c**, it is evident that the effect of the out of plane polarization is opposite in the two regions.

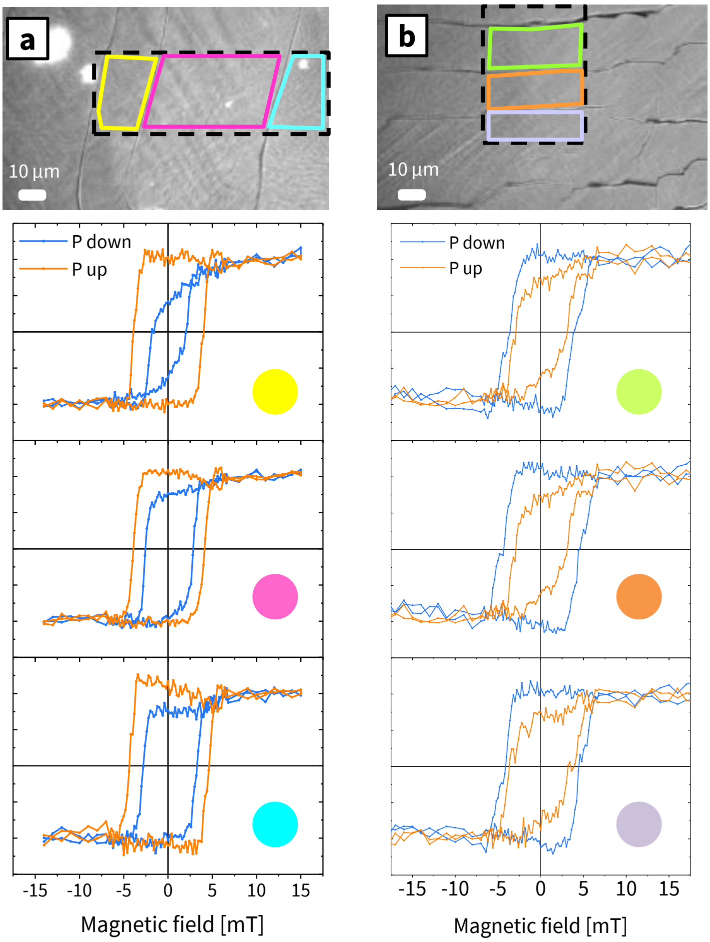

Figure 4.10: stripe-by-stripe analysis of the magnetic behavior for the two regions with **a** - vertical and **b** - horizontal cracks. The big regions of interest (black dashed contours) where divided in sub-regions (coloured contours) and the intensity was integrated over each of them to obtain the hysteresis loops. The different stripes among the same area show a similar response to out-of-plane polarization.

4.3.4. PEEM data

The same samples studied by XMCD at the APE-HE beamline in Elettra (results of section 4.3.1) were also studied with PEEM at the I06 beamline of the Diamond Light Source. Secondary electron emission from the sample surface was imaged with a Elmitec SPELEEM-III microscope. The X-ray beam comes to the sample surface with a grazing angle of 16°. XMCD asymmetry maps are obtained according to the formula:

$$\mathrm{XMCD} = \frac{I^R - I^L}{I^R + I^L}, \quad \text{where } I^\gamma = \frac{I_{\mathrm{res}} - I_{\mathrm{off}}}{I_{\mathrm{off}}}$$

Here I_{res} and I_{off} indicate intensities acquired with photon energy resonant to the Fe L_3 edge and off-resonance, respectively. $\gamma = R, L$ indicates right and left circularly polarized light. Repeating this procedure for two orthogonal sample orientations allows reconstructing a 2D vector map of the magnetization. A proper dedicated sample holder allows for application of a voltage across the sample thickness *in-situ*. Magnetization vector maps were measured after switching the polarization up or down, with zero applied electric field. A 50 µm field of view was used. Samples were demagnetized *ex-situ* by an oscillating field produced by a solenoid. No magnetic field was ever applied during the PEEM experiment. This experiment shows a direct evidence of magnetization rotation using exclusively an electric field, which is a key aim in multiferroic heterostructure. The preferential orientation of the magnetic domains, observed in the domain arrangement, is drastically different when the polarization is reversed. Different behaviors have been observed, which vary in the details. In the following some illustrative cases are presented.

Let's discuss figure 4.11 for the Fe/PMN-PT sample. In panel **a** the raw image is presented, from which it is visible a fracture in the film in the top-left corner. At the beginning of the experiment, the sample is in the $\mathrm{P_{down}}$ state, and has been demagnetized. Panel **b** shows the corresponding vector map. The magnetization is mainly pointing upward, with some small elongated domains pointing in the opposite direction. Hence there is a clear preferential alignment of $\vec{M}$ along the vertical axis. After switching the polarization up (panel **c**) in a large portion of the image the magnetization vector points towards left, being subject of a rotation of about 90°. This happen on both sides of the rift, in accordance with the micro-MOKE data (however, along the fracture the magnetization appears disordered, maybe as an effect of dipolar interactions across the rift). When the polarization is switched down again (panel **d**) the system goes back to an assembly of domains pointing either up or down. The crack, now closed, coincides with a 180° domain wall. These data show that reversing the out of plane polarization induces a rotation of the magnetization of about 90°, which is compatible with the change in magnetic anisotropy deduced from XMCD and MOKE measurements. Figure 4.12 shows similar data for another region of the same sample, where no cracks are clearly visible. In this case the initial state presents a complex arrangement of magnetic domains, without an apparent preferential orientation. However, in the P_{up} state the magnetization is almost uniformly oriented in the vertical direction. Switching back to P_{down} the domain arrangement is more disordered, with appearance of domains pointing either left or right. Even in this case what is observed is a change in the preferential orientation of the domains for different electrical poling. The preferential orientation for P_{up} is orthogonal to the one observed in the previous image, testifying that the magnetoelectric coupling acts locally on a microscopic scale. Figure 4.13 shows vector maps for the FeMn sample. Here a crack crosses the whole field of view, as can be seen from panel **a**. The ferroelectric polarization was toggled between up and down 3 times each, and vector maps were recorded at each stage. It is evident that the P_{down} case favors alignment

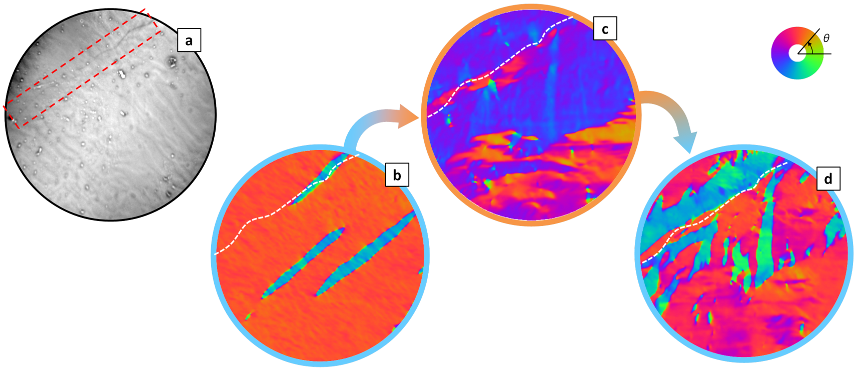

Figure 4.11: a - PEEM image acquired at the Fe L_3 edge for a Fe sample. A surface crack is highlighted by the dashed box. **b** - magnetization vector maps for polarization down (at the beginning of the experiment). **c** - after *in-situ* switching the polarization up. **d** - after switching it back down. The position of the crack is marked by a dashed white line in the magnetization vector maps. The direction of magnetization is encoded in different colors, according to the colorwheel.

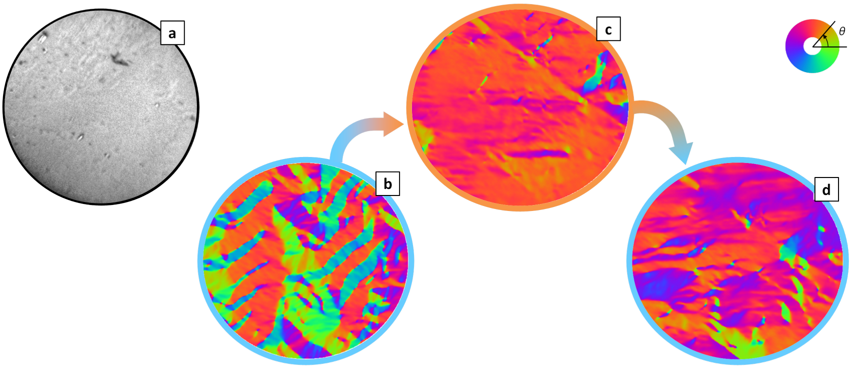

Figure 4.12: Data analogous to those of figure 4.11, for the same sample but for a different region, with no cracks visible. The vector maps here presented where acquired in parallel to those shown in 4.11.

of magnetization along the horizontal axis. The magnetization is almost uniformly pointing right, except some small domains in proximity of the crack. In the P_{up} case instead we systematically observe some big domains pointing either (approximately) up or down. Comparing panels **d** and **f**, there is also some similarity in the position of these domains. Once again this is consistent with a reversible electrically-induced 90° rotation of the easy axis. Contrary to figure 4.11, the crack in this case coincides with a 90° domain wall, and the two sides of the crack seem to display different preferential orientations of the domains.

4.4. Discussion

Let's now discuss the observed phenomena in terms of the magneto-electric coupling mechanisms described in chapter 1: ion migration, exchange mediated, charge mediated, strain mediated. The first three can be easily ruled out. The last one will be discussed in more detail. First of all, it is possible to compare the XAS spectra obtained for opposite electrical polarization to detect any electrically-driven change in the chemical environment of iron. The lineshape of the Fe L edges (shown in figure 4.14 - **a**) corresponds to non-oxidized metallic iron for both P_{up} and P_{down}, so that ion migration can be ruled out. Exchange-mediated coupling can

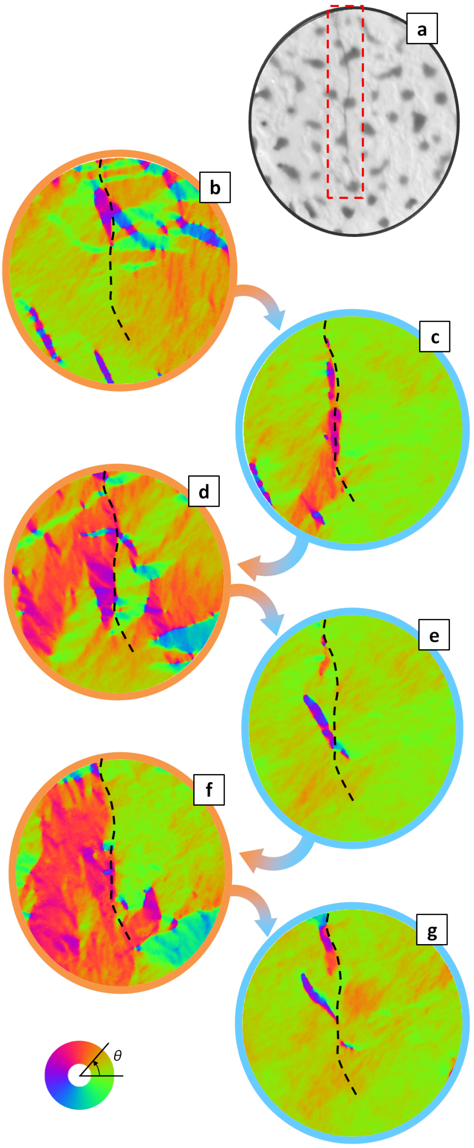

Figure 4.13: a - PEEM image acquired at the Fe L_3 edge for a FeMn sample. A surface crack is highlighted by the dashed box. Black silhouettes are impurities on the surface. **b . . . g** - magnetization vector maps for consecutive switches of the polarization between up (b, d, f) and down (c, e, g).

be excluded a priori, since there is no other magnetic material involved than iron. Some iron oxides can also be antiferromagnetic (e.g. hematite $\alpha - Fe_2O_3$ [98]) but the presence of oxides should be easily detected by XAS, and again this is not the case. Charge-mediated coupling is also not a satisfying explanation. First of all, we would expect that a 10 nm thick SiO_2 interlayer would efficiently screen electrostatic interactions between the substrate and the iron film. If the observed magnetoelectric coupling was charge-mediated, in the micro-MOKE experiment we would expect to observe a highly reduced effect, if any. Instead, the observations are very similar to those of the XMCD experiment, which did not include the SiO_2 interlayer. Another relevant remark is that from zone to zone we observed effects with opposite trend. We may expect non-uniform charge accumulation at the interface, or eventually that some pinned ferroelectric domains would not switch. This would produce a non-uniform magnetoelectric response, with some areas more or less affected by electrical poling. However, this cannot explain the fact that in some areas positive poling induces an increase in the magnetic remanence while in some others induces a reduction. For this reason charge-mediated effects can be excluded.

4.4.1. The role of strain

The discussion of strain-mediated coupling is more intricate. Most of the literature regarding ferromagnet/PMN-PT(001) heterostructures indeed has been satisfactorily interpreted with this mechanism. The key to observe non-volatile effects is the 109° ferroelectric domain rotation in rhombohedral PMN-PT. In the case presented here, the concentration of 40% PT corresponds to a tetragonal phase, so that the usual model does not apply: switching the out-of-plane polarization can happen only by 180° rotation and is not expected to induce any change in the in-plane strain. Diffraction data, shown in figure 4.14a, confirm this on the macroscopic scale. In the pristine state two peaks are visible, corresponding to the in-plane and out-of-plane orientation of the tetragonal unit cell. After out-of-plane polarization, the in-plane peak is no more distinguishable, but no differences are detected between P_{up} and P_{down}. However, from the data nothing can be said about the strain at the microscopic scale. For sure the cracking of PMN-PT must originate from internal stresses that develop as a consequence of the electrical polarization, and these stresses must be local and non-uniform to generate such a disordered pattern of rifts. If the in-plane strain transmitted to the film differs for opposite po-

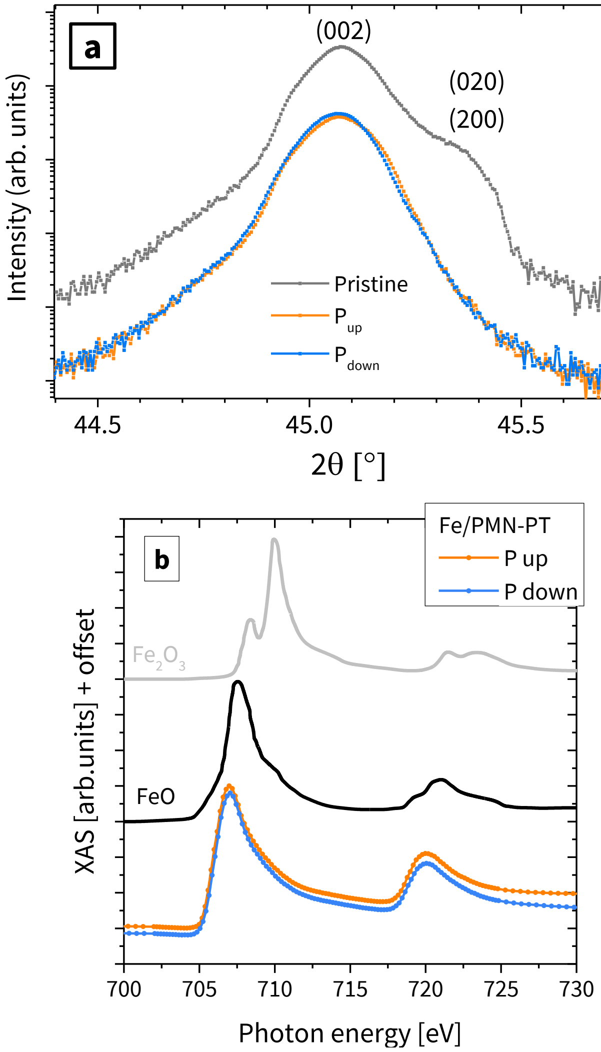

Figure 4.14: **a** - XRD $\theta - 2\theta$ scan of the PMN-PT substrate, for pristine and out-of-plane polarized case. **b** - isotopic XAS spectra of iron $L_{2,3}$ edges for opposite polarizations of the PMN-PT substrate. The two curves have been slightly offset for clarity. By comparison, XAS spectra for FeO and Fe_2O_3 are reported from the literature [99].

larizations, this may explain the observed change in magnetic anisotropy. Still, in a tetragonal crystal there is no reason to think that switching the out-of-plane polarization could induce a change in the in-plane strain. In rhombohedral PMN-PT instead, the modulation should be along the $\langle 110 \rangle$ directions. No change in anisotropy would be expected along $\langle 100 \rangle$ directions, corresponding to the measured loops at $\theta = 0°$ and 90°. Liu et al. [95] hypothesize that cracks develop in correspondence of ferroelectric domain walls between a pinned domain and a switchable one. The shear strain generated during the switch results in the fracture. If this is true, then regions of the Fe film separated by a rift should be subject to different in-plane strain. However micro-MOKE data show that striped blocks belonging to the same region behave magnetically in the same way. This is in discordance with a strain-mediated interpretation and promotes the hypothesis of a "morphology-driven effect" that changes the anisotropy on a mesoscopic scale, according to the rift pattern.

4.4.2. Phenomenological model

The micro-MOKE data show a strong connection between the change in anisotropy and the morphological modification when the cracks display some kind of orientation. These unprecedented observations suggest that magneto-electric coupling in this system may originate from a novel mechanism, never considered previously. It is important to notice, however, that the effect of morphology cannot be described as simple shape anisotropy. Indeed when the surface is cracked the hysteresis loop becomes more easy-axis-like when the field is perpendicular to the rifts. Cracking of the ferromagnetic film breaks chemical bonds between atoms, annihilating the exchange interaction between them. Furthermore, terraces separated by rifts are subject to dipolar interactions, according to the geometric arrangement: the inhomogeneity of magnetization in proximity of the cracks (observed by PEEM) may indeed be its symptom. In some cases, regions separated by cracks may have a lateral distance similar to the dimension of magnetic domains (up to 20 µm, again according to PEEM images). These ingredients can explain why such a morphological change can perturb the magnetic properties, but for a detailed description of this mechanism further studies are needed. A phenomenological model is here presented as a first attempt. Let $E_{\mathrm{anis}}(\theta)$ be the magnetic anisotropy of the system as a function of the in-plane direction of magnetization θ, with the following expression:

$$E_{\mathrm{anis}}(\theta) = K_{\mathrm{i}} \sin^2 \theta - K_{\mathrm{m}} \sin^2(\theta - \alpha)$$

The first term with $K_{\mathrm{i}} > 0$ describes the observed "intrinsic" uniaxial anisotropy, whose origin may be due to the growth conditions of the thin film. The second term describes the effect of polarization. Let's suppose $K_{\mathrm{m}} = 0$ in the $\mathrm{P_{down}}$ case, in absence of cracks, and $K_{\mathrm{m}} > 0$ in the $\mathrm{P_{up}}$ case. Let α be an angle describing the direction of the rifts in a situation where they are running parallel. The effect of magneto-crystalline anisotropy is here neglected, since we have no evidence for a long range structural order in the Fe film. The two regions investigated by micro-MOKE correspond to the cases $\alpha = 0°$ and $\alpha = 90°$. Also the magnetic field was applied either parallel or perpendicular to the easy axis, which means $\theta = 0°$ and $\theta = 90°$ respectively. A measure of the magnetic anisotropy of the system is given by $E(0°) - E(90°)$. The equation here proposed correctly describes the micro-MOKE data in the sense that for $\alpha = 0°$ the system it is more isotropic for $\mathrm{P_{up}}$ than for $\mathrm{P_{down}}$, while for $\alpha = 90°$ the system is less isotropic for $\mathrm{P_{up}}$ than for $\mathrm{P_{down}}$, as can be seen from figure 4.8. Basically this model simply includes a uniaxial anisotropy term which is polarization-dependent. It can equivalently describe the effect of strain, if the proper expression for K_{m} is used, with α indicating the direction of the expansion/contraction.

4.4.3. Conclusions, open questions and outlooks

The results presented in the previous section show a strong magneto-electric response in ferromagnetic metal / PMN-PT(001) heterostructures. This has the effect of changing the remanent magnetization (as probed by XMCD) and non-volatile rotation magnetic domains by means of an applied voltage (shown by PEEM). The electrical and reversible control of morphology in PMN-PT is a novel and surprising observation, and an unambiguous correlation between the morphological change of the heterostructure and its magnetic anisotropy is shown by MOKE microscopy. These findings add a new player in the magnetoelectric coupling of artificial heterostructures: despite the amount of work on ferromagnet/PMN-PT systems, the effect of morphology has never been considered. The work here presented shows that the presence of this effect however isn't just a detail, but its magnitude can, in some conditions, overpass the one attributed to the canonical mechanisms. This suggests new approaches to magneto-electric coupling in heterostructures, and may require some revision of the past literature regarding ferromagnet/PMN-PT systems. Unfortunately, the role of strain cannot be unambiguously distinguished in the data here reported. Regarding magneto-electric coupling, the main question is the following: does the change in magnetic anisotropy come from a strain-driven effect, being the cracking just a secondary symptom of the stresses produced or, on the contrary, strain generates cracking but it is the magnetic anisotropy that is modified *because of the consequent change in the morphology itself*? In the latter case we can talk about a novel mechanism, which can be termed "morphology-driven magneto electric coupling". In the former case, the results here presented shine some light on unprecedented consequences of strain in multiferroic heterostructures. Another open question is: why does PMN-PT break in the first place? Understanding how to obtain such surprising mechanical properties would pave the way to a new paradigm in micro-mechanics with piezoelectrics and ferroelectrics. The reproducible pattern of cracks may indicate that local fracture lines do exist among the grains of the PMN-PT substrate and that, when applying an external macroscopic electric field the local electric field at the crack boundaries can reach large values that create forces among the neighbouring grains such to induce shear displacements. One could conjecture that if the grain pattern was intentionally induced by nanolithography the observed phenomena could be engineered.

Not only the morphological changes of PMN-PT are reversible, the properties of the metallic layer on top show a certain reversibility as well. This is even more surprising if we think that the film breaks along its entire thickness during the crack formation. It is possible to envision novel devices exploiting such ductility, both based on electric transport [95] or magnetism. The challenge is to achieve control on the cracking geometry. One possible realization is also the following [100]: let's imagine patterning some metallic electrodes on a suitable substrate, and deposit successively a piezoelectric/ferromagnetic metal heterostructure. Applying a voltage difference between the top metallic layer and the bottom electrodes may induce deformation of the piezoelectric film according to the pattern of the electrodes. With a suitable choice of dimensions and voltages, a reversible breaking of the ferromagnetic film might be obtained, with consequent modulation of magnetic anisotropy. This concept is illustrated in figure 4.15.

As an example, let's consider ZnO as a piezoelectric material, which has a piezoelectric coefficient along the c-axis $d_{33} = 5.9\,\mathrm{pm\,V^{-1}}$ (about 1% expansion). This means that a 300 nm thick film would expand by 3 nm

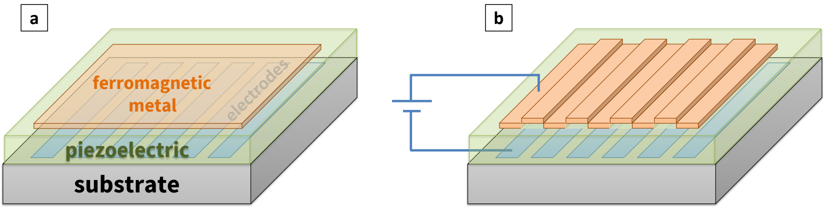

Figure 4.15: Schematic of a device based on the electrical control of morphology. An applied voltage between the patterned electrode array and the top contact causes elongation of the piezoelectric material only in specific regions. The morphology of the ferromagnetic layer changes and consequently also does its magnetic anisotropy.

in the vertical direction with application of 1 V. Therefore if the pattern of the electrodes is successfully imaged in the deformation of the piezoelectric layer, with few volts it would be possible to break an overlaying ferromagnetic film with a thickness of few nm. The lateral dimensions of the electrodes must be bigger than the ZnO thickness, otherwise the deformation pattern induced will not have sharp edges. As a ferromagnetic metal, let's consider a low-coercivity material such as amorphous CoFeB. If we imagine transferring a striped pattern with dimensions $0.5 \times 500\ \mu m^2$, the shape anisotropy would generate a demagnetizing field of 10 mT along the short dimension, enough to change the magnetic anisotropy of the film. Therefore, as a proof-of-concept experiment, we propose a ZnO(300 nm)/CoFeB(4 nm) structure with a striped electrode pattern with lateral size of 500 nm and similar spacing between them.

5. Summary and conclusions

Objectives

I explored the properties of systems that were fabricated aiming to exploit enhanced multiferroic behavior and potentially useful functionalities at room temperature. The systems of choice for this thesis were two prototypical multiferroic heterostructures composed by a ferromagnetic thin film deposited on a ferroelectric substrate: LSMO/BTO(001) and Fe,FeMn/PMN-PT(001). I focused on the magnetic response of the thin films to applied electric fields oriented perpendicular to the interface, and influencing the substrate. In both the chosen heterostructures the magnetic layers and ferroelectric substrates are all materials with high ordering temperature.

Methods used

The magnetoelectric coupling was investigated by measuring the magneto-optic effects (both in the visible by MOKE experiments *ex-situ*, in air, and by magnetic dichroism in X-ray resonant absorption, *in-situ*); all measurements were done *in-operando* mode, that means while applying variable electric fields and varying the temperature. This approach is powerful for discerning the effect of the applied electric fields from any others that may lead to ambiguities when comparing different experiments, different samples, or different *ex-situ* preparations. By comparing the measurements at reversed $\vec{E}$-field, i.e. for opposite out of plane polarizations of the substrate, it becomes possible (in principle) to discriminate between charge and strain effects. With ferroelectric materials one can conveniently exploit the fact that the substrate polarization state is remanent, i.e. it is preserved when the voltage is reduced to zero. The possibility to directly monitor the electrical switching process by measuring the current vs. applied voltage allowed to determine unambiguously the polarization state of the substrate before and after the magnetic measurements of the overlayer. The same approach could however be easily extended to piezoelectric materials. The main spectroscopic method adopted was XMCD with synchrotron radiation. By measuring the X-ray absorption resonances ($L_{2,3}$ edges of the $3d$ metals) one has access both to the magnetic moment and to the chemical state of the magnetic ion, making it possible to address issues like ion migration or change in the valence state. The *in-operando* method was also employed in microscopy: it turned out to be very useful in displaying novel phenomena occurring as a consequence of magnetoelectric coupling in these systems. This ferroelectric crystals are highly inhomogeneous, and this is exemplified by the case of PMN-PT.

Two case studies: similarities and differences

While belonging to the same class of heterostructures, the two case studies differ under many aspects. LSMO is a perovskite oxide, which for the optimal La/Sr ratio has a high T_C (370 K) and a high spin polarization. The physics of manganese oxides is complex: several parameters like doping, pressure, strain, temperature determine drastic changes in their magnetic properties. The synthesis of LSMO thin films requires a careful control of the stoichiometry and of the processing parameters, such as temperature and partial pressures during growth. We deposited LSMO on a BTO substrate, which is a prototypical ferroelectric material, that presents different crystal structures at different temperatures. To obtain the epitaxial growth, a high processing temperature is needed.

Fe is a most common transition metal, certainly the more studied among magnetic materials. Fe has a very high T_C (above 1050 K) and a magnetic moment of 2.12 μ_B. The T_C of Fe is reduced for monolayer (ML) films, but above 3 ML it is well above room temperature and in the thin film regime (several nm) it is bulk-like. Fe can be deposited by several techniques, some of them industrially scalable such as sputtering or chemical methods [101]. In our experiments the deposition was carried out using an e-beam UHV evaporator with the substrate maintained at room temperature, without preliminary surface preparation of the substrate. PMN-PT is well known for its strong piezoelectricity and it is also ferroelectric. Its phase diagram as a function of stoichiometry is complex, and some of its properties are not well understood, but it does not undergo structural changes as a function of temperature. Compared to the previous system, this heterostructure is much simpler (and cheaper) to fabricate.

Summary of the results

In the LSMO/BTO heterostructure I found that the variation in strain due to the epitaxial relationship when the BTO substrate undergoes structural changes is reflected in the magnetic properties of the LSMO film. The magnetization of LSMO can be controlled both by temperature, e.g when reaching the crystallographic phase transitions of BTO, or at fixed room temperature, by the application of electric fields. The ferroelectric domain distribution in the tetragonal phase can be changed by the application of $\vec{E}$-fields. The main result that we found is that, in the conditions explored, a magnetic phase transition can be induced. These results are in line with the current understanding of strain-induced effects in manganites, which are however far from trivial. They cannot be reduced to inverse magnetostriction, but descend from the physics of correlated electron systems: lattice, orbital occupation and magnetic interactions are strongly entangled.

In the (Fe,FeMn)/PMN-PT heterostructure I found that the reversal of electric polarization prompts a giant modulation of the magnetic anisotropy, as well as rotation of the magnetic domains. The effect however is local and associated with a morphology change. Our novel observation is that the morphological change is electrically-driven and reversible. Magnetoelectric coupling in this system eludes interpretation based on the canonical mechanisms, and points at morphology as a new parameter to be considered in multiferroic heterostructures. The fact that similar effects have been observed for FeMn and Fe suggest that this phenomenon can be quite general.

Significance of this work

The strain-induced change of magnetic anisotropy by inverse magnetostriction is a phenomenon that is now reasonably well-understood, thanks to quite many reports in the literature (see those cited in chapter 4). A model scenario involves a strain transfer across a flat and defect-free interface, which determines a uniform expansion or contraction of the magnetic film across the whole thickness, finally the magnetic anisotropy is modified by the applied stress. This approach faces two main challenges towards applications. One is how to move from bulk ferroelectric crystal to thin film to be implemented in nano-devices, while maintaining an efficient electrically induced deformation. Substrate clamping usually limits the piezoelectric expansion in thin films, so this deserves more investigation. The second one is how to implement strain-driven magnetoelectric coupling for memory applications. Ideally an ON/OFF behavior is obtainable rotating the magnetization by 180°, but this is not achievable with strain only.

Both our studies go beyond this paradigm in different ways, somehow tackling separately the aforementioned challenges. In the LSMO/BTO case the non-conventional characteristics of LSMO translate in an unconventional effect: a magnetic phase transition instead of a change in anisotropy. This is a kind of ON/OFF behavior that, in principle, is suitable for a memory device. Besides that, we still rely on strain transfer in the canonical sense, and hence the requirement of good, clean epitaxial interfaces. On the other hand, in the Fe/PMN-PT case the complexity of behavior shifts from the magnetic to the ferroelectric component: the observed phenomena come from the extraordinary mechanical response of PMN-PT to electrical stimuli. A variety of effects (on the magnetic point of view) may arise according to the possible geometries of the morphology. Moreover, the sample can apparently be synthesized in quite rough conditions. This example is at odds with the ideal interface scenario, and shows that morphology may be alternatively used to manipulate anisotropy. Hence, we may think how to exploit this avoiding the use of ferroelectric crystals (see e.g. the device proposed in the final section of chapter 4).

Outlook

What can the case studies of this thesis tell about the future application advances of multiferroic heterostructures? They indicate different ways for the electrical control of magnetism beyond inverse-magnetostriction. One way is to exploit the rich possibilities offered by correlated transition metal oxides. In terms of applications, there are many technical challenges to face in integrating these materials in a device. Another hurdle is the intrinsic tendency of manganites to phase separation, which may impede achieving a high ON/OFF signal ratio, whatever this magnetic "signal" will be. On the other hand, we may obtain strong effects moving away from the ideal strain-mediated scenario, which includes a perfect interface and uniform deformation. The results here discussed on Fe/PMN-PT serve as an exemplifying case. One path for the future is hence the following: to apply "strain" in non-conventional ways, i.e. that can be intentionally not homogeneous and induce a morphological change. On the microscopic scale, strong magneto-electric coupling can be obtained, mediated by different kind of effects. The key challenge will be twofold: achieving control on the desired morphological change, and discern the different phenomena contributing to magneto-electric coupling. For the latter, as we have shown, the in-operando approach will be extremely useful for spectroscopy, microscopy and diffraction. New geometries for artificial multiferroics must be envisioned, most likely involving patterning and/or nano-structuring [102]. There is plenty of room for creativity in such a process for the years to come.

Abbreviations used

AFM	Atomic Force Microscopy
BFO	$BiFeO_3$
BTO	$BaTiO_3$
CMR	Colossal Magneto Resistance
DFT	Density Functional Theory
DOS	Density of States
GMR	Giant Magneto Resistance
HDD	Hard Disk Drive
LEED	Low Energy Electron Diffraction
LSMO	$La_{0.65}Sr_{0.35}MnO_3$
MBE	Molecular Beam Epitaxy
ME	Magneto Electric
ML	Mono-Layer
MOKE	Magneto Optical Kerr Effect
MRAM	Magnetic Random Access Memory
MTJ	Magnetic Tunnel Junction
PEEM	Photoemission Electron Microscopy
PFM	Piezo Force Microscopy
PLD	Pulsed Laser Deposition
PMN-PT	$PbMn_{0.65}Nb_{0.35}O_3$-$PbTiO_3$
RHEED	Reflection High Energy Electron Diffraction
SEM	Scanning Electron Microscopy
SEMPA	SEM with Polarization Analysis
SOT	Spin Orbit Torque

SQUID	Supercondunucting QUantum Interferometry Device
SR	Synchrotron Radiation
STO	$SrTiO_3$
STT	Spin Transfer Torque
TEM	Transmission Electron Microscopy
TEY	Total Electron Yield
TFY	Total Fluorescence Yield
u.c.	unit cell
VSM	Vibrating Sample Magnetometry
XAS	X-ray Absorption Spectroscopy
XLD	X-ray Linear Dichroism
XMCD	X-ray Magnetic Circular Dichroism
XPS	X-ray Photoemission Spectroscopy

Bibliography

[1] N. A. Spaldin and R. Ramesh. “Advances in magnetoelectric multiferroics”. In: *Nature Materials* 18.3 (2019), pp. 203–212. DOI: 10.1038/s41563-018-0275-2.

[2] A. Fert. “Nobel Lecture: Origin, Development, and Future of Spintronics”. In: *Review Of Modern Physics* 80 (2008), p. 1517. DOI: 10.1002/anie.200801093.

[3] S. Yuasa et al. “Future prospects of MRAM technologies”. In: *2013 IEEE International Electron Devices Meeting.* IEEE, 2013, pp. 3.1.1–3.1.4. DOI: 10.1109/IEDM.2013.6724549.

[4] J. Akerman. “Toward a Universal Memory”. In: *Science* 308.5721 (2005), pp. 508–510. DOI: 10.1126/science.1110549.

[5] P. Gambardella and I. M. Miron. “Current-induced spin-orbit torques”. In: *Philosophical Transactions of the Royal Society A: Mathematical, Physical and Engineering Sciences* 369.1948 (2011), pp. 3175–3197. DOI: 10.1098/rsta.2010.0336.

[6] M. Cubukcu et al. “Ultra-Fast Perpendicular Spin-Orbit Torque MRAM”. In: *IEEE Transactions on Magnetics* 54.4 (2018). DOI: 10.1109/TMAG.2017.2772185.

[7] H. Ohno, M. D. Stiles, and B. Dieny. “Spintronics”. In: *Proceedings of the IEEE* 104.10 (2016), pp. 1782–1786. DOI: 10.1109/JPROC.2016.2601163.

[8] L. Chen et al. “Electric-field control of interfacial spin-orbit fields”. In: *Nature Electronics* 1.6 (2018), pp. 350–355. DOI: 10.1038/s41928-018-0085-1.

[9] S. Manipatruni et al. “Scalable energy-efficient magnetoelectric spin-orbit logic”. In: *Nature* 565.7737 (2019), pp. 35–42. DOI: 10.1038/s41586-018-0770-2.

[10] F. Matsukura, Y. Tokura, and H. Ohno. “Control of magnetism by electric fields”. In: *Nature Nanotechnology* 10.3 (2015), pp. 209–220. DOI: 10.1038/nnano.2015.22.

[11] L. W. Martin and R. Ramesh. “Multiferroic and magnetoelectric heterostructures”. In: *Acta Materialia* 60.6-7 (2012), pp. 2449–2470. DOI: 10.1016/j.actamat.2011.12.024.

[12] N. A. Hill. “Why Are There so Few Magnetic Ferroelectrics?” In: *J. Phys. Chem. B* 104.29 (2000), pp. 6694–6709. DOI: 10.1021/jp000114x.

[13] M. Fiebig, T. Lottermoser, D. Meier, and M. Trassin. “The evolution of multiferroics”. In: *Nature Reviews Materials* 1.8 (2016), p. 16046. DOI: 10.1038/natrevmats.2016.46.

[14] J. M. Hu, L. Q. Chen, and C. W. Nan. “Multiferroic Heterostructures Integrating Ferroelectric and Magnetic Materials”. In: *Advanced Materials* 28.1 (2016), pp. 15–39. DOI: 10.1002/adma.201502824.

[15] T. Jungwirth, X. Marti, P. Wadley, and J. Wunderlich. “Antiferromagnetic spintronics”. In: *Nature Nanotechnology* 11.3 (2016), pp. 231–241. DOI: 10.1038/nnano.2016.18.

[16] P. Wadley et al. “Electrical switching of an antiferromagnet”. In: *Science* 1031.January (2015), pp. 1–10. DOI: 10.1126/science.aab1031.

[17] H. Y. Hwang et al. "Emergent phenomena at oxide interfaces". In: *Nature Materials* 11.2 (2012), pp. 103–113. DOI: 10.1038/nmat3223.

[18] C. Song et al. "Recent progress in voltage control of magnetism: Materials, mechanisms, and performance". In: *Progress in Materials Science* 87 (2017), pp. 33–82. DOI: 10.1016/j.pmatsci.2017.02.002.

[19] C. H. Ahn, J.-M. Triscone, and J. Mannhart. "Electric field effect in correlated oxide systems". In: *Nature* 424.6952 (2003), pp. 1015–1018. DOI: 10.1038/nature01878.

[20] C. A. F. Vaz, F. J. Walker, C. H. Ahn, and S. Ismail-Beigi. "Intrinsic interfacial phenomena in manganite heterostructures". In: *Journal of Physics Condensed Matter* 27.12 (2015), p. 123001. DOI: 10.1088/0953-8984/27/12/123001.

[21] S. Fusil, V. Garcia, A. Barthélémy, and M. Bibes. "Magnetoelectric Devices for Spintronics". In: *The Annual Review of Material Research* 44 (2014), pp. 91–116. DOI: 10.1146/annurev-matsci-070813-113315.

[22] J.-M. Hu, T. Nan, N. X. Sun, and L.-Q. Chen. "Multiferroic magnetoelectric nanostructures for novel device applications". In: *MRS Bulletin* 40.09 (2015), pp. 728–735. DOI: 10.1557/mrs.2015.195.

[23] M. Bibes and A. Barthélémy. "Multiferroics: Towards a magnetoelectric memory". In: *Nature Materials* 7.6 (2008), pp. 425–426. DOI: 10.1038/nmat2189.

[24] G. S. Abo et al. "Definition of magnetic exchange length". In: *IEEE Transactions on Magnetics* 49.8 (2013), pp. 4937–4939. DOI: 10.1109/TMAG.2013.2258028.

[25] J. T. Heron et al. "Deterministic switching of ferromagnetism at room temperature using an electric field". In: *Nature* 516.7531 (2014), pp. 370–373. DOI: 10.1038/nature14004.

[26] D. G. Schlom et al. "A thin film approach to engineering functionality into oxides". In: *Journal of the American Ceramic Society* 91.8 (2008), pp. 2429–2454. DOI: 10.1111/j.1551-2916.2008.02556.x.

[27] D. G. Schlom. "Perspective: Oxide molecular-beam epitaxy rocks!" In: *APL Materials* 3.6 (2015), p. 62403. DOI: 10.1063/1.4919763.

[28] S. Hasegawa. “Reflection High-Energy Electron Diffraction”. In: *Characterization of Materials*. Hoboken, NJ, USA: John Wiley & Sons, Inc., 2012, pp. 1–14. DOI: 10.1002/0471266965.com139.

[29] D. G. Schlom et al. “Oxide nano-engineering using MBE”. In: *Materials Science and Engineering B* 87.3 (2001), pp. 282–291. DOI: 10.1016/S0921-5107(01)00726-7.

[30] Y. Cao et al. “Artificial two-dimensional polar metal at room temperature”. In: *Nature Communications* 9.1 (2018), p. 1547. DOI: 10.1038/s41467-018-03964-9.

[31] T. Yajima et al. “Controlling band alignments by artificial interface dipoles at perovskite heterointerfaces”. In: *Nature Communications* 6 (2015), p. 6759. DOI: 10.1038/ncomms7759.

[32] J. Chakhalian et al. “Colloquium: Emergent properties in plane view: Strong correlations at oxide interfaces”. In: *Reviews of Modern Physics* 86.4 (2014). DOI: 10.1103/RevModPhys.86.1189.

[33] J. A. Mundy et al. “Atomically engineered ferroic layers yield a room-temperature magnetoelectric multiferroic”. In: *Nature* 537.7621 (2016), pp. 523–527. DOI: 10.1038/nature19343.

[34] G. van der Laan and A. I. Figueroa. “X-ray magnetic circular dichroism - A versatile tool to study magnetism”. In: *Coordination Chemistry Reviews* 277 (2014), pp. 95–129. DOI: 10.1016/j.ccr.2014.03.018.

[35] F. de Groot and A. Kotani. *Core level spectroscopy of solids*. CRC Press, 2008, p. 490.

[36] J. Stöhr and H. C. Siegmann. *Magnetism : from fundamentals to nanoscale dynamics*. Springer, 2006, p. 820.

[37] J. Stöhr. “X-ray magnetic circular dichroism spectroscopy of transition metal thin films”. In: *Journal of Electron Spectroscopy and Related Phenomena* 2048.95 (1995).

[38] G. Shibata et al. “Anisotropic spin-density distribution and magnetic anisotropy of strained $\mathrm{La}_{1-x}\mathrm{Sr}_x\mathrm{MnO}_3$ thin films: angle-dependent x-ray magnetic circular dichroism”. In: *npj Quantum Materials* 3.1 (2018), p. 3. DOI: 10.1038/s41535-018-0077-4.

[39] C. Stamm et al. “Antiferromagnetic-ferromagnetic phase transition in FeRh probed by x-ray magnetic circular dichroism”. In: *Physical Review B* 77.18 (2008), p. 184401. DOI: 10.1103/PhysRevB.77.184401.

[40] F. Maccherozzi et al. “Evidence for a magnetic proximity effect up to room temperature at Fe/(Ga,Mn)As interfaces”. In: *Physical Review Letters* 101.26 (2008), p. 267201. DOI: 10.1103/PhysRevLett.101.267201.

[41] S. Polisetty et al. “Optimization of magneto-optical Kerr setup: Analyzing experimental assemblies using Jones matrix formalism”. In: *Review of Scientific Instruments* 79.5 (2008), p. 055107. DOI: 10.1063/1.2932445.

[42] A. Berger, O. Idigoras, and P. Vavassori. “Transient behavior of the dynamically ordered phase in uniaxial cobalt films”. In: *Physical Review Letters* 111.19 (2013), p. 190602. DOI: 10.1103/PhysRevLett.111.190602.

[43] P. Vavassori. “Polarization modulation technique for magneto-optical quantitative vector magnetometry”. In: *Applied Physics Letters* 77.11 (2000), pp. 1605–1607. DOI: 10.1063/1.1310169.

[44] É. Du Trémolet de Lacheisserie, D. Gignoux, and M. Schlenker. *Magnetism*. Springer, 2005.

[45] V. K. Valev. *Magneto Optical Effects Tutorial*. URL: http://people.bath.ac.uk/vkv23/English/RechercheTo.htm (visited on 05/07/2019).

[46] V. Antonov, B. Harmon, and A. Yaresko. *Electronic structure and magneto-optical properties of solids*. Kluwer Academic Publishers, 2004, p. 528.

[47] A. Comin et al. “Elastic and magnetic dynamics of nanomagnet-ordered arrays impulsively excited by subpicosecond laser pulses”. In: *Physical Review Letters* 97.21 (2006), p. 217201. DOI: 10.1103/PhysRevLett.97.217201.

[48] M. M. Decker et al. “Time Resolved Measurements of the Switching Trajectory of Pt/Co Elements Induced by Spin-Orbit Torques”. In: *Physical Review Letters* 118.25 (2017), p. 257201. DOI: 10.1103/PhysRevLett.118.257201.

[49] D. A. Allwood, G. Xiong, M. D. Cooke, and R. P. Cowburn. “Magneto-optical Kerr effect analysis of magnetic nanostructures”. In: *Journal Of Physics D-Applied Physics* 36.18 (2003), pp. 2175–2182. DOI: 10.1088/0022-3727/36/18/001.

[50] M. Grimsditch and P. Vavassori. “The diffracted magneto-optic Kerr effect: What does it tell you?” In: *Journal of Physics Condensed Matter* 16.9 (2004), R275–R294. DOI: 10.1088/0953-8984/16/9/R01.

[51] J. McCord. “Progress in magnetic domain observation by advanced magneto-optical microscopy”. In: *Journal of Physics D: Applied Physics* 48.33 (2015), p. 333001. DOI: 10.1088/0022-3727/48/33/333001.

[52] A. R. Khorsand et al. “Element-Specific Probing of Ultrafast Spin Dynamics in Multisublattice Magnets with Visible Light”. In: *Physical Review Letters* 110.10 (2013), p. 107205. DOI: 10.1103/PhysRevLett.110.107205.

[53] *NFFA - Trieste*. URL: http://trieste.nffa.eu/.

[54] *NFFA - Europe*. URL: https://www.nffa.eu/.

[55] G. Panaccione et al. “Advanced photoelectric effect experiment beamline at Elettra: A surface science laboratory coupled with Synchrotron Radiation”. In: *Review of Scientific Instruments* 80.4 (2009), p. 043105. DOI: 10.1063/1.3119364.

[56] G. Vinai et al. “MBE Cluster: a chain of UHV chambers for growth and in-situ characterization for spintronic applications”. In: *(in preparation)* (2019).

[57] J. H. Haeni, C. D. Theis, and D. G. Schlom. “RHEED Intensity Oscillations for the Stoichiometric Growth of $SrTiO_3$ Thin Films by Reactive Molecular Beam Epitaxy”. In: *Journal of Electroceramics* 4.2 (2000), pp. 385–391. DOI: 10.1023/A:1009947517710.

[58] *I06: Nanoscience at Diamond Light Source*. URL: https://www.diamond.ac.uk/Instruments/Magnetic-Materials/I06.html.

[59] F. Motti et al. “Strain-induced magnetization control in an oxide multiferroic heterostructure”. In: *Physical Review B* 97.9 (2018), p. 094423. DOI: 10.1103/PhysRevB.97.094423.

[60] A. Haghiri-Gosnet and J. Renard. “CMR manganites: physics, thin films and devices”. In: *Journal of Physics D: Applied Physics* 36.8 (2003), R127–R150. DOI: 10.1088/0022-3727/36/8/201.

[61] E. Dagotto, T. Hotta, and A. Moreo. “Colossal magnetoresistant materials: the key role of phase separation”. In: *Physics Reports* 344.1-3 (2001), pp. 1–153. DOI: 10.1016/S0370-1573(00)00121-6.

[62] T. H. E. Lahtinen and S. Van Dijken. “Temperature control of local magnetic anisotropy in multiferroic CoFe/$BaTiO_3$”. In: *Applied Physics Letters* 102.11 (2013), p. 112406. DOI: 10.1063/1.4795529.

[63] C. Adamo et al. “Effect of biaxial strain on the electrical and magnetic properties of (001) LSMO thin films”. In: *Applied Physics Letters* 95.11 (2009), p. 112504. DOI: 10.1063/1.124050.

[64] M. K. Lee et al. “Strain modification of epitaxial perovskite oxide thin films using structural transitions of ferroelectric $BaTiO_3$ substrate”. In: *Applied Physics Letters* 77.22 (2000), pp. 3547–3549. DOI: 10.1063/1.1328762.

[65] C. Thiele et al. “Influence of strain on the magnetization and magnetoelectric effect in LAMO / PMN-PT (A = Sr, Ca. . .)” In: *Physical Review B* 75 (2007), p. 054408. DOI: 10.1103/PhysRevB.75.054408.

[66] W. Eerenstein et al. “Giant sharp and persistent converse magnetoelectric effects in multiferroic epitaxial heterostructures”. In: *Nature Materials* 6.5 (2007), pp. 348–351. DOI: 10.1038/nmat1886.

[67] A. Alberca et al. “Phase separation enhanced magneto-electric coupling in $La_{0.7}Ca_{0.3}MnO_3/BaTiO_3$ ultra-thin films”. In: *Scientific Reports* 5.1 (2016), p. 17926. DOI: 10.1038/srep17926.

[68] R. V. Chopdekar et al. “Strain-dependent magnetic configurations in manganite-titanate heterostructures probed with soft X-ray techniques”. In: *European Physical Journal B* 86.6 (2013), p. 241. DOI: 10.1140/epjb/e2013-30995-4.

[69] J. Heidler et al. “Manipulating magnetism in $La_{0.7}Sr_{0.3}MnO_3$ via piezostrain”. In: *Physical Review B* 91 (2015), p. 024406. DOI: 10.1103/PhysRevB.91.024406.

[70] H. Guo et al. “Interface-induced multiferroism by design in complex oxide superlattices”. In: *Proceedings of the National Academy of Sciences* (2017), p. 201706814. DOI: 10.1073/pnas.1706814114.

[71] G. Shibata et al. “Thickness-dependent ferromagnetic metal to paramagnetic insulator transition in $La_{0.6}Sr_{0.4}MnO_3$ thin films studied by x-ray magnetic circular dichroism”. In: *Physical Review B* 89.23 (2014), p. 235123. DOI: 10.1103/PhysRevB.89.235123.

[72] G. H. Kwei, A. C. Lawson, S. J. L. Billinge, and S. W. Cheong. “Structures of the ferroelectric phases of barium titanate”. In: *The Journal of Physical Chemistry* 97.10 (1993), pp. 2368–2377. DOI: 10.1021/j100112a043.

[73] J.-L. Maurice et al. “Strain relaxation in the epitaxy of $La_{2/3}Sr_{1/3}MnO_3$ grown by pulsed-laser deposition on $SrTiO_3$ (001)”. In: *Philosophical Magazine* 83.28 (2003), pp. 3201–3224. DOI: 10.1080/14786430310001603436.

[74] P. Giannozzi et al. “Quantum ESPRESSO: a modular and open-source software project for quantum simulations of materials”. In: *Journal of Physics: Condensed Matter* 21.39 (2009), p. 395502. DOI: 10.1088/0953-8984/21/39/395502.

[75] J. D. Burton and E. Y. Tsymbal. “Prediction of electrically induced magnetic reconstruction at the manganite/ferroelectric interface”. In: *Physical Review B - Condensed Matter and Materials Physics* 80.17 (2009), pp. 1–6. DOI: 10.1103/PhysRevB.80.174406.

[76] C. A. F. Vaz et al. “Origin of the Magnetoelectric Coupling Effect in PZT/LSMO Multiferroic Heterostructures”. In: *Physical Review Letters* 104 (2010), p. 127202. DOI: 10.1103/PhysRevLett.104.127202.

[77] Y. W. Yin et al. “Enhanced tunnelling electroresistance effect due to a ferroelectrically induced phase transition at a magnetic complex oxide interface.” In: *Nature materials* 12.February (2013), pp. 1–6. DOI: 10.1038/nmat3564.

[78] T. L. Meyer et al. “Enhancing interfacial magnetization with a ferroelectric”. In: *Physical Review B* 94 (2016), p. 174432. DOI: 10.1103/PhysRevB.94.174432.

[79] G. Vinai et al. “Reversible Modification of Ferromagnetism through Electrically Controlled Morphology”. In: *Advanced Electronic Materials* 5.7 (2019), p. 1900150. DOI: 10.1002/aelm.201900150.

[80] B. D. Cullity and C. D. Graham. *Introduction to Magnetic Materials*. Hoboken, NJ, USA: John Wiley & Sons, Inc., 2008. DOI: 10.1002/9780470386323.

[81] A. A. Bokov and Z. G. Ye. “Recent progress in relaxor ferroelectrics with perovskite structure”. In: *Journal of Materials Science* 41.1 (2006), pp. 31–52. DOI: 10.1007/s10853-005-5915-7.

[82] O. Noblanc, P. Gaucher, and G. Calvarin. “Structural and dielectric studies of $Pb(Mg_{1/3}Nb_{2/3})O_3$-$PbTiO_3$ ferroelectric solid solutions around the morphotropic boundary”. In: *Journal of Applied Physics* 79.8 (1996), pp. 4291–4297. DOI: 10.1063/1.361865.

[83] Y. Zhang et al. “Adaptive ferroelectric state at morphotropic phase boundary: Coexisting tetragonal and rhombohedral phases”. In: *Acta Materialia* 71 (2014), pp. 176–184. DOI: 10.1016/j.actamat.2014.03.007.

[84] B. Noheda et al. “Phase diagram of the ferroelectric relaxor $(1-x)PbMg_{1/3}Nb_{2/3}O_3$-$xPbTiO_3$”. In: *Physical Review B* 66.5 (2002), pp. 541041–5410410. DOI: 10.1103/PhysRevB.66.054104.

[85] P. Zhao et al. “Domain engineered switchable strain states in ferroelectric (011) $[Pb(Mg_{1/3}Nb_{2/3})O_3](1-x)$-$[PbTiO_3]x$ (PMN-PT $x \approx 0.32$) single crystals”. In: *Journal of Applied Physics* 109.12 (2011), p. 124101. DOI: 10.1063/1.3595670.

[86] J. J. Yang et al. “Electric field manipulation of magnetization at room temperature in multiferroic $CoFe_2O_4/Pb(Mg_{1/3}Nb_{2/3})_{0.7}Ti_{0.3}O_3$ heterostructures”. In: *Applied Physics Letters* 94.21 (2009), p. 212504. DOI: 10.1063/1.3143622.

[87] S. Zhang et al. “Electric-field control of nonvolatile magnetization in $Co_{40}Fe_{40}B_{20}/Pb(Mg_{1/3}Nb_{2/3})_{0.7}Ti_{0.3}O_3$ structure at room temperature”. In: *Physical Review Letters* 108.13 (2012), p. 137203. DOI: 10.1103/PhysRevLett.108.137203.

[88] M. Buzzi et al. “Single domain spin manipulation by electric fields in strain coupled artificial multiferroic nanostructures”. In: *Physical Review Letters* 111.2 (2013), p. 027204. DOI: 10.1103/PhysRevLett.111.027204.

[89] C. Zhang et al. “Electric field mediated non-volatile tuning magnetism at the single-crystalline $Fe/Pb(Mg_{1/3}Nb_{2/3})_{0.7}Ti_{0.3}O_3$ interface”. In: *Nanoscale* 7.9 (2015), pp. 4187–4192. DOI: 10.1039/C4NR05847J.

[90] J. Heidler et al. “Magnetoelectroelastic control of magnetism in an artificial multiferroic”. In: *Physical Review B* 94.1 (2016). DOI: 10.1103/PhysRevB.94.014401.

[91] P. Li et al. “Spatially resolved ferroelectric domain-switching controlled magnetism in $Co_{40}Fe_{40}B_{20}/Pb(Mg_{1/3}Nb_{2/3})_{0.7}Ti_{0.3}O_3$ multiferroic heterostructure”. In: *ACS Applied Materials and Interfaces* 9.3 (2017), pp. 2642–2649. DOI: 10.1021/acsami.6b13620.

[92] S. Zhang et al. “Strain-Mediated Coexistence of Volatile and Nonvolatile Converse Magnetoelectric Effects in $Fe / Pb(Mg_{1/3}Nb_{2/3})_{0.7}Ti_{0.3}O_3$ heterostructure”. In: *ACS Applied Materials and Interfaces* 9.24 (2017), pp. 20637–20647. DOI: 10.1021/acsami.7b03051.

[93] R. Lo Conte et al. “Influence of Nonuniform Micron-Scale Strain Distributions on the Electrical Reorientation of Magnetic Microstructures in a Composite Multiferroic Heterostructure”. In: *Nano Letters* 18.3 (2018), pp. 1952–1961. DOI: 10.1021/acs.nanolett.7b05342.

[94] Y. Ba et al. “Spatially Resolved Electric-Field Manipulation of Magnetism for CoFeB Mesoscopic Discs on Ferroelectrics”. In: *Advanced Functional Materials* 28.11 (2018), p. 1706448. DOI: 10.1002/adfm.201706448.

[95] Z. Q. Liu et al. “Electrically reversible cracks in an intermetallic film controlled by an electric field”. In: *Nature Communications* 9.1 (2018), p. 41. DOI: 10.1038/s41467-017-02454-8.

[96] M. Ghidini et al. “Shear-strain-mediated magnetoelectric effects revealed by imaging”. In: *Nature Materials* (2019). DOI: 10.1038/s41563-019-0374-8.

[97] R. O. Cherifi et al. “Electric-field control of magnetic order above room temperature”. In: *Nature Materials* 13.4 (2014), pp. 345–351. DOI: 10.1038/nmat3870.

[98] R. Lebrun et al. “Tunable long-distance spin transport in a crystalline antiferromagnetic iron oxide”. In: *Nature* 561.7722 (2018), pp. 222–225. DOI: 10.1038/s41586-018-0490-7.

[99] P. S. Miedema and F. M. De Groot. “The iron L edges: Fe2p X-ray absorption and electron energy loss spectroscopy”. In: *Journal of Electron Spectroscopy and Related Phenomena* 187.1 (2013), pp. 32–48. DOI: 10.1016/j.elspec.2013.03.005.

[100] V. Polewczyk et al. “Designing and modelling of a patterned multiferroic heterostructure to modify locally the magnetic shape anisotropy”. In: *(in preparation)* (2019).

[101] S. Vangelista et al. “Chemical vapor deposition growth of Fe_3O_4 thin films and Fe/Fe_3O_4 bi-layers for their integration in magnetic tunnel junctions”. In: *Thin Solid Films* 520.14 (2012), pp. 4617–4621. DOI: 10.1016/J.TSF.2011.10.128.

[102] G. Vinai et al. “Giant magneto-electric coupling in 100 nm thick Co capped by ZnO nanorods”. In: *Nanoscale* 10.3 (2018), pp. 1326–1336. DOI: 10.1039/C7NR09233D.

List of publications

- **F. Motti**, G. Vinai, A. Petrov, B. A. Davidson, B. Gobaut, A. Filippetti, G. Rossi, G. Panaccione and P. Torelli - *Strain-induced magnetization control in an oxide multiferroic heterostructure.* Phys. Rev. B 2018, 97, 094423.
- G. Vinai, **F. Motti**, V. Bonanni, A. Y. Petrov, S. Benedetti, C. Rinaldi, M. Stella, D. Cassese, S. Prato, M. Cantoni, G. Rossi, G. Panaccione and P. Torelli - *Reversible Modification of Ferromagnetism through Electrically Controlled Morphology.* Adv. Electron. Mater. 2019, 1900150.
- C. Baeumer, T. Heisig, B. Arndt, K. Skaja, F. Borgatti, F. Offi, **F. Motti**, G. Panaccione, R. Waser, S. Menzel, and R. Dittmann - *Spectroscopic elucidation of ionic motion processes in tunnel oxide-based memristive devices.* Faraday Discuss. 2019, 213, 215.
- **F. Motti** G. Vinai, V. Bonanni, C. Rinaldi, M. Stella, M. Cantoni, T. Forrest, F. Maccherozzi, S. Dhesi, G. Rossi, G. Panaccione and P. Torelli - *Local investigation on the role of voltage-induced surface cracks on the magnetic response in magneto-electric heterostructures.* In preparation.
- I. Aliaj, A. Guarino, E. De Gennaro, **F. Motti**, P. Torelli, F.M. Granozio, S. Roddaro et al. - *X-ray Spectroscopic Investigation of Graphene-LAO/STO Hybrid Systems.* In preparation.
- G. M. Pierantozzi, A. Petrov, G. Vinai, **F. Motti**, R. Cucini, A. De Vita, T. Pincelli, A. Gessini, J. Fujii, M. Oura, V. Polewczyk, F. Offi, F. Borgatti, G. Rossi and G. Panaccione - *Strain induced competing electronic phases in LCMO.* In preparation.